

Fuel Consumption Reduction Through Velocity Optimization for Light-Duty Autonomous Vehicles with Different Energy Sources

by

Niket Prakash

A dissertation submitted in partial fulfillment
of the requirements for the degree of
Doctor of Philosophy
(Mechanical Engineering)
in The University of Michigan
2019

Doctoral Committee:

Professor Anna G. Stefanopoulou, Chair
Assistant Professor Youngki Kim
Professor Ilya Kolmanovsky
Associate Research Scientist Jason Siegel
Assistant Professor Ramnarayan Vasudevan

“one should not increase, beyond what is necessary, the number of entities required to explain anything” - William of Ockham

Niket Prakash
niketpr@umich.edu
ORCID iD: 0000-0001-5432-819X

© Niket Prakash 2019

To my parents Thakur Vikas Sinha and Amita Sinha for allowing me to define and pursue my own goals, and my sister Vanika for always having my back

ACKNOWLEDGEMENTS

I want to thank my committee chair Professor Anna Stefanopoulou for her constant help and support throughout my time in her Powertrain Controls Lab. Her large research group gave me the opportunity to pursue various diverse projects, from advanced engine combustion modes during my Master's degree to autonomous vehicles propelled by everything from gasoline engines to fuel cells. In the following paragraphs I will thank all the people who helped me in specific aspects of these diverse pursuits, but none of this would be possible without the mentorship of Prof. Stefanopoulou.

I would like to thank Assistant Professor Youngki Kim for all his help and support in formulating and solving the autonomous vehicle control problem. I would also like to thank Associate Research Scientist Jason Siegel for his guidance and support in formulating and solving the hybrid Fuel Cell problem. I am grateful to Professor Ilya Kolmanovsky and Assistant Professor Ramnarayan Vasudevan for their valuable inputs as members of my committee.

I am grateful to the U.S. EPA and the ORISE program for their intellectual and financial support, and I would like to particularly thank Dr. Matthew Brusstar for his help while I was at the U.S. EPA. I would also like to thank Dr. Andrew Moskalik, Mr. Aaron Hula and Dr. David Haugen for their valuable inputs. I want to thank Mr. Thomas Veling for his help in successfully running the dynamometer tests at the facility. I also want to thank Mr. Kevin Newman and Mr. Paul DeKraker for their help with the ALPHA model which is integral to this thesis.

The work on Fuel Cell hybrids was made possible because of the intellectual and financial help from the Automotive Research Center in accordance with Cooperative Agreement W56HZV-14-2-0001 with the U.S. Army CDCC Ground Vehicle Systems Center via the project "The Advanced Vehicle Power Technology Alliance." I am particularly grateful to Dr. Denise Rizzo for all her help and support.

One of the great joys of working at the Powertrain Controls Lab was the ability to

interact and learn from my wonderful colleagues. I want to thank Dr. Jason Martz for his incredible support at the beginning of my time here, his constant guidance was extremely important for me. I want to thank the lab alumni for their counsel Dr. Huan Lian, Dr. Shyam Jade and Dr. Jacob Larimore. I am also grateful to Dr. Patrick Gorzelic, Dr. Sandro Nuesch and Dr. Shankar Mohan who were my seniors and always ready with advice as I was finding my feet in the lab. I enjoyed working immensely with Dr. Gionata Cimini, Mrs. Shima Nazari, Ms. Di Chen, Ms. Eunjeong Hyeon and Ms. Miriam Figueroa-Santos on our papers together. I would like to thank everyone in the lab for their insights Dr. Rasoul Salehi, Dr. Robert Middleton, Mr. Rani Kiwan, Mr. Bryan Maldonado, Ms. Chunan Huang, Mr. Mitchell Bieniek, Mr. Suhak Lee, Mr. Peyman Mohtat, Mr. Sarvanan Duraiarasan, Mr. Ting Cai, Mr. Sravan Pannala and Mr. Joeseph Drallmeier.

Because of the ORISE scholarship I was able to work with other PhD students at the EPA's Ann Arbor lab who brought in their own unique research goals which were very different from mine. I am grateful for my interactions with my fellow lab mates Dr. Shao Teng Chong, Dr. Ati (Sedigheh) Tolou, Mr. Justin Koczak, Mrs. Christina Reynolds and Mr. Rinav Pillai.

Over the last five years, my professional work was greatly enhanced by the amazing friendships I developed outside of the lab. My friends forced me to take time off and discover some of the more entertaining aspects of living in the US and specifically Ann Arbor. I would like to thank Kumar Aanjaneya, Sneha Agarwal, Mayank Agarwal, Abhishek Bafna, Nikita Bhutani, Amberlyn Britt, Omkar Daud, Aniket Deshmukh, Harshad Dharmatti, Varun Gala, Kunal Garg, Vaibhav Gogte, Arnab Hazari, Sneha Joshi, Bikash Kanungo, Aditi Kulkarni, Saurabh Mahajan, Pallavi Moghe, Naveen Murthy, Keval Ramani, Shriya Sethuraman, Poorwa Shekhar and Ripudaman Singh, for the much needed fun times I spent with them.

Finally I would like to thank my family; my grandmothers Sushila Sinha and Indira Sinha for their constant words of encouragement over the years; my sister Vanika for always having my back; and my parents Amita and Vikas Sinha who have only encouraged me as I defined and pursued my dreams at my own pace, making more trips to the US than I made to India.

TABLE OF CONTENTS

DEDICATION	ii
ACKNOWLEDGEMENTS	iii
LIST OF FIGURES	vii
LIST OF TABLES	xi
ABSTRACT	xii
CHAPTER	
I. Introduction	1
1.1 Fuel Economy improvements with Autonomous Driving: Literature Review	4
1.1.1 Eco-Driving Methods: Driver Implementation	5
1.1.2 Eco-Driving Methods: Velocity Smoothing	5
1.1.3 Eco-Driving Methods: Pulse and Glide (PnG)	6
1.1.4 Eco-Driving Methods: Potential for Improvements	7
1.2 Modeling and Simulation	8
1.2.1 Fuel Economy Evaluation: Autonomous Vehicles	8
1.2.2 Baseline Human Driving and Constraints	10
1.3 Hypothetical Lead	10
1.4 Velocity Profile Smoothing	12
1.5 Tractive Energy Minimization	13
1.6 Fuel Minimization	16
1.7 Electric Powertrain Modeling	18
1.8 Fuel Cell Hybrids	20
1.9 Thesis Organization	22
1.10 Contributions	22
II. Hypothetical Lead Vehicle Trace	26
2.1 Introduction	26
2.2 Background on Current EPA Fuel Economy Test Procedures	30
2.3 Vehicle Following Model Implementation	30
2.4 Hypothetical Lead Vehicle Profile	34
2.5 Conclusions	37
III. Velocity Smoothing	38
3.1 Introduction	38
3.2 Model and Optimization Constraints	41
3.2.1 Model Description	41
3.2.2 Velocity and Position Constraints	41
3.3 Dynamic Programming	44
3.3.1 Simulation Results	46
3.3.2 Experimental Results	48
3.4 Model predictive control	52
3.4.1 Model predictive control with tracking penalty	55
3.5 Impact of Prediction Quality on Performance	57
3.5.1 Velocity Prediction Algorithm	59
3.5.2 Velocity Optimization using Predicted Lead Velocity	60
3.5.3 Improved Prediction Accuracy	64
3.6 Discussion	70
3.7 Conclusion	71
IV. Optimal Fuel Cost Function Evaluation	72

4.1	Introduction	72
4.2	Optimal Control Problem	74
	4.2.1 Velocity Smoothing by Acceleration and Deceleration Minimization	75
	4.2.2 Tractive Energy Minimization	76
4.3	Drive Cycle Optimization	77
4.4	Full Vehicle Simulation	78
4.5	Case Study I: Downsized Boosted Engine	81
	4.5.1 LA 92 Drive Cycle Optimization	81
	4.5.2 US06 Drive Cycle Optimization	85
4.6	Case Study II: Further Downsized Engine	88
4.7	Case Study III: Naturally Aspirated Full Size Engine	90
4.8	Case Study IV: Electric Vehicles	92
4.9	Fuel Minimization	95
4.10	Discussion	100
4.11	Conclusion	101
V. Electric Vehicle Analysis		103
5.1	Introduction	103
5.2	LA 92 Drive Cycle Analysis	104
5.3	UDDS Drive Cycle Analysis	108
5.4	US06 Drive Cycle Analysis	110
5.5	Road Grade Variation	113
5.6	Electric Powertrain Model	115
5.7	Optimal Control Problem	116
5.8	Results and Discussion	118
	5.8.1 Case Study I : Tesla Model S as an EV	119
	5.8.2 Case Study II: Heavier Mass EV	121
	5.8.3 Case Study III: Proposed Light Weight Military Robot	122
5.9	Case IV: 100% Efficiency in Regeneration	124
5.10	Conclusions	125
VI. Fuel Cell Vehicles		127
6.1	Introduction	127
6.2	System Models	129
	6.2.1 Fuel Cell Model	129
	6.2.2 Battery Model	133
	6.2.3 Component Sizing	134
6.3	Optimal Control Strategy	134
	6.3.1 Dynamic Programming	134
	6.3.2 Dynamic Programming Results	136
	6.3.3 Efficiency Results	137
	6.3.4 Charge Sustaining	137
	6.3.5 Lower Power Demand	139
6.4	Optimal Control Strategy - Thermal Effects	141
	6.4.1 Trajectory Optimization using GPOPS	142
6.5	Battery Thermal Results	145
6.6	Conclusions	148
VII. Conclusions and Future Work		149
7.1	Future Work	151
	7.1.1 Co-optimization	151
	7.1.2 Platoon Formation	151
	7.1.3 Liquid Cooled Fuel Cells	151
BIBLIOGRAPHY		152

LIST OF FIGURES

Figure

1.1	EPA predictions for long term GHG emissions [1].	4
1.2	Fuel economy using various horizons and cost functions in the MPC formulation	13
1.3	Velocity profiles of a section of the original LA92 drive cycle and the optimized cycles. The dashed lines show the velocity profiles of ALPHA simulations which is almost the same as the given trajectories.	14
1.4	The engine operation points of the selected portion of the LA92 drive cycle is plotted on the BSFC map. The solid red lines indicate the operating regions demarcated for residence analysis. A positive number indicates a gain in power optimization over acceleration optimization	15
1.5	The fueling rate is shown to be an approximate linear function of the vehicle power for a selected gear ratio	17
1.6	For two downhill sections of the GEM drive cycle, the optimal trajectory is to swtich off motor and cruise during downhill descent. The optimal strategy is not to brake and utilize the regenerative braking capabilities.	19
1.7	Optimal Fuel Cell operating points for a given velocity trajectory, for the global optimal DP solution and constant power rule based. The difference in hydrogen consumption between the two is only 0.07%	21
2.1	Schematic describes the development of the hypothetical lead (HL) vehicle and the sections of the paper with an example of the HL trace used to evaluate the fuel consumption of a particular following strategy.	28
2.2	Comparison of fuel economy results predicted through the ALPHA model for 2013 Ford Escape with a 1.6L Ecoboost engine. Parameter T is the time headway that a follower vehicle maintains from the lead vehicle. Smaller headway indicates more aggressive following. Aggressiveness in following distances significantly changes the fuel consumption. Standard FTP gives 28.3MPG on the chosen vehicle that is 4.5 m long.	29
2.3	Route selected as the typical morning drive to work in Los Angeles in 1971.	31
2.4	US06 Drive Cycle with the hypothetical lead vehicle trace	36
2.5	First 130s of the UDDS Drive Cycle with the hypothetical lead vehicle trace	37
3.1	Position constraints to be applied on the following autonomous vehicle based on the position and velocity of the hypothetical lead	40
3.2	Table reproduced from [2] which shows the average vehicle spacing based on speed.	43
3.3	DP results with different discretization grid points.	45
3.4	Comparison of standard US06 drive cycle with the DP optimized velocity profile. The fueling rates are found from ALPHA model simulations [3].	46
3.5	EPA defined constraints on velocity required for a certifiable FE test. The DP optimized velocity trajectories adhering to the velocity and position constraints respectively are shown.	47
3.6	The two chassis dynamometer runs are shown in comparison with the simulation results	48
3.7	The chassis dynamometer run is shown in comparison with the simulation results	48
3.8	Experimental results showing changes in different parameters from the standard cycle to the optimized one	50
3.9	SC03 drive cycle accelerations for the SD cycle and the optimized one	52
3.10	Fuel economy using various horizons and cost functions in the MPC formulation	54
3.11	Comparison of standard UDDS drive cycle with DP and MPC ^a velocity traces. Clearly for MPC ^a with $N_p = 4s$, at Time = 530, 605, 655 and 715s the position is too close to the lower bound and the MPC ^a controller applies significant acceleration to stay within the bounds. These accelerations are less pronounced for the $N_p = 8s$ case and absent in the DP case.	55
3.12	Comparison of standard UDDS drive cycle with two MPC filtered velocity traces where the MPC has position tracking in the cost function. Clearly with increased prediction horizon, the position tracking improves. However, the reduction in acceleration between the two MPC cases is small leading to very slight improvement in FE	56

3.13	Comparison of different drive cycles derived from following the hypothetical lead using DP and MPC algorithms with different cost functions at $N_p=4s$. The acceleration profile of DP is the best followed by MPC with velocity tracking, MPC with position tracking, the standard cycle and finally MPC without reference. This is reflected in the the engine torque and correspondingly the fueling rate.	58
3.14	Schematic to show the autonomous vehicle with the hypothetical lead (HL). Future velocity of HL is evaluated using past information of the HL and other lead vehicles in front of it.	59
3.15	Snapshot of optimized autonomous follower at 116s. Clearly, the optimized trajectory is outside the actual position bounds and therefore with new information at 117s, the optimized follower will have to accelerate to stay within the bounds . . .	62
3.16	Snapshot of optimized autonomous follower at 118s. Now the optimized autonomous follower is within the actual position constraints and hence further acceleration is not required and the optimized trajectory further in the horizon can be realized . .	63
3.17	Linear and quadratic fits for a selected section of the UDDS drive cycle	64
3.18	Increasing the number of lead vehicles does not improve FE, in fact it results in FE falling significantly below the baseline	65
3.19	The speed prediction error in the 1 st second and the 10 th second are shown for 1 vehicle and 10 vehicles. Clearly, in the 1 st second, the prediction error with 10 lead vehicles increases significantly, while the prediction error drops significantly in the 10 th second.	66
3.20	RMS Error at different prediction seconds for the unweighted and weighted cases . . .	67
3.21	Artificially decreasing error in the first prediction second, still results in a lower FE than with decreasing error in the last prediction second. Similar results are shown with the reverse case	68
3.22	Artificially decreasing error in the first prediction second, still results in a lower FE than with decreasing error in the last prediction second. Similar results are shown with the reverse case	69
3.23	Constant velocity and constant acceleration velocity predictions for a section of the UDDS drive cycle	70
4.1	Velocity trajectories of the standard LA92 drive cycle with the velocity smoothing and tractive energy minimized trajectories. The solid lines show the desired velocity trajectory while the dashed lines show the actual trajectory traversed by the vehicle in ALPHA simulations. Clearly all velocity trajectories are reasonable and can be achieved in full vehicle simulations.	78
4.2	The velocity trajectories of the standard LA92 drive cycle along with the velocity smoothing and tractive energy minimized trajectories. Clearly the optimized trajectories are much smoother than the standard cycle and avoid frequent accelerations and decelerations.	80
4.3	The engine operation points of the selected portion from 850s to 950s of the LA92 drive cycle is plotted on the BSFC map [4]. The solid red lines indicate the operating regions demarcated for residence analysis. A positive number indicates a gain in tractive energy optimization over velocity smoothing.	82
4.4	The vehicle velocity and acceleration are plotted for the selected portion of the LA92 drive cycle from 840 – 970s. The tractive power at the wheels and the engine power are also shown. During the phase of low rate of deceleration, the engine is either idling or providing limited power. The plots for engine torque and engine speed show that at these points, the engine operates at high speed and low torque which is highly inefficient.	84
4.5	Velocity traces for the standard and optimized US06 drive cycles. As expected for the energy minimization cycle, higher rates of acceleration, long periods of low deceleration cruising and short high deceleration are observed.	86
4.6	Velocity traces for the selected portions of the standard and optimized US06 drive cycles and the ALPHA simulated velocities. The three time periods of 490 – 525s, 525 – 540s and 540 – 560s are demarcated in the plot.	86
4.7	Three consecutive parts of US06 drive cycle with the operating regions demarcated. A pink square and a green circle shows a higher energy and fuel demand respectively for the velocity smoothing case, while a black square and a yellow circle shows a higher energy and fuel demand respectively for the tractive energy minimization case. The size of the square and circle are proportional to the percentage gain over the other drive cycle.	87
4.8	US06 drive cycle for a production 1.6L EcoBoost engine and a downsized version of the engine. For the downsized case, the available torque is reduced and to generate equivalent power, a higher engine speed is required. The full-size engine fuel maps are experimentally determined from [4].	89
4.9	US06 drive cycle for a the 4.3L Chevrolet Ecotec engine. The low power cruising in the power optimization case reduces the cylinder deactivation time and hence increases the fuel consumption.	91
4.10	Distribution of efficiency of operating points and demanded power from both the conventional engine and the electric motor.	93

4.11	Equivalent power in fuel and battery as supplied to the engine and motor respectively for the selected portion of the US06 drive cycle. The fuel power is much higher due to the maximum 35% efficiency in a conventional engine.	94
4.12	Trapezoidal velocity traces are shown with equal constant velocity cruising duration. On the right BSFC map, the engine operating point at the different constant velocity cruising and FE are shown.	96
4.13	Gear shifting strategy with hysteresis based on the optimal BSFC operating points	97
4.14	Validation of gear map with ALPHA results	98
4.15	Full vehicle model schematic	100
5.1	Motor Torque and Motor Current distribution for LA92 drive cycle while traversing the standard and optimized velocity traces. The optimized trace clearly has a lower torque demand that is further reflected in lower motor current. This trend was observed for both positive (propulsion) and negative (braking) sides	105
5.2	Velocity traces for the standard and optimized drive cycles in the first 120 s of LA92 drive cycle, with the Battery Energy consumed in that time period. Between the solid black lines the standard cycle accelerates, decelerates and accelerates again at a high rate while the optimized cycle accelerates slowly to reach the same velocity. In this period the optimized cycle consumes 55.5 kJ less battery energy.	107
5.3	MPGe for different velocity traces found using a range of prediction horizons with different MPC formulations for the UDSS drive cycle. The constant black and purple lines indicate the MPGe for the standard and DP optimized drive traces. For shorter prediction horizons, MPC without tracking does not work at all and tracking has to be introduced to improve results exactly like the conventional vehicle. Velocity tracking performs better than position tracking, but with longer prediction, the no tracking case improves MPGe significantly	108
5.4	Probability distribution of the motor power and motor efficiency in propulsion for the standard and optimized US06 drive cycles. While from previous results it was assumed that the optimized US06 trace would operate for longer at lower motor power, the interesting result is in the motor efficiency. Operating at lower power reduces the motor efficiency.	110
5.5	Selected portion of US06 drive cycle where the SOC for the optimized cycle is higher in some cases than the standard cycle.	112
5.6	Three different vehicle cases are considered in this paper with varying power to weight ratios. The first two cases are run for EPA's GEM drive cycle while Case III is run over steeper military grades. For each case, three different constraints are applied all of which force the optimal velocity to traverse the given distance in the same time as constant speed lead. Regenerative braking was observed as part of the optimal solution only in cases where constraints were imposed. The motor energy demand reduction over the baseline for the optimized cycles are also shown in bold.	114
5.7	The efficiency of the regenerative braking system is determined by the powertrain and generator efficiency. Also, braking power beyond the generator torque and power limits, shown by the thick black solid line is dissipated as heat, which reduces efficiency further at high loads and speeds.	116
5.8	The vehicle velocity for the constant velocity 55 MPH standard cycle of constraint I and the distance constrained optimized cycle of constraint II are plotted on the left y-axis. The altitude is shown on the right y-axis. The distance constrained optimal velocity was able to reduce the motor energy demand by 3.2% over the constant velocity case.	118
5.9	Magnified plots of the vehicle velocity and motor power while the vehicle descends downhill. In both constraint cases, while the constant speed standard cycle brakes to maintain speed on the negative gradient, the optimal policy is to avoid braking and coast. When the negative slope is low, the vehicle velocity reduces but when the negative slope increases, the vehicle velocity increases as well.	120
5.10	The plot on the left shows the motor power and vehicle velocity with time varying tight constraints of constraint II, while the plot on the right shows the case with only the initial and final constraints of III are applied. Due to the tight constraints on the left, the double mass case brakes to meet them while on the right the velocity is allowed to increase more.	121
5.11	When the DP optimization is carried out for the small 1000lb robot in case III, optimized velocity trajectory obtained through constraint III shows a reduction of 24.2% over the constant speed standard cycle of constraint I.	123
5.12	If the round-trip regeneration efficiency is assumed to be 100%, the optimal policy does include several braking events while descending downhill.	125
6.1	Fuel cell polarization curve and power output per cell normalized by cell active area. The fuel cell output power increases with current, and peaks when the voltage drops below a critical value.	131

6.2	Fuel cell system efficiency including power to drive the fan and regulate the stack at a given temperature assuming an ambient temperature of $25^{\circ}C$. The black dashed line indicates the optimum efficiency line for the system as a function of net power and the corresponding stack temperature. The white region in the lower right hand corner of the figure is the set of net power and temperature for which steady state operation is infeasible. That is the cooling power is greater than the stack output at these low temperatures and high operating current.	132
6.3	Optimal power split between the fuel cell and battery for a given power demand as shown above. Three different SOC ranges are shown that limit the battery energy to approximately full, half and quarter.	135
6.4	Operating points of the fuel cell on the efficiency curve for different battery energy with a 3 cell stack.	137
6.5	Energy demand from different components for full and quarter battery	138
6.6	Charge Sustaining case for the highly variable WLTP drive cycle	139
6.7	Charge Sustaining case for WLTP with half power demand.	140
6.8	Optimal power split between the battery and fuel cell for traversing the Churchill B cycle with the given power demand and the optimal operating points of the Fuel Cell found from DP with the constant operating point of the rule-based solution.	141
6.9	Optimal system trajectory for a medium sized battery. The fuel cell and battery delivery roughly equal power to the load.	143
6.10	Optimal system trajectory for a small battery (quarter sized). Even for this relatively small battery, the optimal solution tends to avoid charging the battery with a monotonically decreasing SOC profile. Since the stack operating temperature is near the limit, the cooling flow cannot be decreased at the end of the cycle. When the fuel cell stack is resize as shown in the right plot from 3 to 7, the cooling requirements reduce and allow the cell to operate at the peak efficiency point.	144
6.11	Schematic of Fuel Cell with battery thermal states included	145
6.12	After the addition of the battery thermal state, an additional constraint is imposed on the maximum battery temperature. Within the optimization, rising battery temperature prevents a complete battery discharge.	146
6.13	Final battery temperature constraints are raised to $90^{\circ}C$. In the left plot with final SOC at 0.5, the battery is discharged to its maximum level without hitting the temperature constraints. On the right plot with the final SOC at 0.1, the battery cannot be discharged as it hits the maximum temperature constraint.	147

LIST OF TABLES

Table

1.1	Comparison of fuel economy results of different following strategies	9
2.1	Influence of time headway on fuel economy over the UDDS	29
2.2	Parameter Definitions	32
2.3	Parameter Value	37
3.1	Raw Experimental Results	49
3.2	Fuel Economy Improvements	57
3.3	Prediction Quality Performance	61
4.1	LA 92 drive cycle optimization results	81
4.2	Comparison between optimized drive cycles in different modes for LA92 and US06 drive cycles. US06 results are in parentheses.	85
4.3	US06 Drive Cycle optimization results	86
4.4	US06 Drive Cycle optimization results for selected 3 parts	88
4.5	Vehicle Model Parameters	98
5.1	Vehicle Parameters	116
6.1	Fuel Cell Parameters	130
6.2	Battery to trip energy ratio. Average dynamic efficiency and H_2 consumption. . .	141
6.3	Increasing trip time, with increasing trip energy demand	146

ABSTRACT

The emergence of self-driving cars provides an additional flexibility to the vehicle controller, by eliminating the driver and allowing for control of the vehicle's velocity. This work employs constrained optimal control techniques with preview of position constraints, to derive optimal velocity trajectories in a longitudinal vehicle following mode. A framework is developed to compare autonomous driving to human driving, i.e. the Federal Test Procedures of the US Environmental Protection Agency. With just velocity smoothing, improvements by offline global optimization of up to 18% in Fuel Economy (FE), are shown for certain drive cycles in a baseline gasoline vehicle. Applying the same problem structure in an online optimal controller with 1.5 s preview showed a 12% improvement in FE. This work is further extended by using a lead velocity prediction algorithm that provides inaccurate future constraints. For a 10 s prediction horizon, a 10% improvement in FE has been shown.

A more conventional procedure for achieving velocity optimization would be the minimization of energy demand at the wheels. This method involves a non-linear model thus increasing optimization complexity and also requires additional information about the vehicle such as mass and drag coefficients. It is shown that even though tractive energy minimization has a lower energy demand than velocity smoothing, smoothing works as well if not better when it comes to reducing fuel consumption. These results are shown to be valid in simulation across three different engines ranging from 1.2 L-turbocharged to 4.3 L-naturally aspirated. The implication of these results is that tractive energy minimization requiring more complex control does not work well for conventional gasoline vehicles. It is further shown that using reduced order powertrain models currently found in literature for velocity optimization, can result in worse FE than previous optimizations. Therefore, an easily implementable, vehicle agnostic velocity smoothing algorithm could be preferred for drive cycle optimization.

Employing these same velocity optimization techniques for a battery electric vehicle (BEV) can increase battery range by 15%. It is further demonstrated that eco-driving and regenerative braking are not complimentary and eco-driving is always preferred. Finally, power split optimization has been carried out for a fuel cell hybrid, and it has been shown that a rule-based strategy with drive cycle preview could match the global optimal results.

CHAPTER I

Introduction

Optimal control theory has been extensively employed in solving the classical Goddard problem, of finding the optimal trajectory that minimizes fuel consumption for the vertical climb of a rocket [5]. This problem from 1920 is suddenly relevant again as, these rockets were autonomous or teleoperated by pilots that followed a predefined optimal trajectory as advisory [6]. The growth of interest in autonomous vehicles, where vehicle controllers have the added ability to drive a velocity trace and not be dependent on driver commands, opens new frontiers in their velocity optimization.

Automated vehicles have been envisioned since the Futurama exhibition organized by General Motors (GM) in 1939 [7]. While the exhibition is remembered for initially presenting the now achieved goal of designing a fast and safe network of highways, engineers also presented the concept of an automated highway system. The first steps towards testing self-driving cars on public highways have been conducted for vehicle platooning over the last two decades. In the United States, under the National Automated Highway System Consortium (NAHSC) project, actual road testing of vehicle platoons were carried out where the lead vehicle operated by a driver was followed by autonomous vehicles controlled by their own internal controllers [8]. In Europe, a more recent similar exercise was conducted under the Safe Road Trains for the Environment (SARTRE) program in 2009 [9]. The primary motivations for both these projects was increased road safety by eliminating the driver and fuel economy benefits from reduced aerodynamic drag coefficients.

Individual vehicles with the ability to drive by themselves have been explored as well, with the Google self-driving car being the most well known attempt. The company claims to have driven for more than 4 *million* miles autonomously, without

an accident attributable to their vehicle control systems [10]. A 2014 survey of self identified experts in vehicle automation found a median estimate of 2019 for when vehicles would be able to drive themselves on freeways with a driver to take control only if needed [11]. This thesis is being written in 2019 and to the best of the author's knowledge, a vehicle has yet to be launched on public roads without a safety driver.

However, in recent years for lower levels of autonomy, the electric vehicle manufacturer Tesla has launched its auto-pilot feature which allows for multiple vehicle controls such as speed and steering simultaneously [12]. The company still advises drivers to remain conscious of road conditions with the ability to immediately intervene and supersede auto-pilot controls as needs arise. Recent announcements by traditional manufacturers Ford [13] and GM [14] also point to a future where cars with at least some high level of automation beyond adaptive cruise control would inevitably be sold to the general public fairly quickly.

An analysis in 2017 [15] from a business standpoint concludes that autonomous vehicles will disrupt the present automotive business and move consumers from self-owned vehicles to riding as a service business model. The conclusion from that analysis forecasted that autonomous vehicles will be the majority of the vehicles on the road by 2030. However, a more realistic, if conservative view was taken in the February 2018 editorial of Society of Automotive Engineer's (SAE) Automotive Engineering issue. Quoting several experts in the field, editor Bill Visnic cautioned against undue optimism and concluded it will be at least a decade's wait before fully autonomous vehicles hit the road [16]. Even if we are skeptical of both these optimistic predictions, autonomous vehicles are the inevitable future of the automotive industry.

Presently, the two major motivations driving the pursuit of individual autonomous vehicles are 1) Safety and 2) Reduction of driver time wasted in traffic. Safety is a major motivation given current trends that show, traffic accidents are already the leading cause of deaths for children and young adults aged 5–29 years [17]. According to a survey by the US Department of Transportation (DoT) the critical reason for a vehicle crash can be attributed to the driver in 94% of vehicle crashes, indicating a tremendous opportunity for potential accident reduction [18]. The second motivation is driven by the productivity that is lost by vehicle drivers in commuting, as they have to concentrate on driving and cannot be engaged in other activities [19].

While the ease of driving in autonomous vehicles is certainly a desirable goal, it could also lead to an increase in the overall vehicle miles driven and hence increase the global environmental burden of transportation. An additional potential drain resulting from autonomous driving applications are the energy costs of sensors and on-board computers. A good LIDAR sensor such as the Velodyne, HD-L 64E, used extensively in autonomous vehicle applications, draws at an average of approximately 60 W of electric power [20]. From some preliminary research, about 6 such units would be required for each vehicle. Additionally, the NVIDIA Xavier AI supercomputer designed for implementation in autonomous driving applications, and shown to have 75% less power demand than other such units, still draws approximately 20 W of constant power from operation [21]. According to my simple derivation of these requirements, the cumulative electric energy demand from these devices can be significant and can lead to an increase in battery energy demand of 2%, 4% and 6% over the US06, LA92 and UDDS drive cycles respectively, for a Tesla Model S. Hence, the increase in power consumption due to vehicle automation has to also be offset through some methods.

Having stated all of the above, a collateral benefit of autonomous vehicle technology is the elimination of the driver from the control loop. Now, the vehicle velocity can be set to a desired level by the vehicle controller itself. There are significant fuel economy benefits to be gained by driving optimal velocity traces that reduce fuel consumption [22]. This thesis assesses the potential benefits of utilizing self-driving technology for fuel consumption. Improvements to fuel economy are extremely important from a societal standpoint, as increased CO_2 emissions due to human activity have resulted in unprecedented concentration of green house gasses (GHGs) in the atmosphere [23]. To mitigate the potentially catastrophic effects of a warmer planet, significant cuts to present emission levels are required. Light duty vehicles contribute approximately 60% of all transport related GHG emissions [24]. In Fig. 1.1 business-as-usual refers to the standards from 2012-2025 and then maintaining the 2025 standards in the future. A 4.5% annual rate of improvement yields GHG emissions closer to the IPCC projection to limit temperature rise to 2 C.

According to the emission standards set by the National Program on light-duty vehicles from Model Year (MY) 2012-2025, the US Environmental Protection Agency (EPA) predicts a 6 billion metric ton reduction through life cycles of vehicles sold

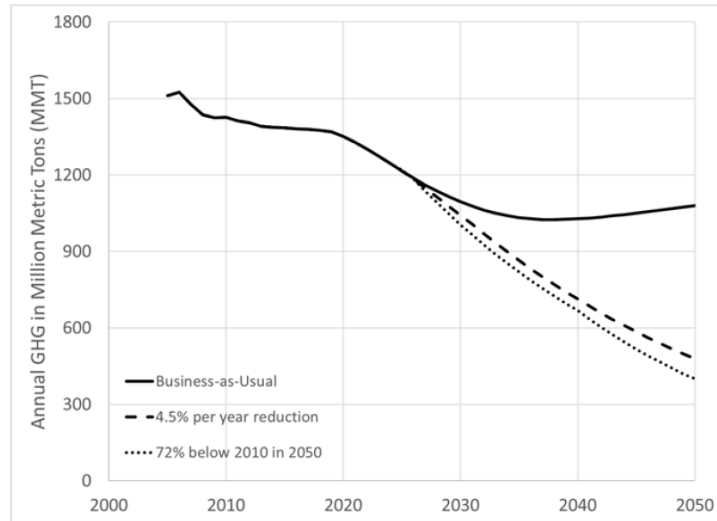


Figure 1.1: EPA predictions for long term GHG emissions [1].

from 2012-2025 [1]. In their mid-term evaluation for the proposed rule [25], EPA presents an optimistic view of being able to meet these standards at potentially lower than initially projected costs through present technological pathways.

However, beyond the standards set for 2025, EPA projects a need for further improvements in fuel economy to substantially reduce emissions further. As shown in Fig. 1.1, billions of metric tons of GHGs can be reduced by improving Fuel Economy (FE) after 2025.

1.1 Fuel Economy improvements with Autonomous Driving: Literature Review

In the EPA mid term evaluation, while a number of improvements and potential pathways for present technologies are mentioned, there is also an analysis of potential future technologies that are presently either absent or not widespread. Automated driving is thought of as an exciting future technology that has significant potential for reducing fuel consumption. Clearly the potential for increasing fuel economy through the use of computer generated drive cycles rather than human derived pedal commands is significant. A recent comprehensive analysis of the benefits and disadvantages of autonomous vehicles warned policy makers ”..to consider early steps to mitigate the negative outcomes and encourage the realization of its potential benefits

[26].”

1.1.1 Eco-Driving Methods: Driver Implementation

According to the literature, improvements from 10% to 50% are possible through drive cycle optimization. A comprehensive review of all extant eco-driving techniques is offered in [27] covering eco-driving optimal control problems across conventional, hybrid and electric vehicles. In the absence of autonomous driving, driver feedback has been used to encourage eco-driving. It was shown very early on, in 1978, that drivers could save fuel by manipulating vehicle speed [28]. In one study of 20 drivers, an improvement of 6% was found in city driving and 1% in highway driving [29]. Another study tried to improve driver behavior for bus drivers and reported 10 – 15% savings in overall fuel consumption [30]. By applying eco-driving or trace smoothing techniques while driving [31], a reduction of almost 33 million metric tons of CO_2 has been predicted. All these cases assume a human driver and that driver’s implementation of eco-driving techniques. As the analysis in [32] concluded, the success of eco-driving techniques depends most heavily on driver acceptance, unlike other more technological improvements.

1.1.2 Eco-Driving Methods: Velocity Smoothing

By eliminating the driver and shifting to autonomous vehicles, the driver training step can be completely removed. In this implementation, the existing vehicle platforms can be driven on better velocity profiles which would significantly improve FE. The ultimate FE minimization can be achieved with 100% autonomous vehicle penetration, where full traffic flow management will also be possible. Until then, in the near future only a moderate penetration of autonomous vehicles is expected where they can encounter other human driven vehicles. Hence, the lead vehicle velocity needs to be taken into account while constructing the current optimal velocity profile for an autonomous vehicle. Appropriate safety as well as traffic constraints have also got to be applied such that the following distance is long enough to be safe but at the same time not too long to allow for cut-ins from other lanes.

Looking at the literature for algorithm driven vehicles, authors in [33] used an algorithm to match the speed of a preceding vehicle after a given prediction horizon. While they were able to show more than a 50% improvement in FE with a 30s preview, in many drive cycles they showed a decrease in fuel economy, indicating

no guarantees on optimality with their algorithm. Moreover, no distance constraints were applied from the preceding vehicle thus leaving the autonomous vehicle liable to crashes, rendering the algorithm unsuitable for practical application. A similar attempt was made in [34] that reduced velocity fluctuations while following the UDDS drive cycle, but in that case again no distance constraints were applied and the autonomous vehicle would in some cases overshoot the UDDS vehicle or fall behind by almost 300 m. Using a DP optimization for free flowing and constrained flow [35] was able to achieve a 34% improvement in free traffic flow and 15.4% improvement in constrained flow where a safety distance had to be maintained from the preceding vehicle. However, no mention was made of the maximum distance from the preceding vehicle. Also that work used offline optimization with the entire drive cycle preview which is not practical.

For an online implementation, a Model Predictive Control (MPC) formulation was used in [36], that showed an 8.8% reduction in fuel consumption with a 5 s preview. However, those authors used their own drive cycles as the baseline and did not show how the controller would perform under known and regulated conditions. Additionally they employed a fixed distance constraint unlike in the real world where the distance from the preceding vehicle depends upon the relative velocity. This would result in awkward traffic patterns.

1.1.3 Eco-Driving Methods: Pulse and Glide (PnG)

Another velocity manipulation technique that delivers lower energy demand than simple velocity smoothing is Pulse and Glide (PnG). This strategy, where the vehicle velocity switches between acceleration and coasting, with the engine switched off during coasting, was implemented in [37]. They reported between 33 – 77% improvements in simulation as compared to a constant speed driving for a conventional vehicle. The PnG strategy is only a theoretical concept for conventional vehicles where the engine cannot be switched off in an automatic transmission while the vehicle is in motion. But with actual experimental testing on a chassis dynamometer, they report 24 – 90% improvements in fuel economy. This work was carried forward in [38] where instead of comparing to a constant velocity case, comparisons were made between a benchmark LQ-based controller and PnG strategy in a vehicle following case. They reported improvements of up to 20% over the baseline. In [39]

a mixture of car following strategies was shown to be the optimal method in minimizing fuel consumption. From an optimal control algorithm, the results showed that the strategy shifted between constant speed and pulse and glide depending on the speed of the preceding vehicle. When the speed was high, PnG was used while for a low lead speed, constant speed cruising was used. While PnG has a lower energy demand than the previous cases, this method only works well in hybrid systems where the engine can be shut off during coasting. Additionally, the lead vehicle in all these cases has a constant speed, which is unreasonable for real world scenarios. When a more naturalistic drive cycle was adopted in [38] a significant spread over the uniform results was reported.

1.1.4 Eco-Driving Methods: Potential for Improvements

From the literature review, it is clear that significant improvements to FE can be achieved using velocity trajectory optimization. Even relatively simple algorithms were able to deliver substantial results. However, one reason for the considerable deviations in results is the differing baselines of human driving. Traditionally, standard drive cycles from the US Environmental Protection Agency’s (EPA) such as the UDDS, US06, LA92 etc are used to evaluate the fuel economy baseline. This work will develop a framework to compare drive-cycles of autonomous vehicles to human driving, as represented by the standard EPA drive cycles. The present EPA fuel economy evaluation framework of using 1-D velocity traces to represent different driving conditions will be preserved. Another issue with the literature, was the constraints imposed on the following distances, which were either absent [34], static [36] or did not take into account a maximum distance [35]. For this work, the minimum and maximum following distances, have been defined based on the lead vehicle speed. These distances come from studies conducted by the US Department of Transportation of car following in a tunnel [2]. With the baseline framework set, this work will then evaluate the benefits of velocity manipulation while navigating traffic.

The fuel economy results shown in this work come from simulations performed in the Advanced Light-Duty Powertrain and Hybrid Analysis Tool (ALPHA), developed at the US Environmental Protection Agency (EPA). This well validated model simulates a vehicle tracking any given 1 Hz velocity trajectory [3]. The forward simulation software attempts to mimic vehicle testing on a chassis dynamometer.

A driver model within the software evaluates pedal position based on present and future speed which is translated to an engine torque. This engine torque is converted to a force on the wheels while accounting for the losses in the powertrain including torque converter clutch and gear shifts. The force on the wheels along with road load and aerodynamic drag on the vehicle is used to evaluate the acceleration and hence the velocity of the vehicle. The software flags any velocity trajectory that cannot be followed by the vehicle within the EPA defined limits of deviation and hence ensures the feasibility of the velocity trajectory.

The vehicle selected for primary evaluation was a 2103 Ford Escape with a 1.6L EcoBoost engine. This vehicle was extensively studied and validated for ALPHA thus giving confidence to our simulation results. Moreover, the downsized boosted engine is now an efficient engine technology that has increased its market share from 3% in 2008 to 22% in 2016 [4]. All gains shown would be over this already efficient and commercialized engine.

All the optimized drive traces will also be simulated in ALPHA for an electric vehicle, a 2013 Tesla Model S. The goal of this analysis is to show the potential benefits of optimized drive traces in electric vehicles by reducing the battery energy demand and thus offering a longer range for the same battery size. Additionally, we can make comparisons with conventional vehicles to understand the relative benefits of different strategies for varied powertrains and provide insight into which strategy fits with which technology.

The last section of this work deals with the optimization of fuel cell hybrids [40]. A complete scalable, Fuel Cell (FC) model is constructed that accounts for the parasitic losses in cooling to maintain a relatively low (70 °C) FC temperature [41]. The FC is hybridized with a battery and the optimization is for the power split between the two power sources as well as for component sizing. In this manner optimal operating points of the FC can be obtained as the hybrid vehicle traverses a velocity trajectory.

1.2 Modeling and Simulation

1.2.1 Fuel Economy Evaluation: Autonomous Vehicles

Human car following scenarios that approximate various traffic conditions have been investigated extensively in traffic simulation literature [42]. In this field, the Intelligent Driver Model (IDM) [43], which incorporates parameters for comfortable

Time Headway T (s)	Gap (car-length)	Fuel Economy (MPG)	Difference From Baseline UDDS (%)
0.90	1.00	27.6	-2.5
1.25	1.33	28.0	-1.1
1.70	1.80	28.3	0.0
2.50	2.67	28.6	+1.1
3.90	4.00	29.4	+3.9

Table 1.1: Comparison of fuel economy results of different following strategies

braking, speed-determined following distances and allowing for differences between desired and actual following distances, was shown in [44] to have the least RMS errors in predicting actual data. The tunable parameter for time headway T in IDM determines how closely the lead vehicle is tracked as shown in Table 1.1. It can be seen that with increasing, T , the following gap increases and in doing so, the resulting fuel economy increases as well. The results are shown for vehicles following the EPA’s Urban Dynamometer Driving Schedule (UDDS) test cycle. From the fuel economy numbers mentioned in the legend, it is clear that aggressiveness or lack thereof in following determines the fuel consumption to cover approximately the same distance in the same time. In fact the FE of a standard UDDS for the given vehicle is 28.3 MPG. An aggressive following of 0.9s resulted in worse fuel economy than the UDDS¹, while a more relaxed following of 3.9s resulted in an improvement in FE over the UDDS. Therefore, we can conclude that an improved FE is not an inevitable consequence of autonomous driving.

Even in human driving, the role of aggressive driving on FE was investigated in a news report [45] which found a 31% difference between moderate and aggressive driving. A more comprehensive investigation of driving behavior by the University of Michigan Transportation Research Institute (UMTRI) found a 13% and 16% difference in fuel economy between the mean and the 10th and 90th percentile drivers respectively. A total of 117 selected drivers over a period of more than a month on similarly instrumented vehicles for the study [46]. These results indicate that a simple adaptive cruise control (ACC) type of following strategy with an aggressive time headway can actually perform worse than the lead vehicle. Clearly, we cannot just assume that autonomous vehicles will improve FE beyond human driving but it has to be encouraged.

¹In this analysis we do not account for the reduction in aerodynamic drag that can be achieved with close vehicle following

1.2.2 Baseline Human Driving and Constraints

As mentioned in the Introduction, the primary motivation compelling car manufacturers to improve FE standards is the tightening regulatory control, and in this context improving regulatory policies for autonomous driving strategies that improve FE are crucial. As illustrated by Table 1.1, there is a trade-off between fuel consumption and distance maintained from the preceding vehicle². The figure shows the following distance at different speeds for vehicles following a UDDS drive cycle using the Intelligent Driver Model (IDM) by applying a range of time headways (T). Hence the distance constraints have to be applied such that the autonomous vehicle is both at a safe distance from the lead, and not so far behind that it results in other vehicles cutting-in and hence abruptly changing the optimal velocity profile.

Another issue with evaluating autonomous vehicle’s fuel economy is to compare it with human driving. The standard EPA drive cycles presently used to estimate fuel economy provides a range of real world speed profiles for a host of different traffic conditions. All these velocity traces have been derived from actual human drivers navigating traffic. For example, the UDDS drive cycle was developed in 1971 when six drivers drove a given route in Los Angeles in the same car. According to the authors in [47], five of them were remarkably similar. From these an actual trace closest to the mean of all traces was selected as the UDDS. Similarly for the development of the Highway Fuel Economy Test (HWFET), drivers were instructed to follow traffic [48]. From these it can be concluded that the present drive cycle used for FE evaluation are actual human drivers following traffic for different road and speed conditions.

In the following sections a short summary of various topics raised in this thesis are presented along with some results.

1.3 Hypothetical Lead

Using these drive cycles as baseline human driving, this work develops the concept of a hypothetical lead (HL). This hypothetical lead can be generated from any given test cycle that can simulate the traffic conditions and provide position constraints for the following vehicle. These constraints can then be exploited by an autonomous driving algorithm to achieve the highest possible fuel economy within them. For a

²Again without considering the reduction in aerodynamic drag

consistent comparison to human driving, these EPA driving profiles would provide an appropriate estimate of the benefits of autonomous driving.

With the valid assumption that these standard drive cycles are derived from following actual traffic conditions, to recreate those traffic conditions, an inverted form of the IDM equations were used to determine the velocity profile of the hypothetical lead. Here the follower vehicle velocity is assumed to be the input and the lead velocity the output. The concept of the hypothetical lead and its derivations has been presented in our ACC paper [49]. The hypothetical lead would thus represent an approximation of all traffic conditions encountered by drivers of these standard drive cycles. By following this hypothetical lead with optimization algorithms, a consistent comparison can be made between humans and automated driving navigating the same traffic conditions.

Apart from being able to simulate different traffic conditions as a lead velocity trace, the hypothetical lead also provides us with the ability to define position constraints on the following autonomous vehicle. The position of the autonomous vehicle is constrained by an upper bound, the closest the autonomous vehicle can get to the lead, and a lower bound, the furthest distance it can fall behind the lead without allowing cut-ins. The upper bound is defined as being 1 car length for every 10 MPH and the lower bound as 4 ft/MPH. The upper bound is determined from a common recommended safety distance [50] and the lower bound from the results presented in a US Department of Transport study on traffic flow theory [2]. The lower bound was further relaxed at low speeds of less than 20 MPH to reduce frequent starts and stops as it can be assumed that cut-ins are reduced at lower speeds. Additionally, following vehicles can ease to a slower stop when the preceding vehicle slows down.

The constraint framework in this way ensures that the autonomous vehicle has to cover the same distance in the same time as human driving. The constraints allow for velocity deviations from the human velocity trajectory. With the baseline framework defined above, the constraints on the autonomous vehicles are the time varying position constraints. Different optimization algorithms can be applied that use the flexibility given by the upper and lower position constraint to optimize the drive cycle so as to either drive a smoother trace or drive engine loads that are more efficient.

1.4 Velocity Profile Smoothing

The first step to optimizing the velocity trace of an autonomous vehicle as evidenced in the literature is velocity profile smoothing or trace smoothing. The idea of trace smoothing is to minimize fluctuations in velocity, or in other words reduce the total accelerations and decelerations as the vehicle moves through the constraints. Applying this method, a better velocity profile than human driving can be found without any information of vehicle characteristics such as mass or aerodynamic drag. A section of the LA92 drive cycle with a smoothed profile is shown in Fig. 4.1.

A simple double integral model was used for this optimization involving two states of position and velocity and the acceleration as the input. The cost function in this case was the square of the input, thus encompassing both the acceleration and deceleration. The simplicity of the model allowed for computational efficiency. Initially an offline Dynamic Programming (DP) optimization was done to find the globally optimal solution [51]. Using the DPM algorithm [52], the position and velocity in time at minimal cost was found. While there is no direct involvement of vehicle parameters in the above optimization, or any attempt to reduce energy demand, a positive effect of reducing accelerations is a reduced propulsive or tractive power demand from the engine thus reducing fuel consumption. The benefit of reduced decelerations is smaller energy loss in braking. Therefore it was not surprising to find that vehicle simulations on these optimized traces through ALPHA, yielded significant improvements in fuel economy of up to 18% in the LA92 drive cycle. These results serve as the upper bound on what is possible by trace smoothing for more realistic online implementations.

Since in the previous optimization formulation, the model is linear with linear constraints and a quadratic cost, it is ideal for online implementation in the Model Predictive Control (MPC) framework. This methodology allows for forward optimization given a preview of a reference signal or constraints. This work evaluated the effectiveness of MPC given different previews. It was found that across all drive cycles, with a 20 s prediction horizon, the MPC results matched those produced by offline DP. However, 20 s is an unreasonably long prediction horizon and the FE with prediction horizon is shown in figure 3.10. For very short prediction horizons, less than 5 s, the optimized traces in MPC^a showed a worse fuel economy than the base-

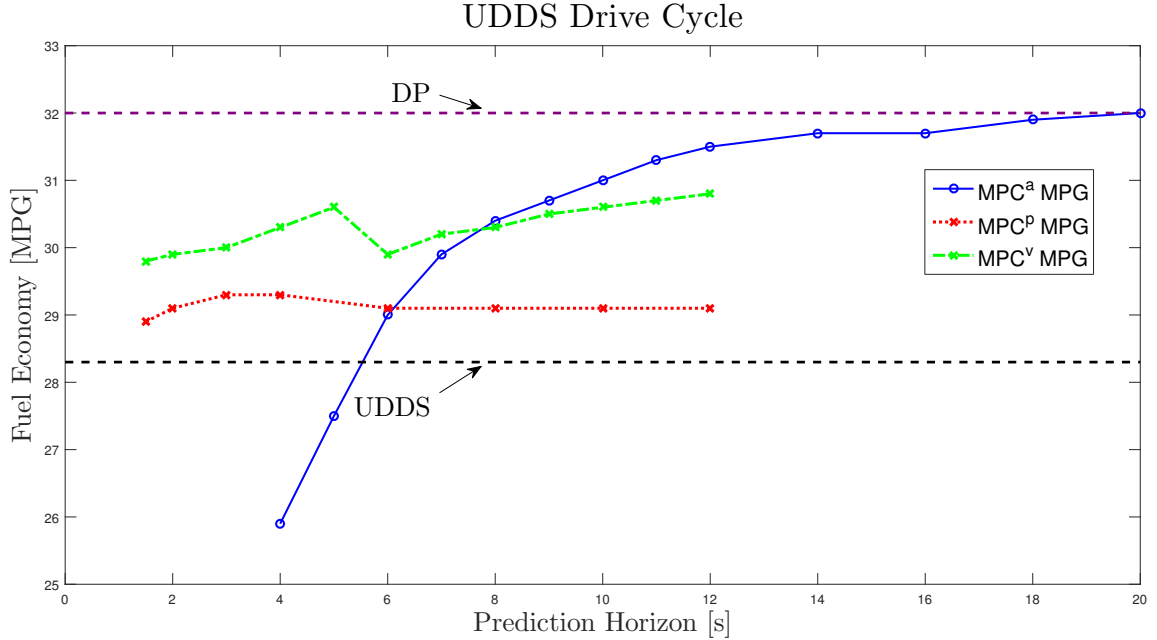


Figure 1.2: Fuel economy using various horizons and cost functions in the MPC formulation

line UDDS. This was due to the position falling too close to the lower bound thus forcing a high rate of acceleration that worsened fuel economy. To overcome this problem, MPC^p and MPC^v were formulated to track the upper bound on position and velocity of the lead respectively. As shown in the figure 3.10, for shorter prediction horizons these performed better, but reference tracking limited their scope for optimization with longer prediction horizons. For just a 1.5 s preview, an improvement of up to 12% was found in the US06 drive cycle. This work was presented at DSCC 2016 [53]. Extending this work further, an analysis has also been carried out by using a prediction algorithm that provides inaccurate preview of lead velocity. With inaccurate predictions a for a 10 s preview a 10% improvement in FE was shown.

1.5 Tractive Energy Minimization

After the straightforward optimization of the velocity trajectory was done to minimize velocity fluctuations while adhering to the position constraints, a logical next step was to minimize the total energy demanded at the wheels while adhering to the same position constraints. This follows from several similar examples in the literature where the minimization of fuel consumption is done indirectly by minimizing the requested power [36, 54, 55]. It was hoped that by this logic minimizing the to-

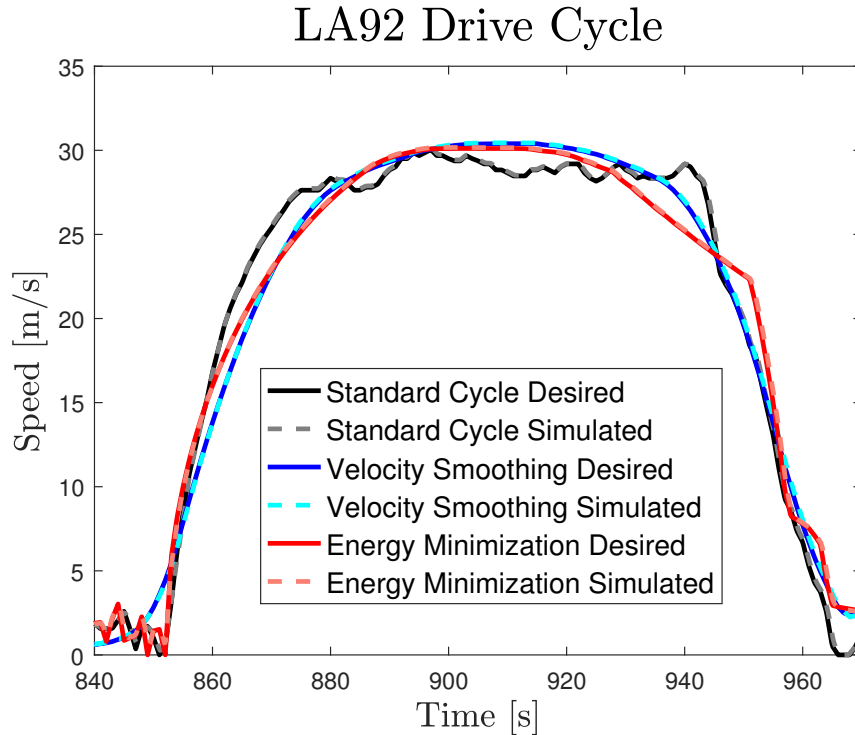


Figure 1.3: Velocity profiles of a section of the original LA92 drive cycle and the optimized cycles. The dashed lines show the velocity profiles of ALPHA simulations which is almost the same as the given trajectories.

tal energy demanded at the wheels would result in an even lower fuel consumption. However, the results were counter intuitive and it was found that while in some cases the fuel economy did improve as compared to the acceleration optimization case, a reduction of energy demand did not guarantee a reduction in fuel consumption.

The resulting velocity profile from tractive energy minimization for a part of the LA92 drive cycle is shown in Fig. 4.1. Clearly, the energy minimization strategy results in a Pulse and Glide (PnG) sort of profile discussed before. An initial high acceleration is followed by a low rate of deceleration cruising. However, while the total energy demand of the tractive energy minimization case reduces by 5.6% over the velocity smoothing case, it results in a decrease of only 2.1% in fuel consumption.

For the section of the LA92 drive cycle shown in Fig. 4.1, the engine operating regions are plotted in Fig. 4.3. The engine BSFC map is divided into 5 regions of operation for analysis. The velocity smoothing case, due to lower rates of acceleration operates more in region 2 where it consumes 9.8% more energy, and a corresponding 10.7% more fuel than the tractive energy minimization case. The higher rates of acceleration for tractive energy minimization with higher initial power demand

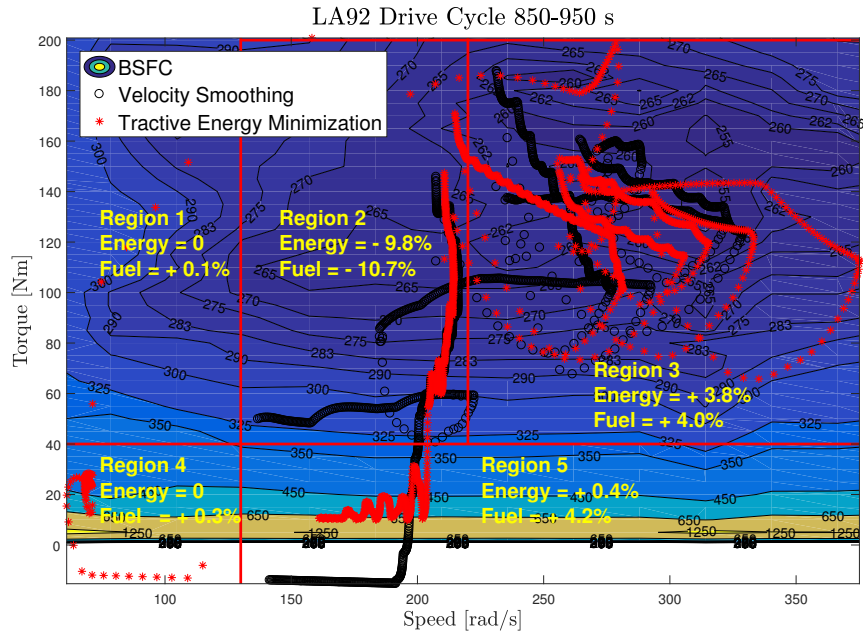


Figure 1.4: The engine operation points of the selected portion of the LA92 drive cycle is plotted on the BSFC map. The solid red lines indicate the operating regions demarcated for residence analysis. A positive number indicates a gain in power optimization over acceleration optimization

forces the operating region into region 3 where it consumes 3.8% more energy and therefore 4% more fuel than the velocity smoothing case. The problem occurs during the cruising phase, where the acceleration optimized velocity undergoes moderate deceleration but the power optimization case undergoes very low rate of deceleration. Here, the rate of deceleration is lower than the deceleration induced by drag forces and hence it requires minuscule engine power. This operation at high speeds and low torque is extremely inefficient and is found in region 5 where the power optimization case consumes 4.2% more fuel for only a 0.4% extra energy. This behavior causes the overall fuel consumption to increase even though the total energy demand is less in the power optimization case.

The insight is counter intuitive and should be considered when power is taken as a surrogate for fuel consumption. The non-linearity of the engine fuel map, coupled with the forced operation at the low torque high speed regions significantly reduces any gains found through a reduction in propulsion energy. This behavior is found spanning different engine sizes including a further downsized as well as a much larger 4.3L engine. In the downsized engine for the power optimization case, the fuel consumption was lower in some cases due to a lower torque range which forced the

engine speed to increase and operate in more efficient regions. For the larger engine, a more aggressive deceleration fuel cut-off strategy further compounded the losses, switching this strategy off still showed similar behavior.

More intuitive results were found in the electric vehicle simulations. As compared to a conventional engine the electric motor has a much flatter efficiency curve and the absence of gears allows for more efficient operation even at the low rates of deceleration. As an illustration, for the US06 drive cycle from 490 – 560s while the conventional vehicle showed a 1% increase in fuel consumption for an 18% reduction in power, the electric vehicle produced a 17% drop in battery energy consumed for a 16% reduction in power. Additionally, in the power optimization case, it was seen that battery energy recovered through regenerative braking was not proportional to the reduction in braking energy. This behavior can be attributed to the more aggressive braking in the power optimization case as compared to the acceleration optimization case. This work has been accepted and is awaiting publication in the special issue on Unmanned Mobile Systems (UMS) of the ASME Journal of Dynamic Systems, Measurement and Control (JDSMC).

1.6 Fuel Minimization

With the insights gained from the previous section, we need to accurately predict the engine torque and engine speed so that the fueling rate can be directly interpreted from the fuel map. It is especially important to determine the engine speed accurately by correctly predicting the selected gear. To this end a simplified vehicle model was built to perform DP optimization to minimize fuel consumption. Since some of the power produced by the engine is lost during transmission to the wheels these losses have to be modeled also. From a preliminary analysis, the engine fueling rate was found to be linearly proportional to the wheel power for a selected gear. This is shown in Fig. 1.5. Obviously this is an approximation and the model is being improved by further study of losses in the torque converter and the gear box.

Apart from predicting engine power, the engine speed had to also be predicted for finding the fueling rate. To characterize the engine speed accurately, the selected gear has to be either estimated or entered externally. A gear shift map based on engine torque and vehicle speed with hysteresis was developed for estimating gear selection. This map showed good co-relation with the ALPHA gear selection for the

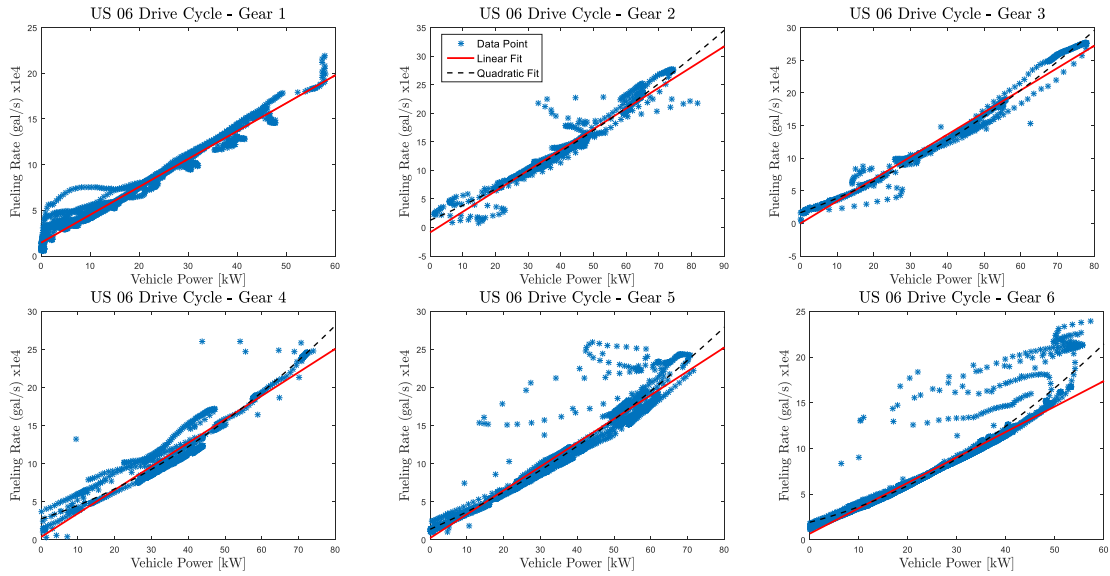


Figure 1.5: The fueling rate is shown to be an approximate linear function of the vehicle power for a selected gear ratio

LA92 drive cycle which undergoes several gear shifts. From the comparison of results generated by DP to those generated through ALPHA simulations, an estimation of gear shift based on engine torque and vehicle speed was found to be more accurate and hence the selected gear was added as another state. In the model, the vehicle speed and torque would determine the selected gear which would govern the fuel consumption. The DP optimization would from that point select vehicle speeds that would minimize the total fuel consumption. Additionally, engine idling and deceleration fuel cut-off were added to the model to improve prediction of fueling rate.

With the above simplified vehicle model, the DP optimization was carried out on the last 110s of the US06 drive cycle. An additional state of gear and long computational times to determine gear shifts slowed down the algorithm significantly and therefore only short parts of a drive cycle could be analyzed. The drive cycle generated by DP optimization was simulated using ALPHA. A 10% error was shown in the MPG predicted by DP as compared to the ALPHA results. There is scope for improvement in the vehicle model as mentioned before, especially in the torque converter losses, to improve prediction accuracy of fueling rate. Clearly this simplified model which takes into account gear switches, is not capable of modeling

the powertrain dynamics well enough, for accurate determination of engine fueling rate and therefore may lead to sub-optimal results. Hence, a more comprehensive powertrain model was sought that could account for the losses and dynamics in the powertrain as the engine torque and speed are transmitted to the wheels.

In a conventional vehicle with only a gasoline engine, the powertrain is very complex as it includes the final drive, the gearbox and the torque converter clutch. Constant efficiency losses can be modeled for the final drive and the gear box, but there are significant dynamics involved with the torque converter clutch when it is disengaged at lower gears and the impeller and turbine are not locked. The slipping between the impeller and turbine significantly affects the engine speed and can thus lead to very different fueling rates. Since modeling the conventional drive train is very hard, first a simplified model of the electric drive train was constructed. The problem however with a more comprehensive model is that it has several states which makes the problem intractable in DP.

1.7 Electric Powertrain Modeling

An analysis of optimized velocities was also carried out for electric vehicles that showed a 9.5% reduction in battery energy consumption while driving the optimized cycle as compared to the standard drive cycle. The gains found in the electric vehicle through reduced energy consumption were somewhat offset by a corresponding decrease in battery recharging through regenerative braking. However, in all the drive cycles the gains from more optimized accelerations outweighed the losses in limited battery recharging which in any case are limited by motor and powertrain efficiency. Further discussion on battery recharging for electric vehicles occurs later in this work. In effect, the optimized drive traces showed a reduction in battery energy demand to cover the same distance thus leading to an increased range. It is understood that range anxiety is the leading cause of concern for electric vehicles as limited battery capacity restricts EV range significantly. Moreover, slow charging times compound the problem further, and increasing energy storage by enhancing battery size becomes expensive. Considering all these issues, the analysis in this work shows that by adopting a smoother driving cycle, the electric vehicle is able to increase its range by 14.8% from 2.7 miles/kWh to 3.1 miles/kWh. This shows that the benefits of trace smoothing are significant for electric vehicles as well.

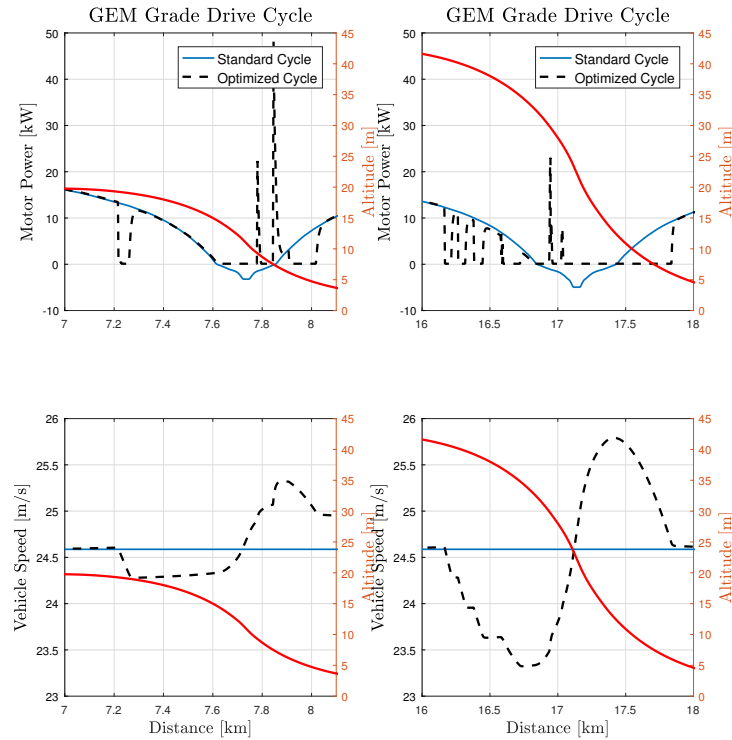


Figure 1.6: For two downhill sections of the GEM drive cycle, the optimal trajectory is to switch off motor and cruise during downhill descent. The optimal strategy is not to brake and utilize the regenerative braking capabilities.

For this work a backward model of the electric powertrain was built, which is suitable for use in numerical optimization algorithms. The model assumes a point mass vehicle and considers only longitudinal dynamics, which is appropriate for the 1-D drive cycles under consideration in this work. The input to the model is the vehicle velocity and the electric motor power demand the output. As an electric powertrain does not have variable gear ratios or a torque converter clutch, modeling the drive train is comparatively simple. The final drive gear ratio and average final drive efficiency were found from the ALPHA model of the Tesla S. This thesis also used the same experimentally determined motor map as the ALPHA model to find the motor efficiency for a given motor torque and speed. For any given velocity trajectory, the results of electric powertrain model matched perfectly with ALPHA predictions thus giving high confidence in the validity of the electric vehicle model.

Using this model, offline DP optimization was carried out to minimize electric power demand at the motor. The constraints were similar to those applied previously in following the hypothetical lead. Somewhat surprisingly, the results were similar to those of wheel power minimization. The results are surprising because with the

electric powertrain now allowed for regenerative braking where negative motor power should reduce the cost function. However, the optimal solution does not seem to exploit this feature.

To further investigate this phenomenon, road grades were introduced in the analysis. Under the EPA's GEM program there exists a constant velocity grade changing drive cycle that allowed us to find the optimal velocity profile as the electric vehicle navigated the hill ascents and descents. In following the constant speed lead of 55 MPH, the optimal trajectory seemed to adhere to the well know principles of hill climbing from [56], where, the optimal policy is to "increase speed while approaching the base of the hill, and then allow the speed to drop off while climbing the hill ... and reverse while descending." This optimal policy does not utilize the regenerative braking capabilities to recharge the battery in hill descent.

From the literature review, it seems that for vehicles that have a regenerative capability, hill descent was always seen as an opportunity to recharge their battery. Clearly this is not the optimal solution. It has been shown in our analysis that the only time when the vehicle braked to utilize regenerative capabilities was when either the position constraints had to be satisfied so vehicle velocity had to be reduced to meet them, or the velocity constraints had to be satisfied, where the vehicle velocity would increase beyond its limits. These cases were explored and explained in detail in our CCTA 2018 submission [57].

The reason for not utilizing the regenerative capabilities is simply the efficiency losses in converting mechanical power at the brakes to electrical power at the motor. Even with a very high conversion efficiency of 90%, the round trip efficiency in converting brake power back to propulsion power at the wheels would be 81%. It was shown that if there were no efficiency losses, then the optimal policy did utilize regenerative braking thus confirming our hypothesis.

1.8 Fuel Cell Hybrids

The last part of this thesis looks at the modeling and simulation of Fuel Cell (FC) hybrid vehicles. From the work done so far in this thesis, the constrained velocity trajectory optimization considers the powertrain dynamics of a conventional gasoline vehicle as well as a battery electric vehicle. However, an optimization problem with two power sources has not yet been considered, where the desired electric power

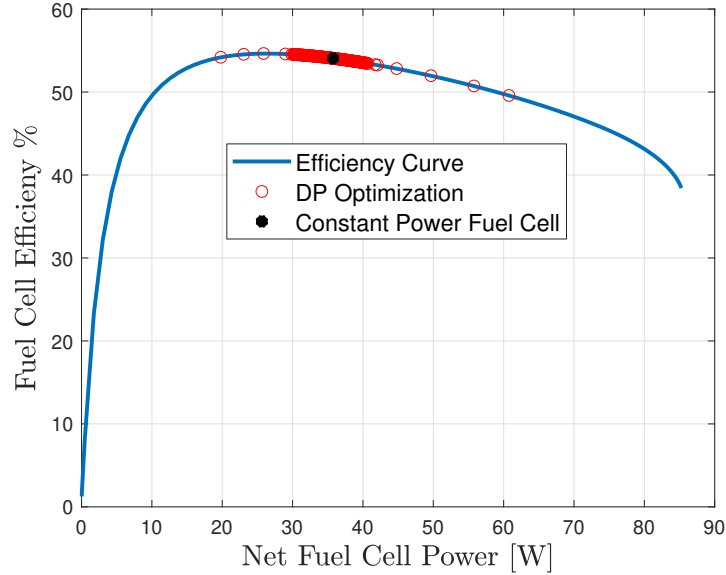


Figure 1.7: Optimal Fuel Cell operating points for a given velocity trajectory, for the global optimal DP solution and constant power rule based. The difference in hydrogen consumption between the two is only 0.07%

demand of the motor can be met with either a fuel cell or a battery or indeed with a combination of both. The optimization challenge here is different as the battery's capacity is limited and optimal operating points of the fuel cell are sought. Moreover, the FC polarization curve is affected by the FC temperature. The temperature can be controlled by regulating the cooler fan speed, which parasitically draws some electric power to operate. For higher power density FC stacks, a liquid cooled system is required due to significantly higher heat generation. Additionally, the compressor at the cathode input also draws some electric power but affects the FC polarization curve. From this description it is clear that such optimization involves several states and efficiency can be affected by several factors and parasitic losses.

As part of the initial analysis done in this thesis for a constant temperature FC efficiency, it was found from DP optimization that the optimal policy is to discharge the battery down to its minimum level, but operate the fuel cell at an almost constant power as shown in Fig 1.7. Using this conclusion a simple rule-based strategy of constant power FC operation showed only a 0.07% difference from the global optimal solution. The value of the constant power provided by the FC was dependent on the energy stored in the battery. The reason for this constant power operation was simply that the FC efficiency decreased almost linearly with increasing power drawn and hence the optimal policy was to draw as little power as possible. The only

time this strategy did not work, was when the constant power demand was less than the peak efficiency point as shown in Fig 1.7. In this case, the global optimal solution was to switch between FC off and its peak efficiency point. The inclusion of thermal effects by adding an air cooling system and the state of temperature, to dynamically compute the FC efficiency, resulted in similar optimization. Now, the FC operated at a higher power initially to quickly raise the temperature and then descended to a constant power operation. During this period, the cooling fan also operated at a constant power. Towards the end, the cooling fan switched off and let the temperature of the FC rise slightly. These results were presented at SAE 2018 [58].

1.9 Thesis Organization

This thesis is organized as follows. Chapter II presents the concept of the Hypothetical Lead vehicle, which serves as the baseline lead velocity trajectory for the rest of this thesis. In Chapter III the optimization results from velocity smoothing are shown. It also includes a full preview optimization using Dynamic Programming and short accurate as well as inaccurate previews using Model Predictive Control. Chapter IV presents the results from velocity optimization using more detailed and vehicle specific models, with the conclusion that velocity smoothing can perform as well if not better than more complex optimizations. The analysis for the electric vehicle is presented in Chapter V, including velocity smoothing as well as velocity optimization over varying road grades. Finally Chapter VI presents the optimization results for minimizing fuel consumption in a Fuel Cell hybrid. Chapter VII is a short note on the future work required to answer some of the open questions from the conclusions of this thesis.

1.10 Contributions

It has been shown through the literature survey that a consistent fuel economy measuring framework does not exist for autonomous vehicles. It's been also shown that while the main motivation driving autonomous vehicle development is safety and driver comfort, to achieve significant reduction in CO_2 emissions regulators will need to compel autonomous drive cycles to be more efficient.

1. **Hypothetical Lead:** The first contribution of this work is to develop the con-

cept of a Hypothetical Lead (HL). The HL provides a consistent framework for regulators to assess the benefits of an algorithm-driven drive cycle over human driving. It's been shown that the HL can be derived from any of the present EPA drive cycles, or even from any other drive cycle. Hence the HL allows for comparison of well known human driving to any algorithm and understand their impact. As stated before, this result motivates regulatory policy as well. This work was presented at ACC 2016 [49].

2. **Velocity Smoothing (Offline):** Following on from the above work, the second contribution is to take the constraints of the HL and optimize within them to “smooth” the velocity trace by minimizing accelerations and decelerations. This simple optimization, done offline using Dynamic Programming (DP), shows up to an 18% increase in fuel economy. These results have been validated with dynamometer experiments, at the EPA’s testing facility. The FE improvements in experiments are even better than in simulation and showed significant reduction of up to 20% for CO_2 . Additionally, emissions are also reduced for the smoothed velocity by 75% for NO_x and 60% for CO . These results are presently under preparation for submission.
3. **Velocity Smoothing (Online):** For online velocity smoothing, Model Predictive Control (MPC) has been employed and shows up to 12% improvement with just 1.5 s of accurate preview. The methods and results were presented at DSCC 2016 [53]. In a previous velocity prediction algorithm that provided inaccurate prediction, a 10% improvement has also been shown. Additionally, from these results, it's been concluded that within the present formulation, prediction accuracy in only the first few seconds is important for optimization. These results are under preparation for submission.
4. **Optimal Fuel Cost Function Evaluation:** For the fourth contribution, this work has tried to minimize the energy demand at the wheels while adhering to the constraints of the HL. Interestingly, even with a significant reduction in energy demand over the previously smoothed velocity trace, there are some drive cycles where the fuel consumption actually increases. The issue with energy optimization is that it always results in a pulse and glide velocity trajectory [54], where the glide portion of the trajectory has a minuscule energy demand. However, due to the non-linear engine efficiency map and powertrain, the fuel

required to traverse the glide portion is disproportionately high. Thus depending on the length of the glide, the overall fuel consumption can be higher as compared to the smoothed velocity trace. Hence, use of velocity smoothing from the previous work might work just as well, if not better than tractive energy minimization. These results have been found to be valid in simulation for a further downsized as well as full size naturally aspirated 4.3L Ecotec engine. This is an important conclusion as trace smoothing is desirable for passenger comfort but the pulse and glide trajectory has a lower energy demand at the wheels. This work shows that perhaps there is no trade-off between passenger comfort and fuel consumption. Therefore a simple linear model that does not require vehicle specific information, and is easily solvable with quadratic solvers, while also being more conducive for passenger comfort can be used for optimal fuel solutions. This work has been accepted for publication in the special issue on Unmanned Mobile Systems (UMS) of the ASME Journal of Dynamic Systems, Measurement and Control (JDSMC).

5. **Gasoline Vehicle Velocity Optimization:** Continuing from the previous work, when a more complex vehicle model to directly compute fueling rate is introduced in the optimization it is found that the resulting FE is lower than the previous two optimizations. This arises due to inaccuracy in the vehicle model. Moreover, for a 120 s optimization, DP requires over 2 hours to complete. When a more complex model is employed that shows only a 0.7% error in fuel consumption from ALPHA, the increased number of states thus render DP intractable. Hence for future work, a better optimization methodology has to be used to deal with these additional states.
6. **Electric Powertrain Velocity Optimization:** Based on the previous results it is clear that for fuel minimization, the entire powertrain dynamic model should be included in the optimization algorithm. The problem is that, electric vehicles have regenerative braking capabilities and it's been found that the optimal cycle does not include regenerative braking. This is true even for traversing road grades, where downhill slopes offered an opportunity to brake and recharge the battery, but the optimal policy is to avoid braking and increase speed with the gravitational pull. This results in efficiency losses in battery recharging, so that even a 90% motor efficiency was in effect 81% efficient round-trip. Hence the

sixth contribution of this thesis is to show that different technologies may not be harmonious and complementary. This is important for high level analyses where improvements from different technologies are algebraically added but our results show this not to be true. These results have been presented at CCTA 2018 [57].

7. **Fuel Cell Hybrid Velocity Optimization:** The final contribution of this thesis is in the realm of Fuel Cell (FC) hybrids. This work shows, that fuel cell efficiency is the main determining force in the optimal power split. For all drive cycles studied, FC operates at a constant power while the battery is discharged and charged in navigating the power variations. This allows for a simple rule based solution that matches the global optimal results. Even in charge sustaining mode, the optimal FC operation is either at it's maximum efficiency point or at zero power. Further it's been shown that introduction of thermal constraints on the FC do not change the constant power operation. However, FC temperature constraints are important contributors to stack sizing and battery thermal constraints to it's discharge rate. Some of the initial results were presented in [58], another paper is in preparation to present additional results.

CHAPTER II

Hypothetical Lead Vehicle Trace

The regulation of fuel consumption and emissions around the world is based on standard drive (SD) cycles. Several autonomous or simple eco-driving methods of smoother driving and smaller acceleration and braking can violate the ± 2 MPH speed deviation regulation from the SD and hence they are currently not counted towards the vehicle fuel economy, even though they are acceptable from a traffic pattern perspective, namely following a vehicle at a safe and reasonable gap. This chapter develops and suggests a prototypical vehicle velocity versus time trajectory that supersedes each SD cycle since the SD cycle is the vehicle trace from following a vehicle with the prototypical velocity trace. The prototypical velocity trace is named from now on as the Hypothetical Lead (HL) vehicle cycle. In essence, the **HL cycle recreates the traffic conditions followed by the drivers of the standard drive cycles.** In the following chapters we demonstrate the use of this HL cycle for assessing the fuel economy benefits of autonomous following in relation to standard test cycles and limits on the following distances to ensure that the different drive traces follow the same prototypical traffic conditions in a reasonable and safe way for real world applications. Thus ensuring that all reported Fuel Economy improvements in this thesis are over a human navigating those traffic conditions.

2.1 Introduction

Autonomous vehicles have been the focus of researchers for several decades and there are several ideas in the literature regarding technologies that can be utilized to implement automated driving. While a lot of research has been focused on the safety aspects of autonomous driving with technologies to prevent collisions, lane departure or blind spot crashes, autonomous technologies also can be used for decreasing fuel

consumption of vehicles. Implementation of advanced vehicle following strategies to optimize engine performance and fuel economy for autonomous vehicles could change the way a light-duty autonomous vehicle negotiates traffic as compared to a human negotiating the same traffic conditions. Unfortunately, the current certification of vehicle fuel efficiency cannot account for such efficiency benefits so there is a lot of interest in devising a methodology that will quantify the benefits with minimum deviation from the existing rules [59].

Presently the US Environmental Protection Agency (EPA) and other regulatory agencies around the world use pre-specified velocity versus time traces called standard drive (SD) cycles to approximate how a driver navigates through different road types and traffic conditions as shown schematically in the upper section of Fig. 1. Only a ± 2 miles per hour (MPH) deviation is allowed by the EPA from the standard velocity trace for a valid test (Code of Federal Regulations, title 10, sec 86.115). Despite their limitations in capturing every possible driving style or traffic, the standard drive cycles are good approximations of a set of everyday driving conditions and are used to compare the fuel consumption of various vehicles.

Given the importance of the SD cycles in the regulatory framework, many autonomous longitudinal driving studies concentrate on intelligent following of a lead vehicle that traces the SD cycles [60]. This would in theory increase the fuel efficiency of the vehicle but it has been also shown that it can cause higher fuel consumption under following conditions with very small deviation from the SD cycles. Hence, the current trend of evaluating fuel consumption reduction in autonomous driving by following a SD is re-examined and a new methodology is proposed. This chapter suggests a new procedure to objectively compare a human driver to an autonomous vehicle and quantify the fuel economy benefits of using autonomous driving technologies.

Vehicle following using eco-driving strategies are being encouraged amongst drivers across the world, to help them improve fuel economy while driving in their daily lives. These tips include maintaining an even driving pace, accelerating moderately from 2000 to 2500 RPM and anticipating traffic flow to avoid sudden starts and stops. A conservative estimate of eco-driving benefits calculates a reduction of 33 million metric tons of CO₂ annually from being emitted into the atmosphere [31]. It is reasonable to assume that vehicles with autonomous technologies would implement

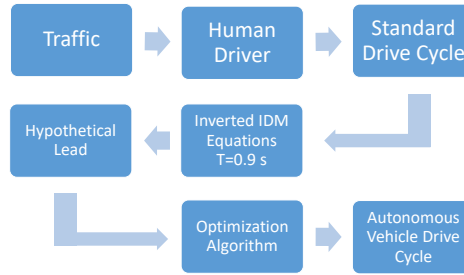


Figure 2.1: Schematic describes the development of the hypothetical lead (HL) vehicle and the sections of the paper with an example of the HL trace used to evaluate the fuel consumption of a particular following strategy.

such driving strategies to reduce fuel consumption and emissions.

As stated in the introduction, previous works have achieved 0.5% – 10% reduction in CO_2 , through Adaptive Cruise Control (ACC) acting between speeds of 18mph and 100 mph in velocity profiles based on expert-rules derived by observing real-world pilots [22]. While, [36] used an optimization algorithm that computed the appropriate acceleration based on traffic conditions so as to improve fuel economy. They were able to show a 8.8% reduction in fuel consumption. In [34] an optimization algorithm was developed to reduce deviations in velocity and thus accelerations by having a velocity preview. Fuel consumption reductions of up to 33% in a vehicle powered by a standard SI engine was shown in simulations over the UDSS drive cycle. However, in changing the SD the distance between the optimized cycle and SD was very large, exceeding 300 m in some cases and overshooting the SD in some cases as well. To avoid distances that are so large that other vehicles could cut-in or too short to be safe rendering real-world implementation impractical one has to impose constraints in the following scenario.

Unfortunately, there is a trade-off between the following distance and the fuel consumed as shown in Table 2.1. The table shows the cases where vehicles were trailing a vehicle executing the UDSS drive trace for different time headways. A car length is assumed to be 4.5 m, a common safety limit is 1 car length per 10 MPH [50]. This entire simulation will be discussed in detail later, but it is worth noting that the fuel consumption only matched for the vehicle following case with a Time Headway of 1.7s. However, the FE increased for larger headway, creating a confusion on what should be considered as the baseline. If the SD cycle is the baseline itself, then a lead velocity trace must be determined for the automated driving vehicle to follow.

Table 2.1: Influence of time headway on fuel economy over the UDDS

Time Headway	FE Change (%)	Car Length/ 10 MPH
0.9	-2.5	1.00
1.25	-1.1	1.33
1.7	0	1.80
2.5	1.1	2.67
3.9	3.9	4.00

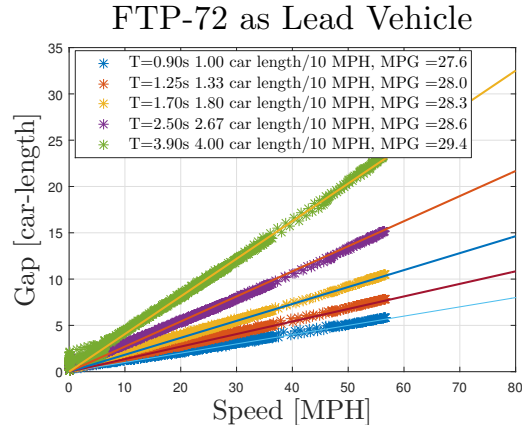


Figure 2.2: Comparison of fuel economy results predicted through the ALPHA model for 2013 Ford Escape with a 1.6L Ecoboost engine. Parameter T is the time headway that a follower vehicle maintains from the lead vehicle. Smaller headway indicates more aggressive following. Aggressiveness in following distances significantly changes the fuel consumption. Standard FTP gives 28.3MPG on the chosen vehicle that is 4.5 m long.

Further, the table clearly shows that increased fuel economy is not an inevitable consequence of automated driving, hence regulators would want to encourage driving algorithms that improve FE. The results of the table are visually displayed in Fig. 2.2, where increasing gap results in an increased FE. The baseline FE of the FTP 72 is 28.3 MPG.

This chapter develops a hypothetical lead (HL) velocity trace from the standard drive cycles to simulate the lead traffic conditions that can be followed by automated driving algorithms to compare the differences between human and automated following. Beyond the EPA testing procedures, this method can also be used to simulate various autonomous technologies and optimization algorithms and evaluate the benefits of using one over the other. Fig. 2.1 provides an overview of the paper and the rationale for the analysis. Section 2.2 reviews the development of the standard drive cycles. Section 2.3 analyzes vehicle following models while Section 2.4 describes the development of the hypothetical lead vehicle from the inverted equations of a vehicle following model.

2.2 Background on Current EPA Fuel Economy Test Procedures

Current certification tests for fuel economy as carried out by the U.S. Environmental Protection Agency involve running all vehicles through standard drive cycles on a chassis dynamometer (Code of Federal Regulations, title 10, sec 86.115). The first drive cycle, the Federal Test Procedure (FTP), also called the Urban Dynamometer Driving Schedule (UDDS), was developed by authorities in Los Angeles (LA) in 1971 trying to reduce smog in their city. They concluded that the morning drive to work was the biggest contributor to the city’s smog and they wanted a test procedure so that the vehicle emissions could be quantified and regulated. The authorities approximated the morning drive to work of an average LA driver by specifying a route shown in Fig. 2.3, which combined different road speeds and traffic conditions.

Six drivers drove the trace, in the same car, with five producing remarkably similar results. The actual trace closest to the mean of all traces was taken with minor modifications to its length as the standard drive cycle [47]. The rationale was to find a vehicle velocity trace that a driver executes while navigating through traffic. It was assumed that to navigate through the given traffic scenario, the UDDS velocity profile would have to be adopted for all vehicles and individual vehicle capabilities would not change the velocity profile if driven by an average human. Similar methods were used to develop other drive cycles such as Highway Fuel Economy Test (HWFET) where drivers were instructed to follow traffic, i.e. pass as many vehicles as passed them [61]. It must be kept in mind that human drivers generated all velocity traces that were finally set as standard drive cycles.

2.3 Vehicle Following Model Implementation

In traffic simulation research, several car following models have been developed to predict the speed of the trailing vehicle in the single lane case. Lefèvre et al [44] compared various parametric approaches that differently predicted the speed of vehicle in a vehicle following mode for a given traffic condition. Of all the parametric approaches, the mean average error and the root mean squared error was found to be the least for the Intelligent Driver Model (IDM). Hence, the IDM was selected as the vehicle following model for this paper. It uses a combination of safe time headway and comfortable braking distance to compute the desired distance from the

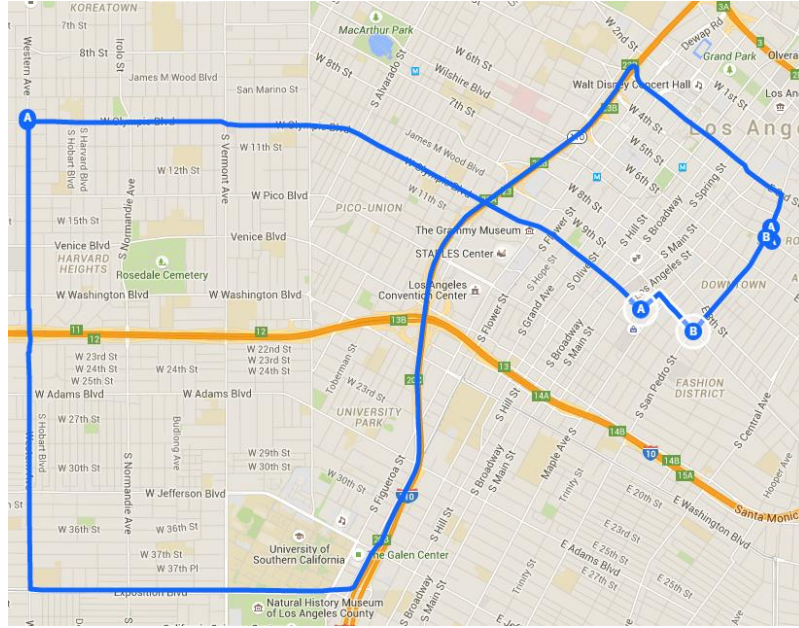


Figure 2.3: Route selected as the typical morning drive to work in Los Angeles in 1971.

lead vehicle and then the actual distance and speed to find the acceleration.

The model used in this thesis to evaluate fuel consumption over a drive-cycle is the Advanced Light-Duty Powertrain and Hybrid Analysis Tool (ALPHA) model developed at the US Environmental Protection Agency [3]. Any drive cycle in 1 Hz resolution can be loaded into the program and the tool incorporates a driver model that is able to track the velocity. The vehicle used is a 2013 Ford Escape with a 1.6L EcoBoost engine [62].

While IDM does show the smallest error with actual traffic data compared to other parametric approaches, there are still some driving characteristics of humans that cannot be captured by the model. Humans change their driving pattern depending on the traffic conditions. In our case, it is assumed that each standard driving trace is created for a certain traffic pattern and hence changing the parameters for each trace would capture this effect. Humans have other signals apart from the speed of the front vehicle such as brake lights and perception of lead driver's intentions which allow them to react early. Additionally they have a perception threshold and only significant changes in speed are determined by the follower vehicle delaying their reaction. Early perception would cause the following driver to act before the IDM would predict and the perception threshold would cause the driver to act after the IDM predicts a response. From the experimental work done by

Lefèvre it can assumed that IDM misses the overshoots and undershoots but is a reasonable approximation of what the driver would do. The RMS error was shown to be about 0.25 m/s for a 1 s prediction horizon. In actual dynamometer testing, for the UDDS an RMS error of 0.2 m/s was seen between the ALPHA model velocity and the actual velocity trace driven by an experienced driver. This indicates an acceptable error margin being given by the IDM equations.

The aforementioned IDM, described below was used to follow a vehicle executing a drive cycle.

$$(2.1) \quad d_{actual,k} = s_{L,k} - s_{F,k}$$

$$(2.2) \quad r_k = v_{L,k} - v_{F,k}$$

$$(2.3) \quad d_{des,k} = d_{min} + T \times v_{F,k} - \frac{v_{F,k} \times r_k}{2 \times \sqrt{a_{max} \times b_{comf}}}$$

$$(2.4) \quad a_{F,k+1} = a_{max} \left(1 - \left(\frac{v_{F,k}}{v_{max}} \right)^4 - \left(\frac{d_{des,k}}{d_{actual,k}} \right)^2 \right)$$

$$(2.5) \quad b_{max} \leq a_{F,k+1} \leq a_{max}$$

Table 2.2: Parameter Definitions

Parameter Name	Parameter Definition	UDDS
d_{des}	Desired Gap (m)	<i>Calculated</i>
d_{min}	Minimum Gap at 0 velocity (m)	2
T	Time Headway (s)	0.9
v_L	Lead vehicle speed (m/s)	<i>Calculated</i>
v_F	Follower vehicle speed (m/s)	<i>Calculated</i>
v_{max}	Maximum vehicle speed (m/s)	45
r	Relative speed of lead and follower vehicle (m/s)	<i>Calculated</i>
a_{max}	Maximum acceleration (m/s^2)	3.0
b_{comf}	Comfortable deceleration (m/s^2)	1.5
a_F	Acceleration of follower vehicle (m/s^2)	<i>Calculated</i>
b_{max}	Maximum deceleration (m/s^2)	3.0

Where the subscript L denotes the lead and F the follower. Parameter d is the gap, s the displacement, v the velocity, a the acceleration, b the braking and r is the

relative velocity. The value of each parameter (T , a_{max} , b_{comf} and d_{min}) depends on the velocity time trace of different drive cycles. Each standard drive cycle is said to represent a particular type of road with the expected traffic conditions and hence the speed, acceleration and braking.

To generate Fig 2.2, the standard drive cycle, in this case UDDS, is the lead vehicle. The UDDS involves maximum acceleration and deceleration of 1.5 ms^{-2} and -1.5 ms^{-2} respectively. Since drivers don't tend to push the car to the limit the maximum acceleration (a_{max}) was chosen to be double the maximum acceleration seen in the drive cycle. The comfortable braking (b_{comf}) was kept the same as the maximum braking of standard drive cycles and the maximum braking in IDM, double of that. The minimum distance was kept at 2m. An important assumption of the selected model is that the reaction time and attention span of the driver are merged to 1s and used as the time step for the iterations. Prior work [42] shows that this is reasonable. The parameters values for the UDDS case are given in Table 2.2.

The time headway (T) can be varied to find the optimal gap that should be maintained from the vehicle in front. The gap can be increased or decreased by appropriately tuning T . The eco-driving strategies are implemented while keeping in mind that the gap between the lead vehicle and the follower vehicle has to be long enough to ensure a safe braking distance but at the same time not too long such that other vehicles can cut in and cause the autonomous vehicle to brake thus negating the objective of maintaining an even driving pace.

A time headway of 0.9s for the FTP drive cycle would achieve the desired gap between the lead and the follower vehicle such that it is safe, does not allow cut-ins and is good for traffic flow. However, the given velocity trace violated the ± 2 MPH for less than 2s regulation on 15 occasions and still showed a worse fuel economy than the UDDS drive cycle as shown in Fig 2.2. Close following made the follower vehicle speed vary significantly as it tried to keep up with the lead vehicle and maintain a safe distance. The RMS error between the standard drive cycle and the following velocity trace was 0.4 ms^{-1} . Increasing the time headway to 1.7s produced a velocity trace that matched closely with the standard cycle, did not violate the regulations, showed an RMS error of 0.2 ms^{-1} and a fuel consumption that matched the UDDS. However, in this case the following distances were larger (1.8 car-lengths), and would allow cut-ins. Increasing the time headway further reduced fuel consumption and for

$T = 3.9$ s a 4% increase in MPG could be seen however, the following distances were very large and the RMS error was 1.2 ms^{-1} .

For the case where vehicles are made to follow the UDDS drive cycle, it was shown that for $T = 0.9$ s, fuel consumption was more than the lead UDDS. Conversely for larger following distances lower fuel consumption is observed. An autonomously driven vehicle should be able to negotiate this trade off and achieve an optimal fuel economy. Through this example we have seen that in an attempt to decrease fuel consumption the regulations for speed are violated. Hence we need to determine another methodology that can evaluate the reduction in fuel consumption by use of self-driving algorithms that deviate in navigation through traffic from humans.

2.4 Hypothetical Lead Vehicle Profile

A systematic evaluation technique has to be developed that can objectively determine the fuel economy benefits of self-driven cars. To do this we could turn back to the rationale of the original standard drive cycles. These cycles were developed as an approximation of how an average human driver would navigate through different road and traffic conditions. The same thinking can also be used for evaluating autonomous driving capabilities. Since the standard drive cycles were humans navigating through traffic conditions, to find autonomous driving benefits we should compare it to how a controller based off an optimization algorithm would navigate through the same traffic conditions.

To recreate the traffic conditions for the standard drive cycles, this chapter inverted the IDM equations. By inverting the equations the velocity trace of the lead vehicle being followed by the driver driving the standard drive cycles could be found. It is important to note that the driver of the standard drive trace would not just be following a single vehicle in a single lane but rather reacting to lane changes, stop lights, stop signs etc. The standard drive cycles are a simplified trace and the recreated traffic conditions are simplified single lane hypothetical lead vehicle velocity traces. Hence, the lead vehicle is essentially a hypothetical velocity trace that drivers of the standard drive traces followed to produce their respective drive cycles.

Since we are trying to determine the velocity profile of the lead vehicle from the follower vehicle data. The follower speed v_F and acceleration a_F are already known. Considering a single time step of 1 s, we can write the velocities of the lead and

follower vehicles as

$$(2.6) \quad v_{L,k} = s_{L,k} - s_{L,k-1}$$

$$(2.7) \quad v_{F,k} = s_{F,k} - s_{F,k-1}$$

Using the above equations, with equation 2.2, equation 2.1 the actual gap between the lead and follower can be defined by equation 2.8, where $s_{L,k-1}$ and $s_{F,k-1}$ are known but r_k is unknown.

$$(2.8) \quad d_{actual,k} = s_{L,k-1} - s_{F,k-1} + r_k$$

Then by rearranging equation 2.4 we get equation 2.9, where $d_{des,k}$ and $d_{actual,k}$ are unknown. Since the vehicles do not crash the desired and actual distance between the vehicles is always positive.

$$(2.9) \quad \frac{d_{des,k}}{d_{actual,k}} = \sqrt{1 - \frac{a_{F,k+1}}{a_{max}} - \left(\frac{v_{F,k}}{v_{max}}\right)^4}$$

Finally rearranging equation 2.3 gives equation 2.10, where r_k and $d_{des,k}$ unknown.

$$(2.10) \quad r_k = (d_{min} + T \times v_{F,k} - d_{des,k}) \frac{2 \times \sqrt{a_{max} b_{comf}}}{v_{F,k}}$$

Hence there are 3 equations and 3 unknowns. Substituting equations 2.8 and 2.9 into equation 2.10 produces equation 2.11 from which the relative velocity r_k can be determined

$$(2.11) \quad r_k = \frac{d_{min} + T \times v_{F,k} - s_{L,k-1} - s_{F,k-1} \sqrt{1 - \frac{a_{F,k+1}}{a_{max}} - \left(\frac{v_{F,k+1}}{v_{max}}\right)^4}}{\frac{2\sqrt{a_{max} b_{comf}}}{v_{F,k}} + \sqrt{1 - \frac{a_{F,k+1}}{a_{max}} - \left(\frac{v_{F,k+1}}{v_{max}}\right)^4}}$$

From the relative velocity the velocity of the lead vehicle can be found from equation 2.2. The initial conditions are assumed to be $v_F(0) = v_L(0) = a_F(0) = s_L(0) = 0$ and $s_F(0) = -d_{min} = -2$.

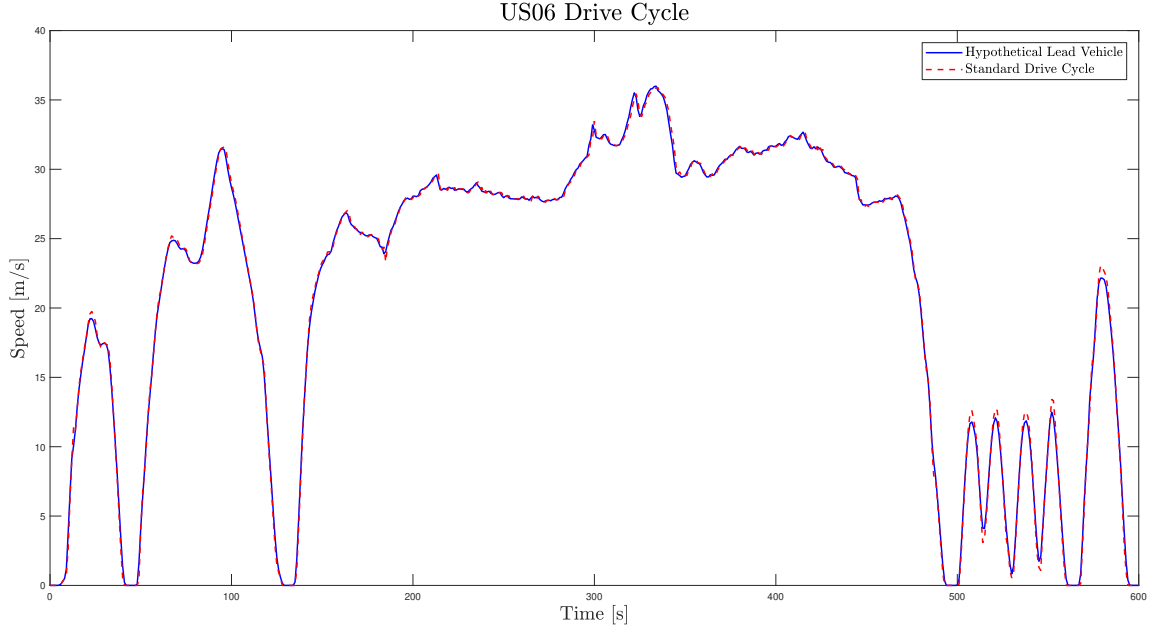


Figure 2.4: US06 Drive Cycle with the hypothetical lead vehicle trace

The equations can be applied to any naturalistic drive cycle to produce the hypothetical lead drive traces. Specifically this process was carried out for five standard drive cycles, UDDS, HWFET, LA92, US06 and SC03, to determine the traffic conditions being followed by the driver of these traces. The parameter values are given in Table 2.3. For this paper the following gap was kept at $T = 0.9$ s, which gives a 1 car-length/10 MPH inter-vehicle distance. By this logic if the hypothetical lead vehicle were to be followed by the IDM to mimic a human driver it would result in the standard drive cycle. In the next sections of this thesis we will follow this hypothetical lead with optimal control algorithms such that a consistent comparison is possible between human and automated driving.

The HL vehicle trace resulting from the US06 drive cycle is shown in Fig. 2.4. As mentioned before, 0.9 s time headway is close following hence, the actual SD cycle is more aggressive than the HL in following. A magnified plot with the first 130 s of the UDDS drive cycle is shown in Fig. 2.5, where the blue velocity trace of the HL, is followed by the red dotted trace of the SD cycle. Again, the SD cycle due to close following is more aggressive than the HL.

Table 2.3: Parameter Value

Parameter Name	UDDS	US06	LA92	SC03	HWFET
$d_{min}(m)$	2	2	2	2	2
$T(s)$	0.9	0.9	0.9	0.9	0.9
$v_{max}(m/s)$	45	45	45	45	45
$a_{max}(m/s^2)$	3.0	6.0	4.0	6.0	3.0
$b_{comf}(m/s^2)$	1.5	2.5	1.5	2.5	1.5
$b_{max}(m/s^2)$	3.0	6.0	4.0	4.0	3.0

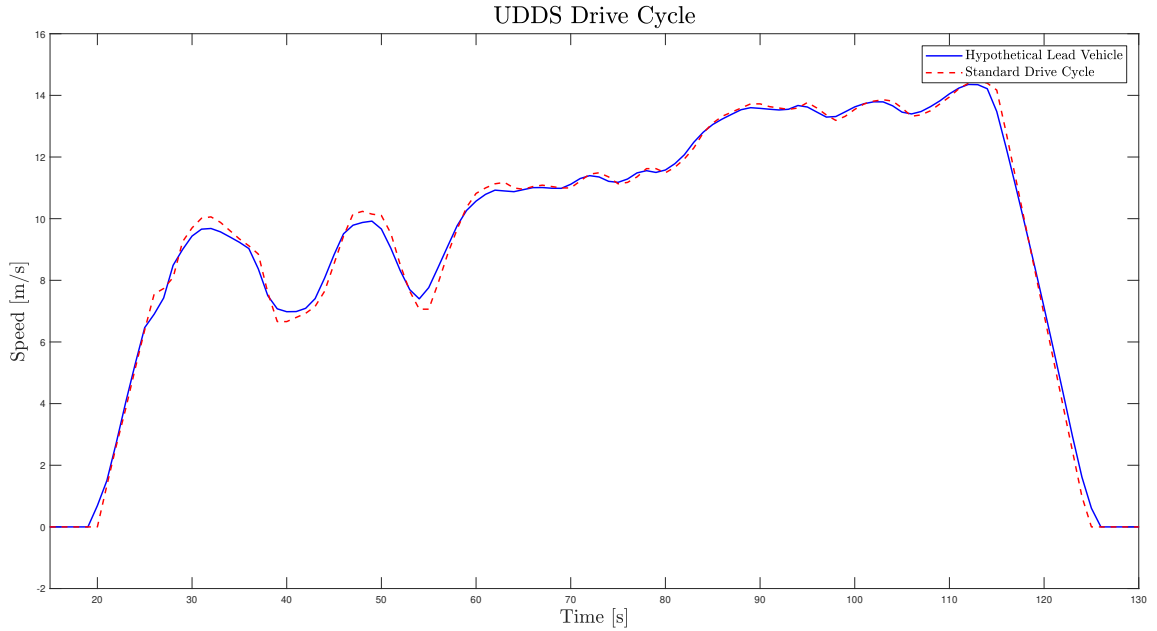


Figure 2.5: First 130s of the UDDS Drive Cycle with the hypothetical lead vehicle trace

2.5 Conclusions

The hypothetical lead vehicle provides a good baseline for comparing automated driving with the vehicle executing an SD. The rationale of the method developed in this thesis is that given the HL a human followed to produce the SD, how would an autonomous vehicle with eco-driving capabilities follow the HL. To judge the fuel consumption reduction by use of autonomous technologies the autonomous trace produced through the vehicle following algorithm can be compared to the SD trace thus giving a straightforward comparison under the same principles.

CHAPTER III

Velocity Smoothing

Constrained optimization control techniques with preview are designed in this chapter to derive optimal velocity trajectories in longitudinal vehicle following mode, while ensuring that the gap from the lead vehicle is both safe and short enough to prevent cut-ins from other lanes. The hypothetical lead vehicle associated with the Federal Test Procedures (FTP) [49] is used as an example of the achieved benefits with such controlled velocity trajectories of the following vehicle. Fuel Consumption (FC) is indirectly minimized by minimizing the accelerations and decelerations as the autonomous vehicle follows the hypothetical lead. Implementing the cost function in offline Dynamic Programming (DP) with full drive cycle preview showed up to a 17% increase in Fuel Economy (FE). These results were validated with chassis dynamometer testing, which additionally showed a significant reduction in emissions. Real time implementation with Model Predictive Control (MPC) showed improvements in FE, proportional to the prediction horizon. Specifically, 20 s preview MPC was able to match the DP results. A minimum of 1.5 s preview of the lead vehicle velocity with velocity tracking of the lead was required to obtain an increase in FE. Further, a velocity prediction algorithm was used to predict 10 s future velocity of the lead as input constraints to MPC. These predictions have inaccuracies, and based on the results we conclude that using an accurate prediction in the 1st s is most important for FE improvements under our formulation.

3.1 Introduction

Vehicle autonomy is steadily increasing and in the coming years several manufacturers would offer vehicles with the capability for highly autonomous driving. Presently, adaptive cruise control systems lack the ability to navigate through all

traffic conditions and are recommended only at highway speeds for safe operations [63]. However, autonomous vehicles at the very least would have longitudinal traffic navigation capabilities at all speeds and traffic conditions. The navigation algorithms for autonomous vehicles can be designed to improve their fuel economy (FE), as compared to the FE obtained by a human driving through the same traffic conditions.

In [34] a set of linear equations were used to reduce the accelerations and decelerations. Both showed significant improvements in FE. However, these results are obtained without imposing conditions on how far the follower vehicle could fall behind the lead, resulting in possible cut-ins that would change the velocity. Hence maintaining the appropriate gap between the vehicles is an important consideration that limits the scope for trace smoothing. The authors in [36] compared a linear quadratic and a Model Predictive Control (MPC) following algorithm, showing a fuel consumption decrease of 8.8% if a 5s look-ahead capability is guaranteed. However, the authors employed time-invariant constraints on position. These could result in an awkward traffic pattern since real-world driving varies the following gap based on the speed. Moreover, they did not use standard drive cycles and hence were unable to show how the controller would perform in known and regulated conditions. Also their baseline was not a human drive cycle but a LQR derived trajectory.

In this chapter, the Federal Test Protocols (FTP) and associated drive cycles are considered using the hypothetical lead vehicle. The concept of a hypothetical lead vehicle for any standard drive cycle was introduced in Chapter II. The idea was to find the lead vehicle velocity trajectory followed by the driver of a standard drive cycle. Autonomous vehicles could follow the same lead with various algorithms. This method would allow for simulation of actual traffic conditions associated with the Federal drive cycles and also provide a consistent comparison between how humans follow traffic and how optimal controllers would follow the same traffic conditions. Obviously any vehicle with automatic longitudinal control can employ these optimal controls.

This chapter will develop optimal control algorithms that use the preview of the hypothetical lead vehicle to chart a velocity trajectory for the autonomous vehicle. The constraints on the autonomous vehicle are imposed by the position and speed of the lead. The objective is to minimize fuel consumption of the autonomous vehicle as it navigates through different traffic conditions, represented by different drive cy-

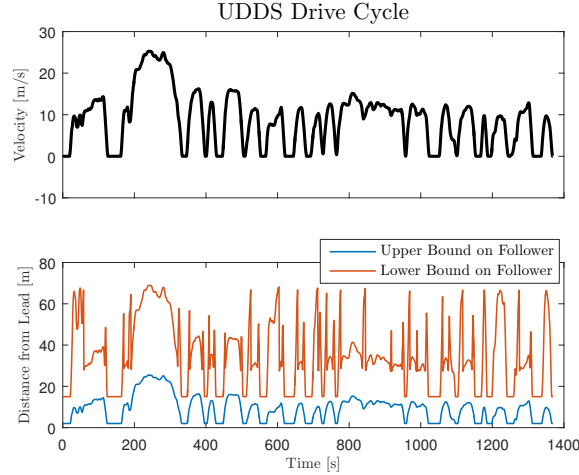


Figure 3.1: Position constraints to be applied on the following autonomous vehicle based on the position and velocity of the hypothetical lead

cles. Fuel consumption is indirectly minimized by reducing energy consumed during accelerations and energy loss in decelerations. The objective thus translates into a constrained optimization problem.

To solve this optimization problem, Dynamic Programming (DP) and MPC have been used. The DP method provides the benchmark for performance improvements by solving the optimal control problem with a perfect knowledge of the future behavior [51]. Due to the high computational and prediction requirements, DP cannot be used for real-time control of the autonomous vehicle. On the other hand MPC is becoming a standard choice when dealing with multivariable, constrained systems and can be used for real-time control [64] of the velocity trajectory, which can then be used to evaluate FC.

The remainder of this chapter is organized as follows. Section 3.2 presents the model of the vehicle and the problem statement. Section 3.3 shows the application and results of DP for the vehicle following problem. Additionally, it reports the experimental results from chassis dynamometer testing. Section 3.4 presents three different formulations for MPC implementation and compares them. Section 3.5 utilizes a velocity prediction algorithm to feed inaccurate lead trajectories to MPC. Section 3.6 is a short discussion on the results obtained and Section 3.7 concludes the chapter.

3.2 Model and Optimization Constraints

3.2.1 Model Description

In this chapter, the dynamics of the autonomous vehicle are described by a simple point mass Linear Time-Invariant (LTI) model, with position p and velocity v as states and acceleration a as the only input, namely

$$(3.1) \quad x_{k+1} = \underbrace{\begin{bmatrix} 1 & T_s \\ 0 & 1 \end{bmatrix}}_A x_k + \underbrace{\begin{bmatrix} 0.5T_s^2 \\ T_s \end{bmatrix}}_B u_k$$

with $T_s = 0.1\text{s}$ the sampling time, $x = [x_p \ x_v]^\top = [p \ v]^\top \in \mathbb{R}^2$ completely measurable and $u = a \in \mathbb{R}$. The simple dynamics allow for fast online controller implementation. The velocity state v can be used offline in the ALPHA model to estimate the Fuel Consumption and hence the Fuel Economy of the vehicle. Define \mathbb{U} and \mathbb{X}_k as polyhedral sets of constraints on inputs and states respectively, such that

$$(3.2a) \quad \mathbb{U} = \{u \in \mathbb{R} \mid u^{\min} \leq u \leq u^{\max}\}$$

$$(3.2b) \quad \mathbb{X}_k = \{x \in \mathbb{R}^2 \mid [x_{p,k}^{\min} \ x_v^{\min}]^\top \leq x_k \leq [x_{p,k}^{\max} \ x_v^{\max}]^\top\}.$$

The model does not consider the engine, vehicle or powertrain dynamics and is a general formulation applicable to all vehicle types. The resulting optimized velocity trajectory is applied as an input to the ALPHA model [3] of a particular vehicle for offline computation of fuel economy. The results for FE shown in this paper are specific to the 2013 Ford Escape with a 1.6L EcoBoost[®] engine [4]. The absolute values of fuel economy would change for different vehicles with other powertrain and engine configurations.

3.2.2 Velocity and Position Constraints

After defining the formulations for velocity smoothing, we shall now define the constraints on the optimal control problems. The constraints on the drive cycle optimization assumed in this thesis are time varying position limits based on the lead vehicle's velocity for safe and close following. These constraints are different from the certification limits imposed by the EPA for their fuel economy testing. According to their constraints only ± 2 MPH deviation within 1 s from the certification velocity trace is allowed. These constraints are very restrictive and in the case of autonomous

vehicles the extra degree of freedom of staying within safe distance can be used. The resulting profile would completely change from an average human thus resulting in a very different velocity profile beyond the EPA limits.

Specifically, the gap between the lead and the following vehicles is constrained by lower and an upper bound. The lower bound, a *safety limit*, is the closest distance that the follower vehicle can trail the lead vehicle. This is derived from being one car length behind the lead vehicle for every 10 MPH, a common safety length recommended [50]. The upper bound is the longest distance the autonomous vehicle can fall behind the lead vehicle. This is derived from assuming a distance that would prevent safe cut-ins from adjacent lanes and is kept at 2.7 m/m/s(4 ft/MPH). The spacing function comes from results presented in a US Department of Transport study on traffic flow theory [2] for vehicle following in a tunnel. The resulting table is reproduced here in Fig. 3.2. The constraints applied in this thesis, are the most aggressive following from the table.

The constraints are further relaxed at low speeds of less than 20 MPH to 10 ft/MPH. Indeed, at such low speeds cut-ins are not expected and a longer gap reduces frequent starts and stops, thus delivering better FE. Since the position constraints are dependent on the lead vehicle's states at that instant, these constraints are time varying.

Fig. 3.1 shows the upper and lower bounds on position at different velocities of the lead vehicle. Also, the constraints ensure that the autonomous vehicle has to cover the same distance in the same time as the standard drive cycle. The constraints on position and speed are selected according to

$$(3.3a) \quad x_{p,k}^{\min} = x_{L,k} - v_{L,k} L/10$$

$$(3.3b) \quad x_{p,k}^{\max} = x_{L,k} - \begin{cases} v_{L,k} d_{\max} & \text{if } v_{L,k} < 20\text{MPH} \\ v_{L,k} d_{\min} & \text{otherwise} \end{cases}$$

$$(3.3c) \quad x_v^{\min} = 0$$

$$(3.3d) \quad x_v^{\max} = 40$$

where x_L is the position of the lead vehicle, v_L is the velocity of the lead vehicle, L is one car length or 4.5 m, d_{\max} is 3 m (10 ft) and d_{\min} is 1.2 m (4 ft). The stationary

Table 4.5 Macroscopic Flow Data

Speed (m/sec)	Average Spacing (m)	Concentration (veh/km)	Number of Vehicles
2.1	12.3	80.1	22
2.7	12.9	76.5	58
3.3	14.6	67.6	98
3.9	15.3	64.3	125
4.5	17.1	57.6	196
5.1	17.8	55.2	293
5.7	18.8	52.6	436
6.3	19.7	50	656
6.9	20.5	48	865
7.5	22.5	43.8	1062
8.1	23.4	42	1267
8.7	25.4	38.8	1328
9.3	26.6	37	1273
9.9	27.7	35.5	1169
10.5	30	32.8	1096
11.1	32.2	30.6	1248
11.7	33.7	29.3	1280
12.3	33.8	26.8	1162
12.9	43.2	22.8	1087
13.5	43	22.9	1252
14.1	47.4	20.8	1178
14.7	54.5	18.1	1218
15.3	56.2	17.5	1187
15.9	60.5	16.3	1135
16.5	71.5	13.8	837
17.1	75.1	13.1	569
17.7	84.7	11.6	478
18.3	77.3	12.7	291
18.9	88.4	11.1	231
19.5	100.4	9.8	169
20.1	102.7	9.6	55
20.7	120.5	8.1	56

Figure 3.2: Table reproduced from [2] which shows the average vehicle spacing based on speed.

distances are defined as 2 m as the lower bound and 15 m as the upper bound. The time-invariant limits on the speed between 0 – 90 MPH or 0 – 40 m/s are reasonable on almost all US roads [65].

In this thesis, the universal lead velocity trace v_L was determined by introducing a hypothetical lead vehicle. When followed by a human it results in EPA standard drive cycles, and when followed by the optimization algorithms it results in the optimal drive cycles. Through this approach, human and autonomous optimized driving can be compared with the same baseline lead. The concept of the the hypothetical lead and its derivation from the standard cycles are explained in detail in the previous chapter II.

The acceleration and deceleration constraints are time-invariant. For this thesis they have been derived from the standard drive cycles to be $u^{\min} \equiv -6 \text{ m/s}^2$, and $u^{\max} \equiv 6 \text{ m/s}^2$. The same is true for the state x_v or velocity v where $v^{\min} \equiv 0 \text{ m/s}$, and $v^{\max} \equiv 40 \text{ m/s}$. Constraints on the state x_p or position p however, are time varying as the position of the autonomous vehicle is determined by the position and velocity of the hypothetical lead and hence a speed dependent gap.

3.3 Dynamic Programming

The objective of this chapter is to indirectly minimize the FE of the autonomous vehicle by minimizing its accelerations and decelerations. The optimal velocity trajectory has to be computed while keeping the vehicle within the position constraints governed by the lead vehicle. Assuming that all future references, constraints, and disturbances are perfectly known, dynamic programming (DP) can be used to find a non-causal, global-optimal input (acceleration) sequence that minimizes a defined cost function [51]. In this work the input or the acceleration itself has to be minimized. The DP methodology would provide the minimum input, acceleration and deceleration necessary to ensure that the vehicle adheres to its position constraints.

Despite its limitation as an offline technique, DP results serve as an upper bound on FE improvements for the design of real-time control strategies. The formulation

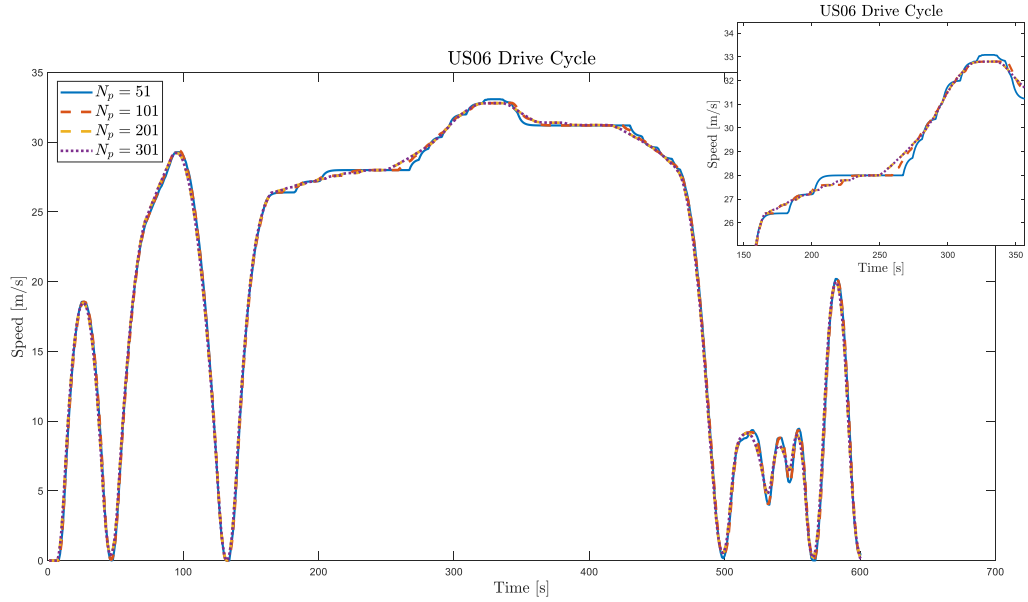


Figure 3.3: DP results with different discretization grid points.

is as follows

$$(3.4a) \quad \min_u \sum_{k=1}^{N_f} \|u_k\|_2^2$$

$$(3.4b) \quad \text{s.t. } x_{k+1} = Ax_k + Bu_k$$

$$(3.4c) \quad u_k \in \mathbb{U}, x_k \in \mathbb{X}_k$$

where N_f is the final time-step, A , B are defined as in (5.2) and \mathbb{U} , \mathbb{X}_k are defined as in (3.2), constraints on \mathbb{X}_k are defined as in (3.3).

For this thesis the generic dynamic programming MATLAB[®] function in [52] has been used. It allows for constrained optimal control problems, such as the one in (5.3). In this work, the states and the inputs are discretized into 201 grid points. The same discretization is applied across all drive cycles. Increasing the discretization grid points, can result in a better solution as the optimizer has more input points to try. However, increasing the grid points also increases the computation time, and even for this problem with just two states and one input, for a long drive cycle like the LA92, it can result in a significantly long computation time. To consider this trade-off, we tried increasing the number of grid points till significant further improvements were not observed. The results are shown in Fig. 3.3 where no difference in the optimized velocity trajectory is observed when the number of grid points are

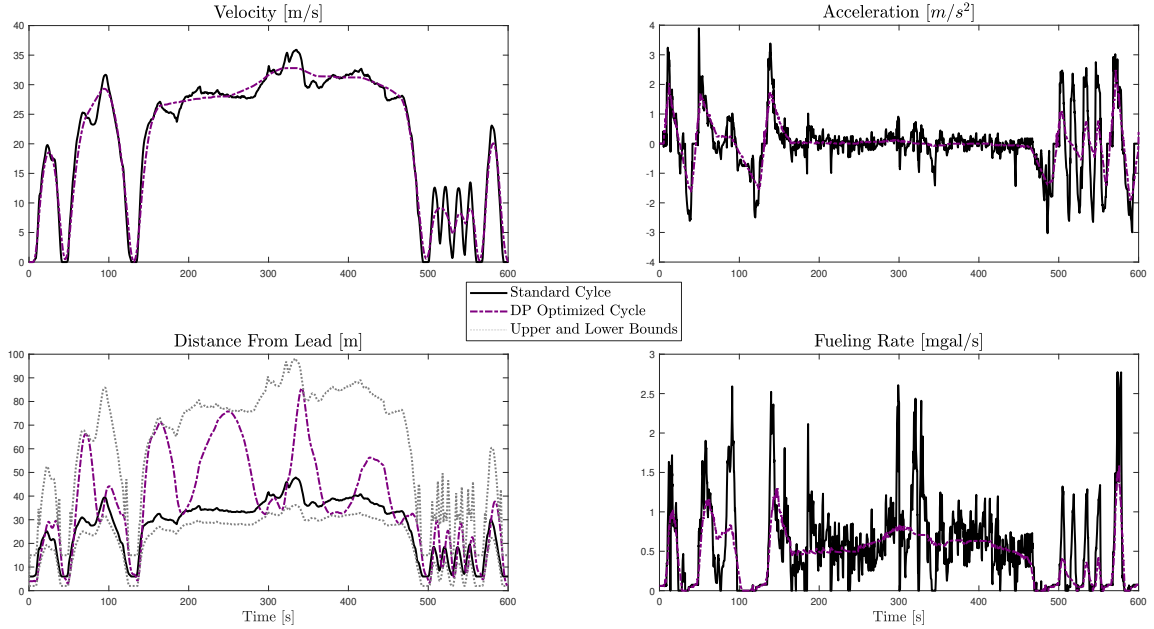


Figure 3.4: Comparison of standard US06 drive cycle with the DP optimized velocity profile. The fueling rates are found from ALPHA model simulations [3].

increased from 201 to 301. All fuel economy values, including those of the SD cycles are calculated by applying the velocity trajectory as an input to the ALPHA model.

3.3.1 Simulation Results

The resulting optimal velocity trajectory showed significant improvements in FE for four US Environmental Protection Agency (EPA) drive cycles as presented in Table. 3.2. A significant increase in FE was seen in US06 at 16.7% over the standard US06 drive cycle. Figure 3.4 shows velocity trajectory of the optimal trace as compared to the standard EPA defined trace. It can be seen in the top left plot, that the optimized drive cycle in purple is much smoother than the SD cycle. From the top right plot, it is clear that the accelerations of the optimized cycle are much lower than those of the SD cycle, which shows that the optimization objective is achieved. The bottom left plot shows that the position constraints imposed on the optimization were met by the DP algorithm. Finally, the bottom right plot shows the reduction in fueling rate, over the drive cycle. Most notably, in the initial 100 s, the optimized cycle is able to reduce the fueling rate significantly over the SD cycle by lowering the acceleration. And also in the final 100 s, by avoiding the frequent accelerations and decelerations. In the middle portion of the drive cycle, the persistent

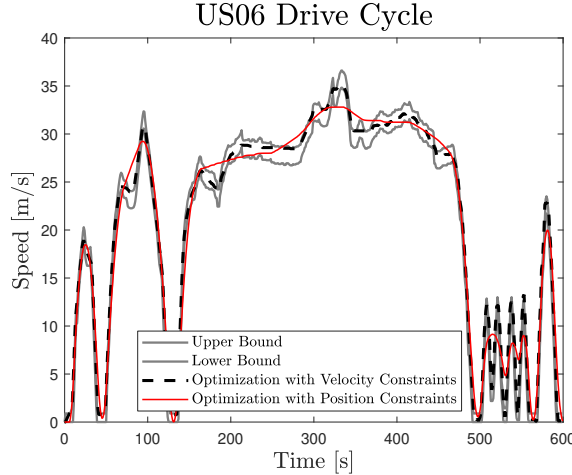


Figure 3.5: EPA defined constraints on velocity required for a certifiable FE test. The DP optimized velocity trajectories adhering to the velocity and position constraints respectively are shown.

change in velocity was avoided, and this results in a trajectory that is favorable from a passenger’s point of view. Hence, such a technology would be desirable from a consumer perspective. In essence, the optimization by utilizing the entire gap between the upper and lower bounds, DP is able to find the velocity trajectory with minimal accelerations and decelerations while remaining close to the lead vehicle. The absence of these acceleration spikes reduces fueling rates and leads to the significant improvements in FE.

Also, Fig. 3.5 shows the EPA specified velocity bounds [66]. As mentioned before, deviations in velocity during testing are allowed within these bounds. The exact regulation is that at a particular time step, the maximum velocity is +2 MPH over the maximum velocity within ± 1 s and the minimum velocity is -2 MPH below the minimum velocity within ± 1 s. This is a fairly large bound as shown in Fig. 3.5. We used these constraints to optimize the velocity and were able to achieve up to 8% improvement in FE. Having said this, it is not possible for human drivers in real time to be able to expertly navigate these bounds, as they don’t appear on the screen. This is an academic exercise to show the possible improvements with a perfect controller. Moreover, these velocity constraints originate from the original human driven drive cycles and hence force the optimized velocity trajectory to adhere to human driving. We argue, that the position constraints are better for the autonomous vehicle as it allows for optimization within tangible bounds that are practically implementable. The DP optimized velocity with the position constraints, violated the velocity bounds

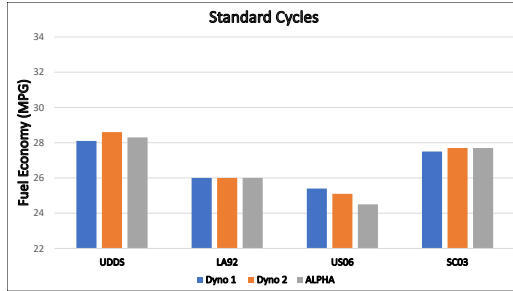


Figure 3.6: The two chassis dynamometer runs are shown in comparison with the simulation results

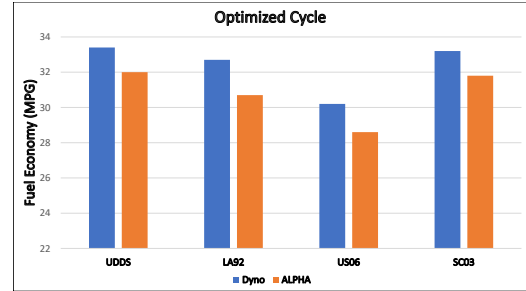


Figure 3.7: The chassis dynamometer run is shown in comparison with the simulation results

on several occasions as also shown in the figure.

3.3.2 Experimental Results

The simulation results for the DP optimization, stated above were also experimentally validated at the US EPA’s Ann Arbor facility. The US EPA’s Nation Vehicle and Fuel Emission Laboratory (NVFEL) is the certification site where the chassis dynamometers are used to certify production vehicles for fuel economy and emission ratings. The state of the art facility is run by the US EPA and the lab is ISO/IEC 17025:2005 accredited for emissions testing.

The test cell conditions are closely monitored and maintained to ensure consistent testing environments. Fuel consumption is measured from the tailpipe carbon emissions for greater accuracy. The vehicle considered in this study, the 2013 Ford Escape with a 1.6L EcoBoost engine has been validated on the same experimental set up against the ALPHA. The results were presented in [3]. Hence the dynamometer calibrations have already been worked out and they apply a road load based on the vehicle speed. A professional driver who drives the certification cycles drove for our experiments as well, a separate screen outside the vehicle showed the present and future speeds for the driver to follow. Since this was the certification facility, any deviation outside the certifiable bounds would be automatically rejected.

All the experiments were completed with fully warmed-up conditions. The UDDS was driven to warm up the vehicle (the engine and the transmission) before the actual tests. The tests were conducted with the SD cycle, followed by the optimized cycle, and followed again by the SD cycle. This procedure was repeated for all four SD cycles considered in this chapter. The raw experimental data is presented in Table 3.1.

Table 3.1: Raw Experimental Results

EPA Cycle	Test	Fuel Economy	THC (mg)	CO (mg)	NO _x (mg)	CO ₂ (mg)	CH ₄ (mg)	NO _x (mg)	PM (mg)
UDDS	Dyno 1	28.094	0.0229	0.5776	0.0249	315.9800	0.0040	0.0449	0.1124
UDDS	Dyno	33.380	0.0072	0.2507	0.0102	266.3500	0.0027	0.0152	0.0288
UDDS	Dyno 2	28.579	0.0158	0.4007	0.0223	310.9100	0.0037	0.0356	0.0579
US06	Dyno 1	25.415	0.0309	0.6999	0.0960	349.1700	0.0100	0.1185	0.2641
US06	Dyno	30.149	0.0141	0.2898	0.0246	294.8600	0.0087	0.0308	0.0924
US06	Dyno 2	25.107	0.0116	0.6267	0.1047	353.6500	0.0104	0.1066	0.1508
LA92	Dyno 1	25.957	0.0120	0.5247	0.0389	342.1900	0.0068	0.0447	0.0182
LA92	Dyno	32.656	0.0061	0.2054	0.0153	272.3400	0.0044	0.0174	0.0146
LA92	Dyno 2	25.945	0.0146	0.5056	0.0593	342.3700	0.0080	0.0667	0.0199
SC03	Dyno 1	27.458	0.0127	0.3381	0.0399	323.7400	0.0079	0.0455	0.0676
SC03	Dyno	33.168	0.0081	0.2099	0.0249	268.1200	0.0049	0.0285	0.0541
SC03	Dyno 2	27.647	0.0171	0.4207	0.0440	321.3600	0.0093	0.0527	0.0659

The results comparing the SD cycles are shown in Fig. 3.6. Here Dyno refers to the results from actual dynamometer testing and ALPHA to the simulation results. Specifically, Dyno 1 is the first SD cycle test and Dyno 2 the second SD cycle test. It should be noted, that the x-axis starts at 22 MPG, thus clearly the simulation software is able to perform well and the experimental and simulation results match well. Since a driver drove both Dyno traces, there is some discrepancy between Dyno 1 and Dyno 2, however these are very small and the professional driver was able to maintain consistency. These FE results match well with the ALPHA simulations also shown with the gray bar. For the four, very different drive cycles that have significantly varying accelerations and top speeds, ALPHA performed well for all. This result validates the ALPHA model as a simulation tool.

The results comparing the optimized cycles are shown in Fig. 3.7. These results from experiments show that the predicted improvements are better in actual experimentation than what was predicted by simulation in all cases. This is a consistent difference between the actual dynamometer testing and the ALPHA simulations. We speculate that this is due to the high controller gains in the driver model, to ensure that the SD cycles are accurately followed, however for these smoother cycles, they overcompensate and increase the fueling rate beyond what an actual driver would do. We know that the experimental trace would not deviate from the given drive cycle by more than the EPA specified bounds of ± 2 MPH. However, there is still a wide range for the driver to exploit. In any case, the good correlation in the SD cycles and the consistent trend in the optimized cycle, makes us believe that the

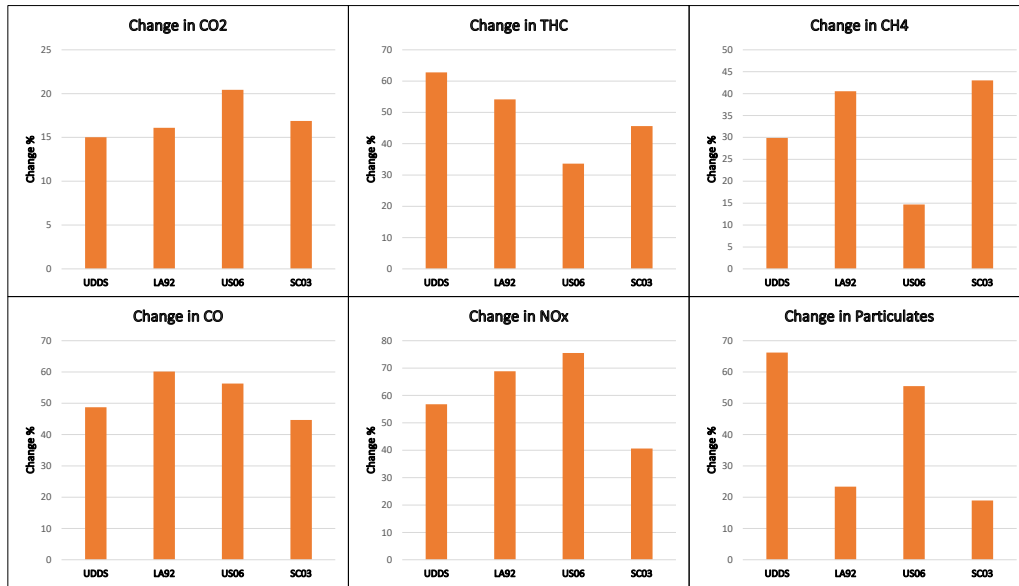


Figure 3.8: Experimental results showing changes in different parameters from the standard cycle to the optimized one

simulation results are qualitatively correct. The experimental results validate our conclusion that velocity smoothing can result in significant improvements over the SD cycles, with improvements of up to 25% in experimentation.

A further benefit of using the US EPA’s vehicle dynamometer testing facilities was the ability to access their bag emissions results. The emissions testing bench confirms to Code of Federal Regulations (CFR) Title 40 part 86, part 1065, and part 1066. This regulation closely sets the testing equipment for its length, thickness, insulation etc. The tailpipe emissions from the vehicle are diverted into bags for analysis later. Since this is a bag analysis we can only get the integral results for the whole drive cycle and not the time resolved continuous data, which would allow for more insight.

The results for various emission gasses are shown in Fig. 3.8. The top left plot shows the reduction in carbon di-oxide (CO_2), the main greenhouse gas (GHG), which we are trying to reduce. From the experimental results, we can show a reduction between 15 – 20% in total CO_2 emissions. To put this result in perspective, we used a simple double integrator acceleration model which did not take into account any of the vehicle’s parameters, and from an offline drive cycle optimization, we were able to reduce CO_2 by more than 15%. This result is less than the 33% shown in [31],

but that evaluation was not based on actual experimental testing. Still, the significant reduction in this global warming causing gas by automated eco-driving should encourage regulators to coax implementations of these systems. The reductions came about without any changes to the vehicle hardware, trip duration or length and were shown to be valid over a range of road conditions and driving styles.

Amongst the other tailpipe emissions, the total hydrocarbon content (THC) reduced over 60% for the UDDS drive cycle and more than 30% for the US06 drive cycle. In absolute terms, the maximum THC emissions were seen for the SC03 drive cycle at 2.2 mg/mile, which is still almost half of the original 4.1 mg/mile for SD. The optimization was only set for reducing the velocity deviations and not emissions however, a significant decrease is observed. Similarly, the methane (CH_4) and carbon monoxide (CO) content also reduced significantly. Again the maximum emissions were for the SC03 drive cycle where the methane emissions reduced from 2.4 mg/mile to 1.4 mg/mile; while the carbon monoxide emissions reduced from 105 mg/mile to 58 mg/mile. To remind the readers, CH_4 is presently regulated at only 8 mg/mile and CO at 1700 mg/mile, hence with the use of optimized automated driving, a steep increase in emission reductions can be sought. The most dramatic reduction was in the oxides of nitrogen (NO_x) where the more than 70% reduction was seen in the US06 drive cycle. And once again the maximum emissions were for the SC03 drive cycle, where the NO_x emissions reduced from 1.2 mg/mile to 0.7 mg/mile. Presently NO_x is regulated at only 300 mg/mile so a considerable reduction can be achieved.

The SC03 drive cycle was specifically designed for evaluating drive cycle emissions with the A/C on. It has slow accelerations and deceleration bounded by $\pm 2.5 \text{ m/s}^2$ or $\pm 5.6 \text{ MPH/s}$ but they are sustained as shown in Fig. 3.9. These are somewhat reduced by the optimization through DP, however, we found that the maximum emissions in terms of *mg/mile* came from this drive cycle. This indicates that frequent velocity changes lead to an increased emission, which is logical given that frequent pedal tip-ins cause the air-fuel ratio to deviate from its set point. Even a slightly deviant air-to-fuel ratio will considerably reduce the ability of the three-way catalyst to cut emissions. The same logic applies for the reduction in emissions from the optimized cycles as a reduction in velocity deviations results in a reduction in air-to-fuel ratio deviations. Unfortunately, since our only data is bag emission based, we cannot evaluate this speculation. A future study should use a time-resolved emissions bench

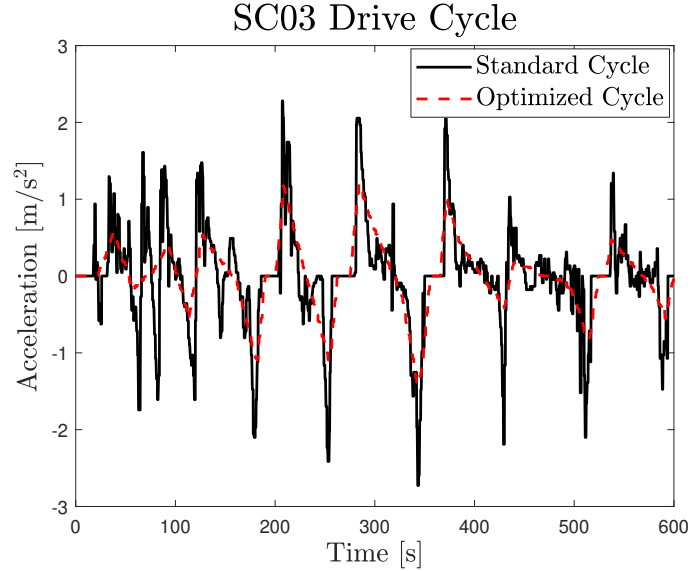


Figure 3.9: SC03 drive cycle accelerations for the SD cycle and the optimized one

to understand the exact time locations of emission reduction.

Another interesting note is that for the gasoline engine evaluated in this experimental set-up, the reduced engine demand does not seem to have any impact on the catalyst temperature. In diesel engines, where the catalyst temperature plays a significant role in the after treatment system, it has been shown before that velocity smoothing leads to higher emissions. Based on our results we don't have to worry about reducing catalyst temperature for a gasoline engine.

In this section, we have experimentally evaluated the simulation results from DP to show that significant improvements are possible and our simulation model ALPHA is valid. We have also shown that while emissions reduction was not an objective of this optimization, by the very nature of our optimization, substantial decrease is possible, even in the worst case of the SC03 drive cycle.

3.4 Model predictive control

Although DP provides the optimal solution, several reasons prevent its use for online control such as the high computational burden and the complete knowledge about the future behavior of the system. The Model Predictive Control (MPC) methodology is becoming the standard technology to handle fast-sampled multi-variable processes, especially in automotive, aerospace and power electronics control [64, 67, 68, 69]. This methodology solves a constrained, finite-horizon, optimal

control problem, and by following the receding horizon policy it applies only the current inputs to the system. At each sampling time the procedure is repeated and a new open-loop optimal control problem is solved with a one-step shifted horizon. Even if MPC drastically reduces the computational complexity with respect to DP, the time required to solve the optimization problem is still considerable, especially in high frequency sampled systems [70]. However, recent advances in convex and embedded optimization are enabling fast online MPC implementations [71, 72, 73].

When dealing with LTI models in our case, quadratic cost function and affine constraints, MPC simplifies to solving the following optimization problem at each sampling instant

$$(3.5a) \quad \min_u \sum_{i=1}^{\tilde{N}_p} \|W_x(x_{k+i|k} - r_{k+i|k})\|_2^2 + \|W_u u_{k+i|k}\|_2^2$$

$$(3.5b) \quad \text{s.t. } x_{k+i+1|k} = Ax_{k+i|k} + Bu_{k+i|k}$$

$$(3.5c) \quad x_{k|k} = x_k$$

$$(3.5d) \quad u_{k+i|k} \in \mathbb{U}, \quad x_{k+i|k} \in \mathbb{X}_{k+i|k}$$

where \tilde{N}_p is the prediction horizon expressed in sampling instants, W_x and W_u are square, diagonal, weight matrices, $x_{k+i|k}$ denotes the prediction of the variable x at time $k+i$ based on the information available at time k , and $r_{k+i|k}$ denotes the prediction of the reference r to be tracked at time $k+i$, x_k is the current state. The influence of the prediction horizon, $N_p = \tilde{N}_p T_s$ expressed in seconds, to the optimal velocity trajectory will be investigated along with three different MPC formulations. All three formulations share the same linear prediction model and the same constraints, as defined in Eqs. (5.2) and (3.2), respectively. They differ from each other for the cost function, and we will refer to them as

1. MPC^a: penalty on acceleration;
2. MPC^p: penalty on acceleration and position tracking;
3. MPC^v: penalty on acceleration and velocity tracking.

MPC^a can be considered as a reduced horizon version of the optimal control problem (5.3), and its cost function is defined by the following weights:

$$(3.6) \quad \text{MPC}^a \triangleq \begin{cases} W_x^a = \text{diag}[0 \ 0] \\ W_u^a = w_u^a = 1 \end{cases}$$

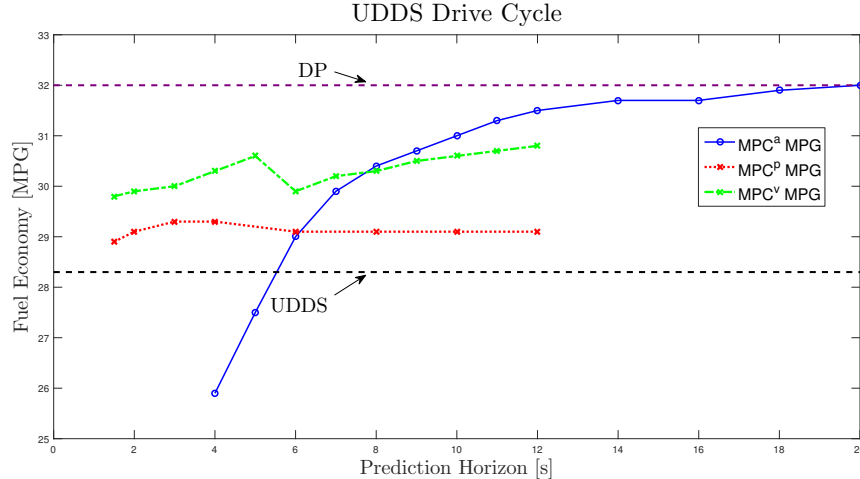


Figure 3.10: Fuel economy using various horizons and cost functions in the MPC formulation

The length of the prediction horizon plays an important role in this control problem as not only the dynamics of the model are predicted but also the constraints on the states and the eventual reference trajectory. This means that long prediction horizons are not only computationally demanding, but can even be infeasible depending on the preview, look-ahead, and overall connectivity responsible for accurately predicting the future behavior of the system. Indeed, in [74], it was shown that while velocity trajectories for short prediction horizons can be predicted well for $N_p = 1.5$ s, a good accuracy for longer horizon is not very probable.

For autonomous driving it can be assumed that these predictions come from different methods such as vehicle to vehicle communication or from a traffic monitoring system. Given different prediction horizons, this work evaluates the potential increase in fuel economy. It must be stressed that for this section, perfect prediction of constraints along the prediction horizon is assumed for all cases.

Fig. 3.10 shows that MPC^a gives satisfactory results only for $N_p \geq 6$ s. This is a significantly long prediction horizon and would not be feasible. For shorter prediction horizons $N_s < 5$ s, MPC^a gives an FE that is even worse with respect to the standard cycle. The reason is clarified in Fig. 3.11, which shows that without enough prediction of the position constrains, MPC^a keeps the vehicle too close to the lower bound. This leads to acceleration spikes to keep the vehicle within the bounds, decreasing the FE. Fig. 3.10 also shows that, as expected, the performance of MPC^a equals the one obtained with DP after a certain prediction horizon, i.e. 20s, as the two formulations are equivalent but for the prediction horizon. The RMS

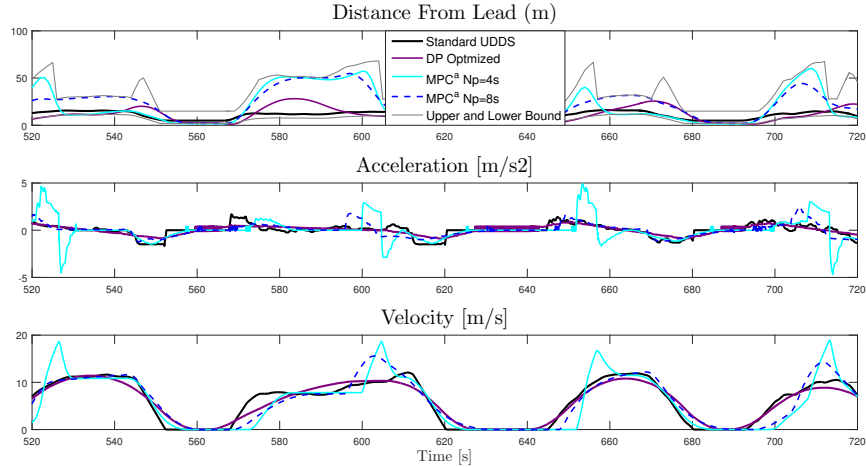


Figure 3.11: Comparison of standard UDDS drive cycle with DP and MPC^a velocity traces. Clearly for MPC^a with $N_p = 4s$, at Time = 530, 605, 655 and 715 s the position is too close to the lower bound and the MPC^a controller applies significant acceleration to stay within the bounds. These accelerations are less pronounced for the $N_p = 8s$ case and absent in the DP case.

error between the velocity trajectory in DP and MPC^a vary as 2.24 m/s for $N_p = 4s$, 1.26 m/s for $N_p = 8s$ and 0.58 m/s for $N_p = 20s$ thus showing how the MPC^a results approach the DP ones.

3.4.1 Model predictive control with tracking penalty

From the results of MPC^a, the vehicle had to be prevented from falling too close to the lower bound on position. Since the state vector is completely measurable, the deviation from the position or velocity reference can be penalized to ensure that the vehicle is within acceptable bounds. The MPC implementations, MPC^p and MPC^v introduce two different tracking penalties in the cost function. It is straightforward to verify that penalizing the velocity or position tracking error worsens the FE for longer prediction horizons, where MPC^a works well. However, as shown in Fig. 3.10, the performance improvement for shorter prediction horizons is significant.

In MPC^p, the position state is forced to track the upper bound of the position constraints. This ensures that the position of the vehicle is far from the lower bound. However, position tracking limits the ability of the controller to utilize the entire gap between the bounds and minimize acceleration. An alternative is MPC^v, where the controller is forced to track the velocity of the lead vehicle. Tracking the lead velocity would ensure that for short prediction horizons, the FE at least matches that of the standard cycle. Additionally, acceleration optimization would increase

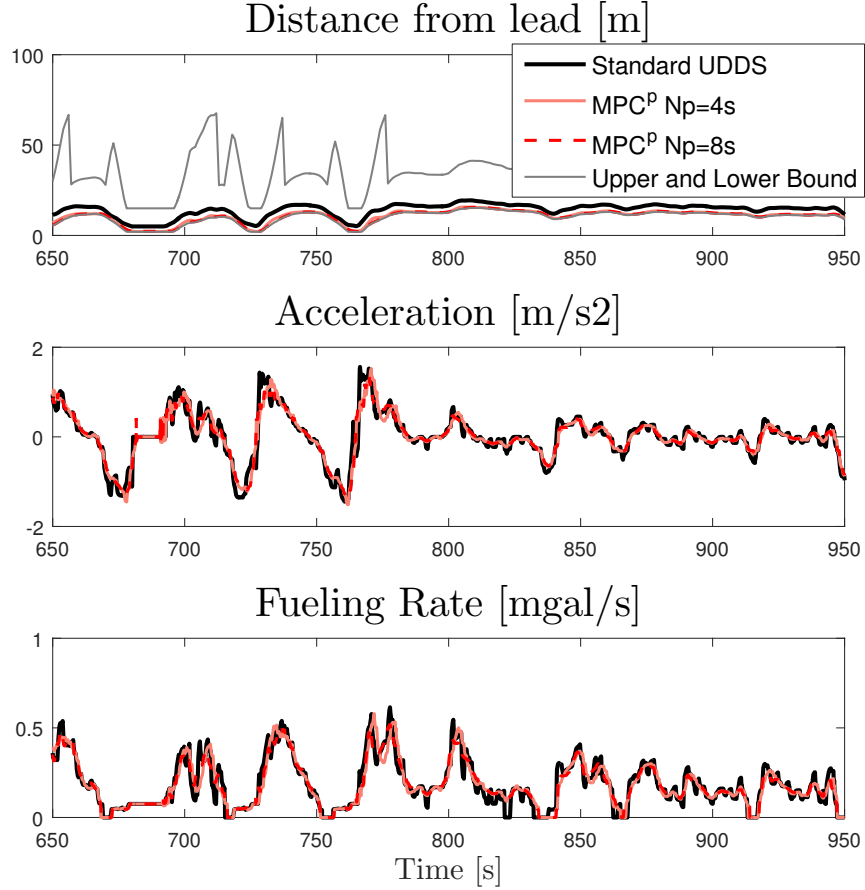


Figure 3.12: Comparison of standard UDDS drive cycle with two MPC filtered velocity traces where the MPC has position tracking in the cost function. Clearly with increased prediction horizon, the position tracking improves. However, the reduction in acceleration between the two MPC cases is small leading to very slight improvement in FE

FE to a value beyond that of the standard cycle. The tradeoff between acceleration optimization and velocity tracking by employing appropriate weights for different prediction horizons are discussed below.

In MPC^p the weights on the cost function are assumed to be

$$(3.7) \quad MPC^p \triangleq \begin{cases} W_x^p = \text{diag} [w_x^p \ 0] \\ W_u^p = w_u^p \end{cases}$$

whereas the weights for MPC^v are such that

$$(3.8) \quad MPC^v \triangleq \begin{cases} W_x^v = \text{diag} [0 \ w_x^v] \\ W_u^v = w_u^v \end{cases}$$

Since the main objective is minimization of acceleration, the weights were chosen such that $w_u^p > w_x^p$ and $w_u^v > w_x^v$. This rule ensures that the penalty on tracking

Table 3.2: Fuel Economy Improvements

Cycle	Standard Cycle FE (MPG)	DP		MPC ^v $N_p = 1.5$	
		FE (MPG)	% increase	FE (MPG)	% increase
UDDS	28.3	32	13.1	29.8	5.3
LA92	26	30.7	18.1	28.2	8.5
US06	24.5	28.6	16.7	27.4	11.8
SC03	27.7	31.8	14.8	29.2	5.4

is less than the penalty on high acceleration. In the proposed results, the weights are tuned for each prediction horizon. For longer prediction horizons the tracking accuracy can be reduced, thus giving freedom for higher acceleration minimization. As an example, for the case $N_p = 1.5s$ the weights are $w_u^p = w_u^a = 1$, $w_x^p = 0.8$ and $w_x^v = 0.2$.

Figure. 3.12 shows MPC^p results for two prediction horizons, i.e. 4s and 8s. The upper bound is closely tracked by both cases and the tracking performance increases slightly as prediction horizon increases. The FE improves over the standard cycle even for short prediction horizons. The close position tracking, however, reduces the scope for optimization and hence the FE for both cases is nearly the same. Fig. 3.10 shows that for $N_p = 8s$, the MPC^a has a much better FE than MPC^p.

It was found that MPC^v showed an even better FE than MPC^p for short prediction horizons. In Fig. 3.13 it can be seen that while staying within the position constraints, MPC^v had lower acceleration and engine torque demands than MPC^a and MPC^p. Clearly the DP case with the entire drive cycle preview is the best for FE. But, for $N_p = 1.5s$ MPC^v shows the best results compared to other possible solutions. MPC^v is therefore selected as our real-time following control implementation.

3.5 Impact of Prediction Quality on Performance

In the previous section, we evaluated MPC results based on perfect predictions, however, that might not be possible in real life. Hence we would have to rely on some imperfect predictions to compute optimal inputs further ahead in the horizon. For imperfect future predicted velocities, we utilized the work in [75]. The authors here developed an algorithm which takes into account the velocity of one or more lead vehicles and predicts future velocity. In this thesis, a velocity trajectory of the HL vehicle is required for the MPC implementation. To clarify the terminology between

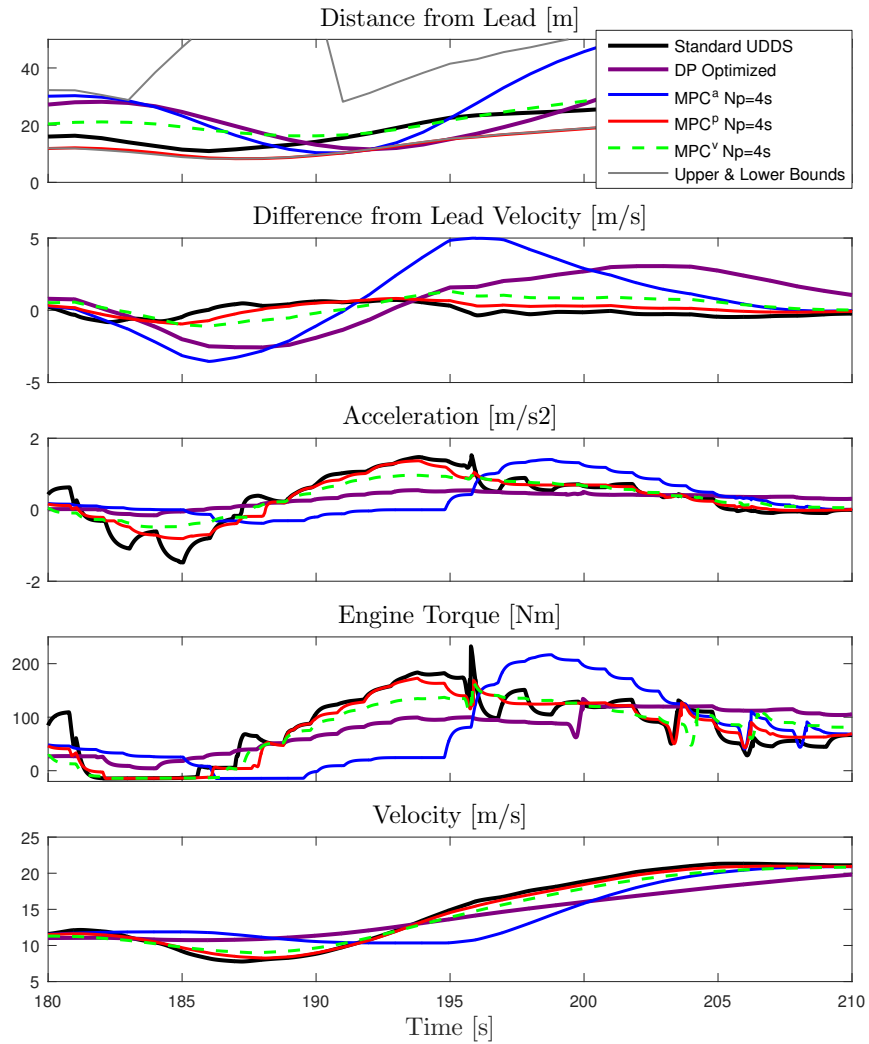


Figure 3.13: Comparison of different drive cycles derived from following the hypothetical lead using DP and MPC algorithms with different cost functions at $N_p=4s$. The acceleration profile of DP is the best followed by MPC with velocity tracking, MPC with position tracking, the standard cycle and finally MPC without reference. This is reflected in the the engine torque and correspondingly the fueling rate.

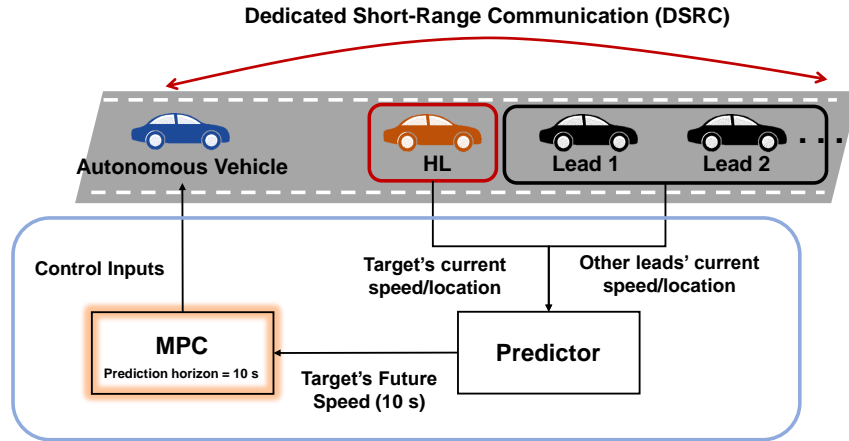


Figure 3.14: Schematic to show the autonomous vehicle with the hypothetical lead (HL). Future velocity of HL is evaluated using past information of the HL and other lead vehicles in front of it.

both works, HL, is the vehicle for which a velocity prediction is required so that it can be followed by the autonomous vehicle, while the ‘lead vehicles’ are those present in front of the HL¹. Information of the lead vehicles are used to predict the velocity of HL. Then the predicted velocity is used to predict the position constraints of the autonomous vehicle, which feeds into MPC to optimize within those constraints.

Since the algorithm produces predictions with some inaccuracies, in this section only the MPC^a formulation is considered so as to avoid tracking inaccurate predictions. Also, as MPC^a started to show better results only with a 10s prediction preview, the same horizon length will be used for prediction and MPC optimization.

3.5.1 Velocity Prediction Algorithm

The simulation case from [75] is used where it can be assumed that the dedicated short-range communication (DSRC) messages are available. This implies that apart from the past speed information from HL, the current speed of all connected leads are also available. This information aids in the future velocity prediction of the lead vehicle as changes in speed can be ascertained from traffic behavior ahead of the lead. The algorithm works by using a linear regression to fit past and future velocities and

¹Target vehicle in [75] is the same as the hypothetical lead in our case

then using the coefficients to predict the future velocity of HL. As shown in Fig. 3.14, the autonomous vehicle is optimally controlled by the MPC, which requires future velocity prediction of the HL. The predictor algorithm is able to do that using the past velocity of the HL as well as the lead vehicles in front of it.

$$(3.9) \quad X_k = \begin{bmatrix} 1 & t_{k-h_k+1} - t_k & \cdots & (t_{k-h_k+1} - t_k)^n \\ \vdots & \vdots & & \vdots \\ 1 & 0 & \cdots & 0 \\ \hline 1 & \hat{t}_{k,1} & \cdots & (\hat{t}_{k,1})^n \\ \vdots & \vdots & & \vdots \\ 1 & \hat{t}_{k,l_k} & \cdots & (\hat{t}_{k,l_k})^n \end{bmatrix} \left. \begin{array}{l} \} \text{Past} \\ \} \text{Future} \end{array} \right.$$

In equation 3.9, t_k is the current time, h_k the number of HL's past speeds used at t_k , limited to maximum of 10. The number of columns in X_k is determined by the order of the polynomial fit used. In this work we consider two cases with a linear and a quadratic fit.

The coefficients β_k can be determined using the weighted least squares estimation as

$$(3.10) \quad \beta_k = (X_k^T W_k X_k)^{-1} X_k^T W_k \mathbf{v}_k$$

where W_k is the weighting matrix and the vector \mathbf{v}_k has the speed data of the predicted vehicle and the speed of lead vehicles collected at time t_k :

$$(3.11) \quad \mathbf{v}_k = [v_{k-h_k+1}^{HL}, \cdots, v_k^{HL} | v_{k,1}^L, \cdots, v_{k,l_k}^L]^T$$

Hence finally, the predicted velocity \hat{v}_{k+f} can be calculated by

$$(3.12) \quad \hat{v}_{k+f} = \sum_{i=0}^n \beta_{i,k} \cdot (t_{k+f} - t_k)^i$$

where t_{k+f} is future time after a time step f .

3.5.2 Velocity Optimization using Predicted Lead Velocity

The velocity of the autonomous vehicle is optimized for 10 s, where the constraints in the 1st second come from the actual velocity of HL and next 9 s come from the

Table 3.3: Prediction Quality Performance

Cycle	% Improvement over baseline SD				
	Predicted Perfect	Predicted Linear	Predicted Quadratic	Fixed Velocity	Fixed Acceleration
UDDS	3.5	0.7	1.4	-2.1	-0.7
US06	12.2	4.0	10.2	-2.0	9.8
LA92	9.2	-1.9	3.8	N/A	0.0

prediction algorithm. MPC^a implements the optimal input for the next instant but optimizes for the entire prediction horizon. Then the window shifts to the next 10s and MPC optimizes again. This procedure continues for the entire drive cycle. In this first attempt only a single lead in front of the HL was assumed, and it was also assumed that both the HL and Lead 1 from Fig. 3.14 were executing the same velocity trajectory with a 1s delay.

The baseline FE case is the SD cycle, which going back to Fig. 2.1 is obtained when the HL is followed by the IDM algorithm. The results for velocity optimization with prediction are shown in Table 3.3, where up to 10% improvement is possible with a 10s prediction horizon for the US06 drive cycle. This is quite close to the 12% improvement possible with perfect prediction. However, it should also be noted that the drop in FE improvements with the predicted velocity as compared to perfect lead velocity is significant for both the UDDS and LA92 drive cycles. In fact, for the LA92 drive cycle, in the linear case, the MPC algorithm performs worse than the baseline. To remind the readers, baseline IDM simply maintains a specified time headway without any prediction of future lead velocities or optimal controls. Hence, the inaccuracies in prediction can cause a worse performance than the baseline.

The prediction algorithm takes into account historic data of the hypothetical lead and also vehicles ahead of it to fit linear and quadratic polynomials. It was found that the fit with the quadratic polynomial performs better than the linear one, with almost double the improvements for the three drive cycles considered. The reason is that, the linear fits over-predicts future velocities, which in turn lowers the lower bound as it is assumed that the HL is faster and so the position constraints are wider. However, since the actual lead vehicle velocity is lower, the actual lower bound is higher than predicted, which forces abrupt accelerations to stay within the bounds.

This phenomenon can be seen in Fig. 3.15, where left plot shows the velocity and the right one the position. The blue line is the actual velocity of HL, and the red lines coming from that are the predicted velocities of HL at every time step. Clearly,

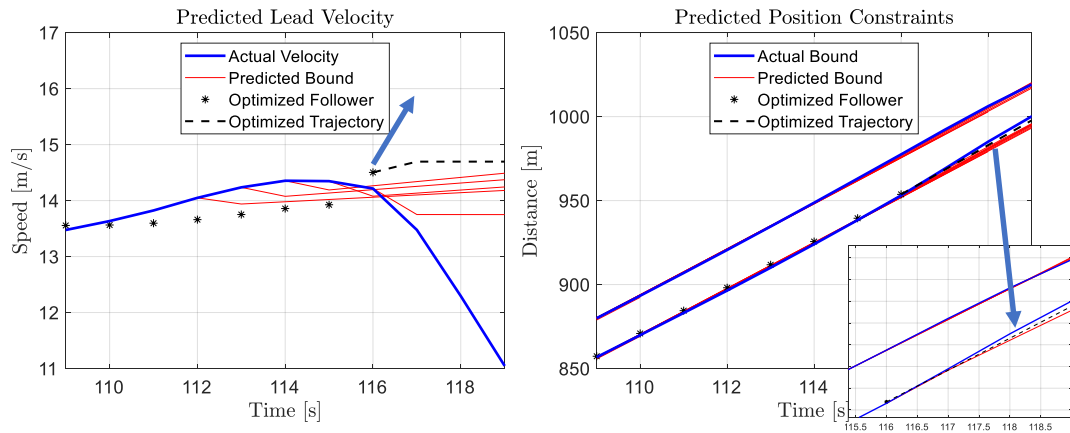


Figure 3.15: Snapshot of optimized autonomous follower at 116s. Clearly, the optimized trajectory is outside the actual position bounds and therefore with new information at 117s, the optimized follower will have to accelerate to stay within the bounds

the predicted velocity is higher than the actual velocity. This makes the predicted constraints to be wider than the actual constraints, as lower velocity means that the following autonomous vehicle should be closer to HL. Hence, the red predicted lines are always diverging away from the actual blue line in the position constraints plot. Therefore, when MPC optimizes it assumes the lower bound to be lower than actual, and future velocities are planned to stay within those predicted bounds. Hence, when it plans for the future, the trajectory is within the expected bounds but outside of the actual ones. The snapshot is at 115s, where we know perfectly what the HL will do at 116s, so the MPC optimizes for the input vector for the next 10s and implements, the input for the next s . The optimized future trajectory which is not implemented is shown with the black dotted lines. From the magnified plot of position constraints, it is obvious that the predicted future position trajectory is outside of the actual bounds. However, when the next step with new information, comes at 116s, the optimized autonomous follower has to accelerate to stay within the bounds. Hence, in the velocity plot, the arrow points to the next velocity, which requires a steep acceleration.

The resulting acceleration is awkward as HL is decelerating, while the following

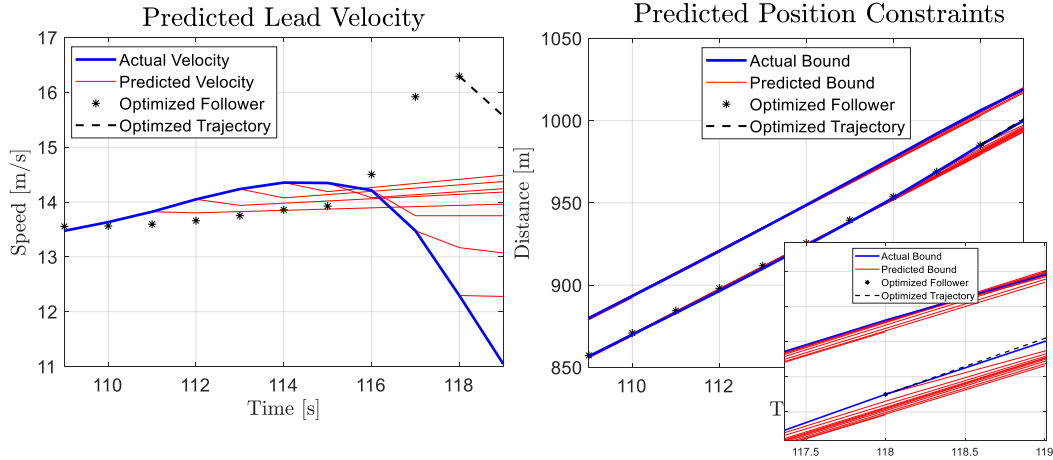


Figure 3.16: Snapshot of optimized autonomous follower at 118s. Now the optimized autonomous follower is within the actual position constraints and hence further acceleration is not required and the optimized trajectory further in the horizon can be realized

autonomous vehicle has to accelerate and then immediately decelerate. Perhaps, a better designed bound might be able to avoid such a situation by allowing for constraint violation through the introduction of slack. However, if the autonomous vehicle is at the maximum position constraint, such as the case at 116s, with inaccurate future information, the autonomous vehicle will always accelerate when the HL decelerates. This is how, inaccurate future information, reduces the optimality of the solution and resulting FE increases.

In Fig. 3.16, we have shown a snapshot at 117s with the MPC optimized velocity and position at 118s. Here, it can be clearly seen in the magnified position constraint plot, that the MPC optimized future trajectories shown with the black dotted lines will stay within the actual constraints. Also, the future optimized velocity trajectory for the follower is decreasing, which is what we want. Hence, now even with inaccurate future predictions, further accelerations are not required. Overall, from Fig. 3.16, the reason for reduced FE with inaccurate predictions are the undesirable accelerations. In this particular case, they occur, when the position of the autonomous vehicle is right at the boundary and future MPC planning violates constraints. This was found to be true at other time instances too and was the primary

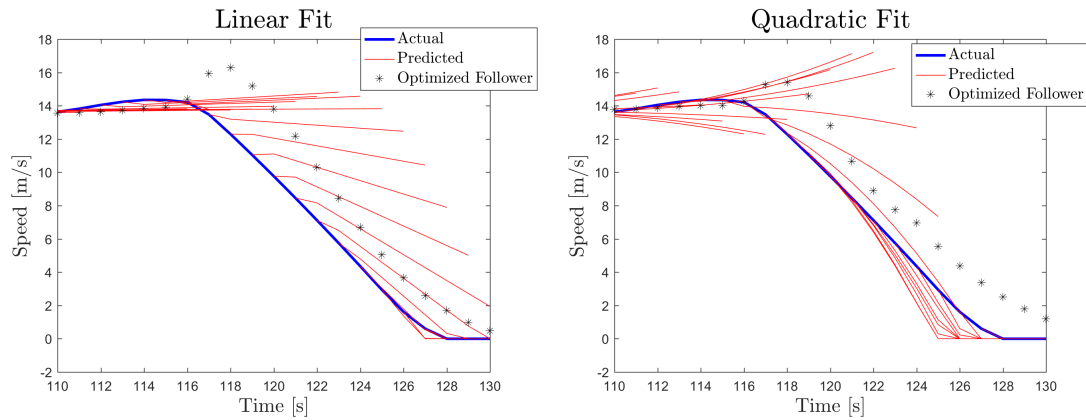


Figure 3.17: Linear and quadratic fits for a selected section of the UDDS drive cycle

reason for increased fueling rate.

Since we could change the order of the polynomial for fitting, it was found that the velocity prediction improved as the RMS error reduced from 2.35 m/s for the linear case to 1.81 m/s for the quadratic case for the UDDS drive cycle. It can be seen in Fig. 3.17 that the quadratic fit is able to predict the impending velocity decrease of HL, much better than the linear fit. Therefore, it can also be seen that the optimized follower does not accelerate as much in the quadratic fit and is able to reduce the increased fueling rate from acceleration. This result was consistent with the rest of the drive cycles and can be seen in Table. 3.3, where the predicted quadratic always performs better than the predicted linear for all three drive cycles considered. Of course, with the quadratic fit it can be clearly seen in Fig. 3.17 that the HL velocity is under-predicted and actual velocity decreases at a slower rate. This would narrow the predicted position constraints and reduce the space for optimization, which is undesirable for optimality. Hence, these FE results are still below the ones obtained with perfect prediction.

3.5.3 Improved Prediction Accuracy

So far, prediction with only 1 leading vehicle has been considered, however, the prediction algorithm also allows for increasing the number of lead vehicles to increase

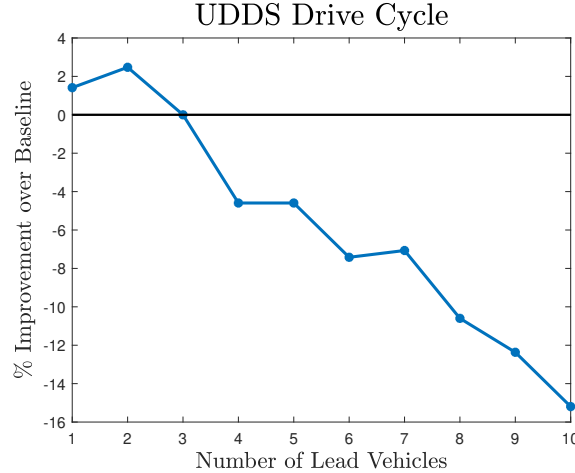


Figure 3.18: Increasing the number of lead vehicles does not improve FE, in fact it results in FE falling significantly below the baseline

the information available to the regression. Referring back to Fig. 3.14, this would involve increasing the number of lead vehicles in front of HL. For this analysis, we assume that all vehicles are executing the UDDS drive cycle but with a time gap of 2s and an initial distance gap of 4m.

It was shown in the velocity prediction paper [75], that increasing the available information reduces the average prediction error. Surprisingly, it was found that increasing the number of lead vehicles had a negative effect on fuel economy improvement and some results were worse than baseline. The results for the UDDS drive cycle are shown in Fig. 3.18, where after increasing the number of lead vehicles beyond 3, FE actually drops below the baseline. These significant reductions in FE come from sudden jerks in the velocity trajectory necessitated by inaccurate prediction. Just like the previous case in Fig. 3.16 the autonomous vehicle falls too close to the constraints and is forced to accelerate to avoid constraint violations.

The reason for falling too close to the constraints is that while the average prediction accuracy improves significantly, the initial prediction accuracy worsens. Prediction errors are shown in Fig. 3.19, where clearly while the prediction error in the 10th second drops significantly for the 10 vehicle case, there is also a significant increase in the prediction error for the 1st second. This leads to the assumption that accurate short horizon prediction is more important than a longer horizon prediction. The assumption makes sense as the optimization is updated every second and hence errors much further in the horizon can be compensated for more easily than those earlier

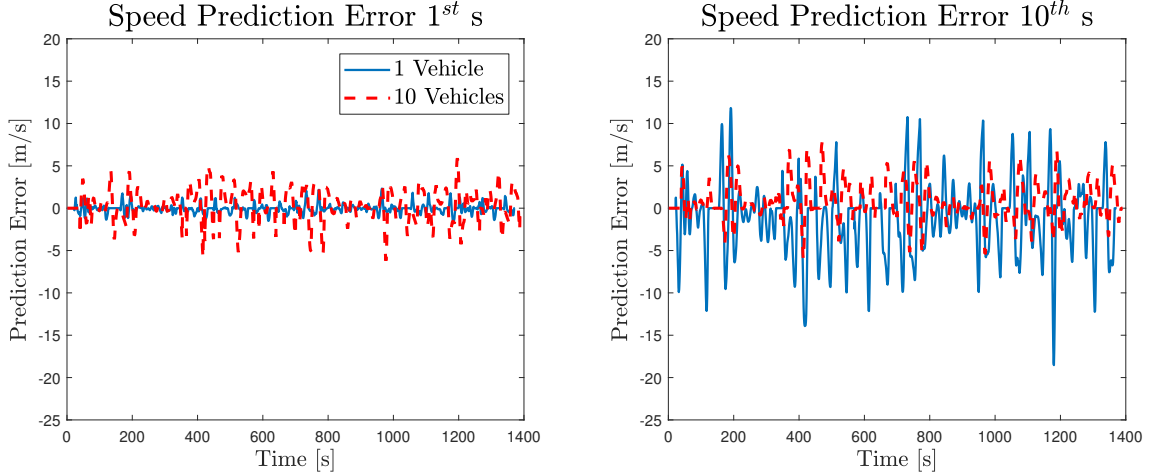


Figure 3.19: The speed prediction error in the 1st second and the 10th second are shown for 1 vehicle and 10 vehicles. Clearly, in the 1st second, the prediction error with 10 lead vehicles increases significantly, while the prediction error drops significantly in the 10th second.

in the horizon.

To resolve the prediction inaccuracy, the weighting function W_k was used, to weigh information of the leading vehicles differently. The weighting matrix can be defined as a diagonal positive definite matrix where the parameters α and γ can be defined by the user. The i^{th} diagonal element of the matrix can be defined as

$$(3.13) \quad \{W_k\}_i = \begin{cases} \exp\{\alpha \cdot (t_{k-h_k+i} - t_k)\} & \text{if } 1 \leq i \leq h_k \\ \exp\{-\gamma \cdot (t_{k,i-h_k})\} & \text{if } h_k + 1 \leq i \leq h_k + l_k. \end{cases}$$

The weighting matrix hence has two components, for the past information α and for the future information from the lead vehicles γ . Since it is an exponential function, information closer to the actual time step are weighed more than those further away in the past or the future and the values of both parameters are selected between 0 – 1. A parameter selection of 0 indicates that all information is used equally and a parameter selection of 1 indicates that current information is weighed the highest and future or past information significantly less.

The optimal weights can be found offline for a given objective, that is to find the optimal α and γ to minimize prediction errors. Since the given objective was to improve the predictions in the first second, using this optimization, it was found that the optimal α was always 1 and the optimal γ was close to 1. These results imply, that all the data of vehicles further in the lead should be almost ignored. Hence, to meet the objective of reducing the prediction error in the 1st second only

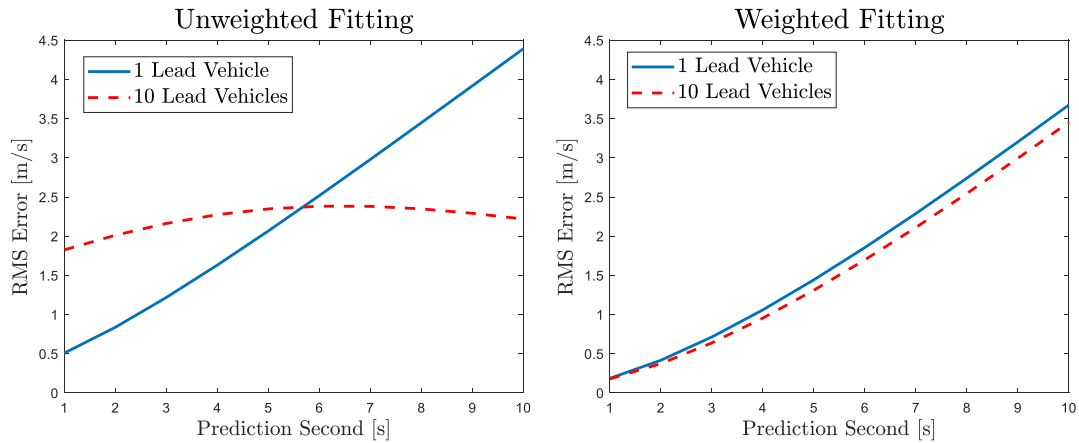


Figure 3.20: RMS Error at different prediction seconds for the unweighted and weighted cases

information of the immediate lead was used while the rest of the information from other vehicles further ahead were ignored. The RMS errors for the unweighted and weighted cases are shown in Fig. 3.20. For the unweighted cases, clearly the average error with 10 vehicles is lower than the average error with 1 vehicle as already shown before. But with the weighted case, the errors in prediction, with both 1 and 10 vehicles are almost the same for the prediction horizon. Predictably, this lead to similar predictions as with just one lead vehicle. To summarize it can be concluded that only the predicted information from the immediate lead is required for FE improvements using the MPC^a algorithm.

To further test the hypothesis of of the 1st second prediction being most important, errors were artificially introduced in the prediction using an exponential function where an error is added based on the prediction second. The resulting prediction errors are shown in Fig. 3.21. Using this when the error bands are introduced in the left plot, such that the RMS error in the 1st second is lower, while the RMS error in the last second is the same as the baseline. The resulting error line is shown in solid blue in Fig. 3.21. The solid red line is the case, where the error in the 1st second is the same as the baseline, while the error in the final second is much lower. The FE improvement results are indicated on the plots and clearly the blue line with the smallest initial error has the best FE improvement of 3.2%. On the other hand, with

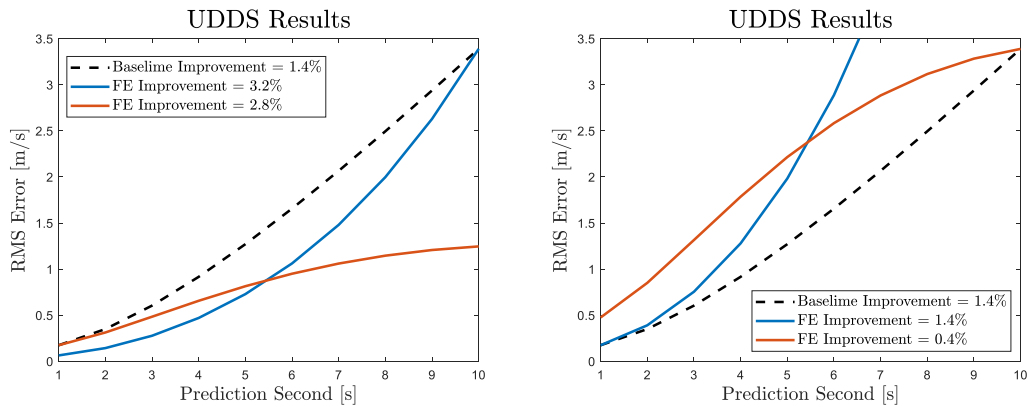


Figure 3.21: Artificially decreasing error in the first prediction second, still results in a lower FE than with decreasing error in the last prediction second. Similar results are shown with the reverse case

a significantly lower error further in the horizon, the red line only showed a 2.8% improvement.

Now in the right plots if again errors are artificially introduced, such that the error in the 1st second is the same as the baseline but much higher in the final second for the blue line, the resulting FE improvement is the exact same as the baseline. Hence, significantly higher errors further in the prediction horizon did not affect the FE. However, when errors were increased in the initial second of the red line case but kept the same for the final second, again, the case with the smaller initial error had a better optimization performance and a higher FE. Similar results for the US06 drive cycle are also plotted in Fig. 3.22 which showed similar behavior. The only difference was that the optimization was more sensitive to prediction errors further in the horizon, where in the left plot the red line performed much better than the baseline and in the right plot, the blue line did much worse than the baseline.

Since it has been concluded that the only information required is that of the hypothetical lead vehicle, other simpler prediction algorithms can also be employed to feed the necessary information to our MPC. A constant acceleration and a constant velocity simple prediction algorithms are also used. For the constant velocity case, it

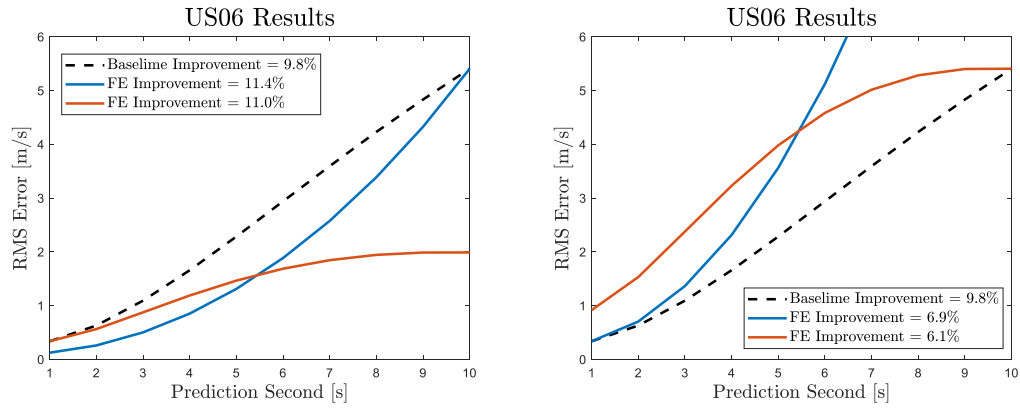


Figure 3.22: Artificially decreasing error in the first prediction second, still results in a lower FE than with decreasing error in the last prediction second. Similar results are shown with the reverse case

is assumed that the velocity at a particular second will be constant for the next 10 s. In the constant acceleration case, it is assumed that the current acceleration would be held constant over the 10 s prediction horizon. The results for a selected portion of the velocity trajectory is shown in Fig. 3.23. In this selected section, it appears that the constant velocity case was better for optimization than the constant acceleration one. However, from the overall results, using these algorithm, for the UDDS drive cycle it was found that the FE of the resulting velocity trajectory was worse than the baseline as reported in Table 3.2. And also, constant acceleration performed better than constant velocity. For other drive cycles, the constant acceleration did improve the FE over the baseline, however, it was always worse than the prediction algorithms.

Therefore, it can be stated that accurate predictions are important for the MPC algorithm and to increase the fuel economy. Hence, it makes sense that MPC^v with 1.5 s of perfect prediction was able to perform as well or better than with the prediction algorithms.

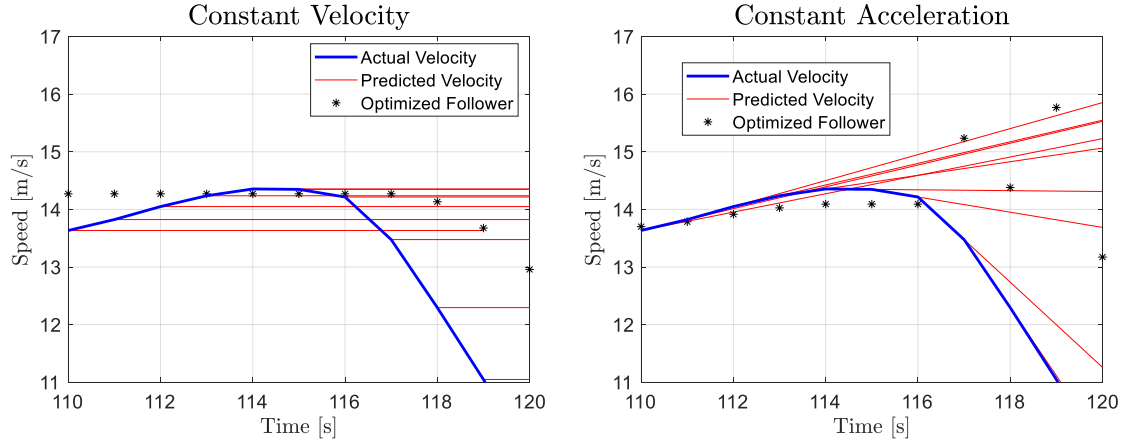


Figure 3.23: Constant velocity and constant acceleration velocity predictions for a section of the UDDS drive cycle

3.6 Discussion

The objective of this chapter was to find a controller that generates an optimal velocity trajectory such that the acceleration is minimized. Table 3.2 shows the improvements in FE for both the DP and MPC^v cases. Significant improvements were shown in FE for the Dynamic Programming case between 13.1% and 18.1% indicating a potential for high gain in FE for autonomous vehicles that enable real time optimization. Real-time implementation with MPC^v controllers shows improvements between 5.3% and 11.8%, for the shortest prediction horizon of 1.5 s. While obviously not performing as well as DP, MPC^v is able to improve upon the baseline. For very long prediction horizons of $N_p \geq 20$ s, MPC^a is able to match the DP results for all the given cycles simulated in ALPHA for the selected vehicle. We then utilized a velocity prediction algorithm to find the velocity of the hypothetical lead vehicle and then use the predicted constraints for MPC. The results show that a lower RMS error in prediction in the 1st second increased FE more than improved RMS error later in the horizon.

The model used in the optimal controller was deliberately kept as a simple point mass LTI acceleration model to generate the optimal velocity trajectory without con-

sidering the vehicle power train or engine dynamics. This was achieved by reducing the total accelerations and decelerations while maintaining an acceptable distance from the lead vehicle based on acceptable traffic patterns. This work shows that in meeting the simple acceleration objectives, FE can also be increased while following a hypothetical lead vehicle with a velocity profile associated with the federal test procedures [49]. An autonomous vehicle could have this FE objective along with other safety and traffic flow objectives. Tailoring the FE optimization by minimizing fuel consumption instead of the generic acceleration could result in even more benefits, given that not all accelerations are equally fuel consuming. This optimization will require engine and transmission data or models and

3.7 Conclusion

The results from this chapter shows the possibilities for improvement on present vehicle technologies through autonomous driving. Offline DP results achieve up to 17% improvement in FE. Simulation of various MPC formulations with a reasonable horizon length was able to achieve 12% improvement in FE. The velocity trajectories that achieved these improvements in autonomous vehicles were significantly different from the velocity profile of the standard cycles. The velocity difference was more than what is currently allowed by regulations. In light of this work, regulators need to reconsider the standard FE testing procedure that imposes a tight band around the velocity trace to encourage use of algorithms that increase FE, acceptable from both traffic and safety perspectives.

CHAPTER IV

Optimal Fuel Cost Function Evaluation

In the previous chapter, we explored one type of drive cycle optimization that involves velocity smoothing. However, when the vehicle controllers are free to drive their own velocities other optimization methods can also be employed. The optimization objective in this thesis is to drive an optimal velocity trajectory that minimizes fuel consumption. Two typical approaches to drive cycle optimization are velocity smoothing and tractive energy minimization. The former reduces accelerations and decelerations and hence it does not require information of vehicle parameters and resistance forces. On the other hand, the latter reduces tractive energy demand at the wheels of a vehicle. In this chapter, utilizing an experimentally validated full vehicle simulation software, we show that for conventional gasoline vehicles the lower energy velocity trajectory can consume as much fuel as the velocity smoothing case. This implies that the easily implementable, vehicle agnostic velocity smoothing optimization can be used for velocity optimization rather than the non-linear tractive energy minimization, which results in a pulse-and-glide trajectory.

4.1 Introduction

One approach to optimizing a drive cycle is velocity smoothing (reducing acceleration and deceleration) which improves passenger comfort by reducing jerk and in turn reduces fuel consumption, but this method does not guarantee an absolute minimum of fuel consumption [22, 34, 36]. This solution is attractive as it is independent of vehicle characteristics such as vehicle mass, road load and aerodynamic resistances. Moreover, the two state velocity model can be formulated as a simple linear model with quadratic costs, allowing for faster computation. In our previous chapter, we showed that this methodology can be effectively employed for online

implementation with Model Predictive Control. Using just 1.5s preview for some drive cycles we could get as much as 66% of the improvements from an entire drive cycle preview.

Another approach is tractive energy minimization; here the penalized variable is tractive or propulsion energy demand at the wheels, and hence is more closely related to fuel consumption. Such an approach should in theory reduce fuel consumption to beyond acceleration optimization [33, 76, 77]. In [54], a continuously variable transmission (CVT) was assumed and engine torque minimized. However, as the analytical solution in the same paper shows, the result of any energy optimization strategy is a pulse and glide velocity trace. Indeed, in this chapter similar results were shown for energy optimization. Any attempt at reducing the total energy demand at the wheels will result in a pulse and glide operation, where an initial heavy acceleration is followed by a steady speed or low rate deceleration gliding before finally coming to a stop. A fuel optimization, where the fueling rate is a linear function of propulsion power will also result in a similar optimized velocity trajectory.

In the literature reviewed for this thesis, the comparison is always between human and optimized driving, where improvements are so substantial that the gains derived by the correct choice of the optimization function become obscure. Note here that the reduction in fuel economy shown in this investigation can be as high as 18% for the optimized drive cycles over the standard US Environmental Protection Agency (EPA) drive cycles. However, between the two optimization techniques there is also a difference in fuel consumption. This difference comes out only in comparison between the two optimization problems with differing cost functions. Our work compares the two approaches for various engine sizes in a conventional powertrain and also against an all-electric powertrain, in time-varying position constrained simulations, to better understand the characteristics of each optimization strategy.

It is common practice in the literature to assume that a reduction in propulsion power or engine torque would yield a reduction in fuel consumption [77, 78, 55]. Translating vehicle power demand to an engine power demand is difficult for both offline and online optimization as complex powertrain dynamics cannot be accurately modeled without using a high fidelity software, which in turn increases computational time. Hence, optimal control designers rely on simpler vehicle models. Several

complex algorithms have been developed to minimize energy demand. Even when an engine fueling map is included, important powertrain dynamics such as gear shift strategy and torque converter clutch slipping are typically ignored. Hence the real engine operation region is unknown to the optimizer and a pseudo tractive energy minimization strategy is implemented.

This chapter, by utilizing full vehicle simulations from [3] shows that reduction in tractive energy does not guarantee a reduction in fueling rate. These results were shown to be valid across three different engine sizes in a conventional gasoline powertrain. This result is fairly well known in the powertrain community, but its implications on fuel efficient driving are not well understood. We show that velocity smoothing that has a higher tractive energy demand, is able to match if not improve fuel economy over tractive energy minimization.

We further utilize a simple powertrain model for direct minimization of fuel consumption but by manipulating the power input. In doing this we show that due to model mismatch, the resulting velocity trajectory has an even lower FE than the previous two optimizations. Clearly, a more complex powertrain model is required, however, such a model increased the number of states and due to the computational size made DP intractable.

This paper is organized as follows: Section 4.2 introduces the drive cycle optimization based on velocity smoothing and energy minimization. Section 4.3 explains the urban and highway cycles chosen for this study and their optimized cycles. In Section 4.4, a full vehicle simulation model used to evaluate fuel consumption is explained. Sections 4.5, 4.6, 4.7 and 4.8 provide detailed analysis of results obtained from the full vehicle simulation over the optimized drive cycles for a 1.6L downsized boosted engine, a further downsized engine, a full size 4.3L engine and an all-electric vehicle, respectively. The use of a vehicle powertrain model is discussed Section 4.9 in A summary discussion on the implications of these results is presented in Section 4.10, while the conclusions are noted in Section 4.11.

4.2 Optimal Control Problem

As mentioned earlier, improvements in velocity trajectory or driving patterns result in the reduction in fuel consumption for autonomous vehicles. The two optimization objectives considered here are velocity smoothing and tractive energy

minimization. The end objective of these velocity optimization approaches is to minimize fuel consumption, hence the resulting optimal velocity trajectory will be evaluated later in full vehicle simulations to determine individual fuel consumption. In this section, the two approaches to optimizing drive cycles including the models, cost-functions, constraints and optimization strategy used are provided in detail.

4.2.1 Velocity Smoothing by Acceleration and Deceleration Minimization

For velocity smoothing or minimizing the total acceleration and deceleration in the velocity profile, the same formulation as the previous chapter III is utilized. A simple point Linear Time-Invariant (LTI) model in [33] is adopted, with position (x_p) and velocity (x_v) as states and acceleration (a) as the only input:

$$(4.1a) \quad x_{p,k+1} = x_{p,k} + x_{v,k}T_s + 0.5a_kT_s^2$$

$$(4.1b) \quad x_{v,k+1} = x_{v,k} + a_kT_s$$

where $T_s = 1$ s is the sampling time. The optimization cost function chosen here is the square of acceleration and deceleration. The sum of the cost function is minimized, hence a smoother drive cycle is produced by minimizing the total changes in velocity. Define \mathbb{A} , \mathbb{X}_p and \mathbb{X}_v as polyhedral sets of constraints on inputs and states, respectively. Thus, the optimal control problem is formulated as

$$(4.2a) \quad \min_a \sum_{k=1}^{N_f-1} a_k^2$$

$$(4.2b) \quad \text{s.t. } a_k \in \mathbb{A}, x_p \in \mathbb{X}_p, x_v \in \mathbb{X}_v$$

where N_f is the final time-step, and constraints \mathbb{X}_p and \mathbb{X}_v are defined later in this section. The acceleration and deceleration constraints are time-invariant. For this paper, they have been derived from the EPA drive cycles to be $a^{\min} \equiv -6$ m/s², and $a^{\max} \equiv 6$ m/s². The same is true for the state of velocity x_v where $x_v^{\min} \equiv 0$ m/s, and $x_v^{\max} \equiv 40$ m/s. Constraints on the state of position x_p , however, are time varying as the position of the autonomous vehicle is determined by the position and velocity of a lead vehicle and hence a speed dependent gap. The cost function used above is a squared term, ensuring that larger accelerations and decelerations are

penalized more and hence it results in a smoother drive cycle. We shall now describe the second approach to drive cycle optimization.

4.2.2 Tractive Energy Minimization

For the second approach of tractive energy minimization, the total propulsion energy at the wheels is minimized. This optimization takes into account vehicle characteristics such as road load coefficients and vehicle mass. The optimization, however, does not take into account the internal powertrain dynamics such as the engine fuel map and gear selection strategy. Instead, it is assumed that a minimization of energy demand would lead to a reduction of fuel consumption which is a common assumption in the literature as previously mentioned in the introduction. To have the power demand at the wheels as the input, the acceleration term a in Eq. (5.2) is calculated by the net force on the vehicle, by Newton's Second Law of Motion. The external resistive forces on the vehicle, the rolling and the aerodynamic drag forces are modeled using the well known coast down parameters [79]. Detailed description about this coast down test is given in Section 4.4. The model and cost function for the second approach are given as follows:

$$(4.3a) \quad x_{p,k+1} = x_{p,k} + x_{v,k}T_s + 0.5 \frac{P_k - (A + Bx_{v,k} + Cx_{v,k}^2)x_{v,k}}{M} T_s^2$$

$$(4.3b) \quad x_{v,k+1} = x_{v,k} + \frac{P_k - (A + Bx_{v,k} + Cx_{v,k}^2)x_{v,k}}{M} T_s$$

where $P \in \mathbb{P}$ is the total power delivered at the wheels by the engine; A , B and C represent the road load coefficients determined from a vehicle coast down test [80]; and M is mass of the vehicle in kg . The total available power for propulsion and braking is limited as $P^{\min} \equiv -60 \text{ kW}$, and $P^{\max} \equiv 60 \text{ kW}$; these are the minimum and maximum power applied by the selected vehicle while executing the standard US06 drive cycle. The formulation for the optimization is given by,

$$(4.4a) \quad P_k^+ = \begin{cases} P_k & \text{if } P_k > 0 \\ 0 & \text{if } P_k \leq 0 \end{cases}$$

$$(4.4b) \quad \min_P \sum_{k=1}^{N_f-1} P_k^+$$

$$(4.4c) \quad \text{s.t. } P_k \in \mathbb{P}, x_p \in \mathbb{X}_p, x_v \in \mathbb{X}_v$$

Since the objective of this formulation is to minimize only the total tractive energy and is not concerned with the braking energy, the cost function only considers the positive input. In our previous work, we have shown that the optimal policy even with regenerative braking is to avoid braking as much as possible as there are losses in energy conversion [57]. This is unlike the previous case where both the positive and negative input, i.e. the acceleration and braking were minimized for a smooth velocity profile. Also, the cost function for the tractive energy minimization case does not use a squared term, unlike the velocity smoothing case. This is because, the attempt is to minimize the total energy demand at the wheels and instantaneous high power demand is acceptable. For acceleration optimization where the objective is velocity smoothing, the harsher acceleration and deceleration are penalized more by using a squared term.

The constraints from Section 3.2.2 are applied in this chapter as well. And in optimizing drive cycles, Dynamic Programming (DP) is considered in again in this study [51]. Specifically, the DP formulation for the drive cycle optimization is solved by using DPM function in [52].

4.3 Drive Cycle Optimization

In this section, the selected urban and highway drive cycles are described as well as the reasons for their selection. We will then discuss the resulting optimized velocity traces before switching to vehicle simulation results in the next section.

The urban drive cycle selected for this paper is the LA92 Dynamometer Driving Schedule, as it has higher maximum speed and maximum acceleration/deceleration as compared to the Urban Dynamometer Driving Schedule (UDDS). For similar reasons, the US06 drive cycle was selected as the highway cycle over the Highway Fuel Economy Driving Schedule (HWFET).

The selected drive cycles were optimized using the DP algorithm as mentioned before with two approaches: velocity smoothing and tractive energy minimization. A part of the resulting drive cycles are shown in Fig. 4.1 and they are explained as follows. The standard drive cycle obtained from human driving has frequent changes in velocity. On the other hand, the velocity smoothing algorithm produces a cycle with gentler propulsion and braking thus beneficial to passenger comfort.

The tractive energy minimization case, however, shows very interesting behavior.

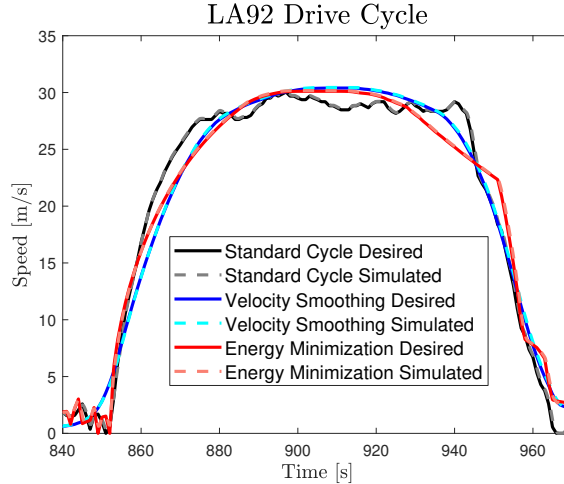


Figure 4.1: Velocity trajectories of the standard LA92 drive cycle with the velocity smoothing and tractive energy minimized trajectories. The solid lines show the desired velocity trajectory while the dashed lines show the actual trajectory traversed by the vehicle in ALPHA simulations. Clearly all velocity trajectories are reasonable and can be achieved in full vehicle simulations.

The initial acceleration is very harsh, followed by a very low power cruising phase which also features low rates of deceleration before finally decelerating to complete the hill¹. This result is very similar to pulse and glide [37] and previous analytical solutions have also predicted that pulse and glide results in least energy consumption [38]. Another attempt at engine torque minimization in [54] also resulted in a pulse and glide velocity profile. In effect, any attempt at tractive energy minimization results in a pulse and glide velocity profile.

4.4 Full Vehicle Simulation

To assess the impact of the optimized drive cycles on fuel consumption, a full vehicle simulation model is required. In this study, the Advanced Light-Duty Powertrain and Hybrid Analysis (ALPHA) tool was used. The ALPHA model was developed by the US EPA for full vehicle simulation over a drive cycle with the stated aim of evaluating the fuel economy of the vehicle. The ALPHA is a physics-based, forward-looking, detailed vehicle simulator built on MATLAB/Simulink environment.

The input to the model is any velocity trace in time and a driver system integrated within the model utilizes feedforward and feedback control schemes to maintain the desired speed. Detailed description of ALPHA is provided in [3]. This model has

¹A section of drive cycle featuring an acceleration, cruising and braking in sequence is referred to as a velocity hill for this thesis

shown to be robust over a range of very different drive cycles and has physics based models for different components, thus leading to a high confidence in the resulting fuel economy numbers. In published validation for different standard EPA drive cycles, the maximum reported error in fuel economy was 2% against experiments [81].

This simulation model is of a higher fidelity than the models used for optimization, as it takes into account the inertial and other delays in the engine and powertrain while executing a velocity change, thus ensuring that simulated vehicle velocity is realistic. Detailed engine, transmission and vehicle systems within the model provide a sophisticated and comprehensive method of estimating fuel efficiency as the modeled vehicle traverses a drive cycle.

The model also accounts for the rolling and aerodynamic resistances. This is accomplished by utilizing the well-known vehicle coast down test, where the vehicle is sped up to a high speed of 80 MPH and then put in neutral and allowed to slow down by the various road and aerodynamic drag forces [79]. The resulting velocity decrease over short time periods can be translated to an absorbed power using the kinetic energy equation. From there, the drag force at each velocity is found and fit using the linear least squares method to obtain the coefficients A , B , and C , of the following equation:

$$(4.5) \quad F = A + Bv + Cv^2$$

where, F is the drag force, and v the velocity at the force. This method is used to simulate the drag forces in a chassis dynamometer test as well. We use these experimentally determined parameters in Eq. (4.3) for calculating the resistive forces [80]. The software is simply evaluating the fuel required to maintain a given velocity trajectory.

For the drive cycles simulated in this thesis, the driver model in ALPHA was able to achieve desired speeds very accurately. The root mean squared (RMS) error between the desired and actual velocity traces for the velocity smoothed LA92 drive cycle was only 0.12 m/s and the mean absolute error (MAE) was only 0.09 m/s. For the tractive energy minimized cycle, the RMS error was 0.17 m/s and MAE was 0.08 m/s. Considering that the average speed for LA92 was 11.0 m/s, these small

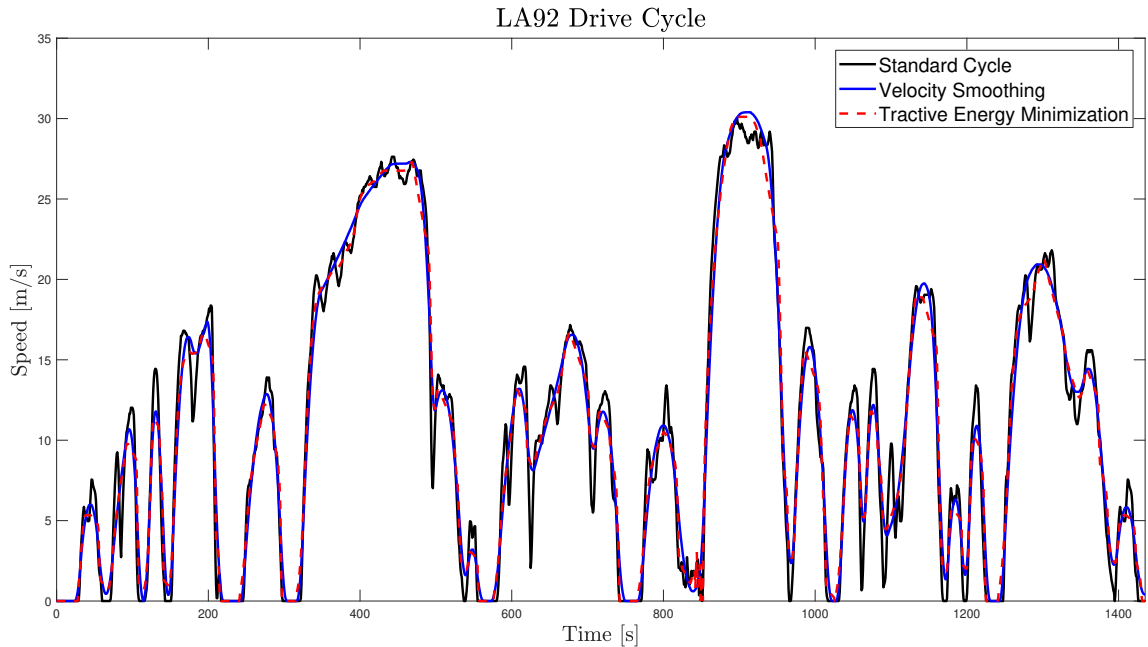


Figure 4.2: The velocity trajectories of the standard LA92 drive cycle along with the velocity smoothing and tractive energy minimized trajectories. Clearly the optimized trajectories are much smoother than the standard cycle and avoid frequent accelerations and decelerations.

errors show that ALPHA is able to simulate the velocity accurately and also that a vehicle is capable of traversing these optimized velocity traces. Fig. 4.1 shows the close following of the simulated velocity trajectories to the desired trajectory.

The results from vehicle simulations presented in Sections 4.5, 4.6, and 4.7 indicate that the drive cycle found from tractive energy optimization can in some cases lead to higher fuel consumption than that found through velocity smoothing. Previous comparisons were made between standard and optimized cycles, where these smaller differences were obscured by the significant reduction in fuel consumption. Hence the remainder of the chapter will focus on comparisons between the two optimized drive cycles. For comparisons with the standard cycles, readers are referred to chapter III. The findings of this work would aid future work on the choice of the cost function when the full fuel optimal computation cannot be performed in real time and a simplified metric might be needed. The results obtained in this chapter are computed through full vehicle simulations in a well validated ALPHA model. The simulation results are explained in detail in the following sections.

Table 4.1: LA 92 drive cycle optimization results

	Standard Cycle	Velocity Smoothing	Tractive Energy Minimization
Fuel Economy [MPG]	26.0	30.7	30.6
Tractive Energy [MJ]	9.93	8.03	7.48

4.5 Case Study I: Downsized Boosted Engine

In this section full vehicle simulation results and analysis are detailed for both urban and highway cycles. The baseline vehicle is a 2013 Ford Escape powered by a 1.6 L Ford EcoBoost engine. The low-displacement boosted engine is considered, as it is a commercially available advanced technology that delivers high efficiency in typical federal test procedures.

4.5.1 LA 92 Drive Cycle Optimization

The complete LA92 drive cycle with both the optimized cycles is shown in Fig. 4.2. Clearly both the optimized drive cycles are much smoother than the standard cycle as they are able to utilize the flexibility in position constraints to avoid frequent accelerations and decelerations. This smoothing of the drive cycle significantly reduces the fuel consumption of the vehicle as it traverses the velocity trajectory. As shown in Table 4.1, while the fuel economy of the standard LA92 cycle is 26.0 MPG, those for the velocity smoothing and tractive energy minimization trajectories are 30.7 MPG and 30.6 MPG, respectively. This produces almost an 18% increase in fuel economy, showing the significant benefits of optimized driving.

However, the small difference in fuel economy between the two optimized drive cycles is interesting. One would assume that a reduction in total tractive energy demand at the wheels would have resulted in a reduction of fuel consumption when compared with the plain velocity smoothed method. It turned out that, in a comparison between the two optimized cycles, a 6.9% reduction in total tractive energy at the wheels conversely results in a 0.3% increase in fuel economy.

To understand this phenomenon, a particular velocity hill from 850 – 950 s was studied closely. In Fig. 4.1, at 850 s, the power optimization case applies a 76% higher instantaneous propulsion power leading to an 80% increase in fuel consumption. However, for the entire event from 850 – 950 s, the overall propulsion energy is reduced by 5.6%. The corresponding fuel consumption reduces by only 2.1%. Clearly a decrease in total tractive energy demand did not lead to a correspondingly

LA92 Drive Cycle 850-950 s

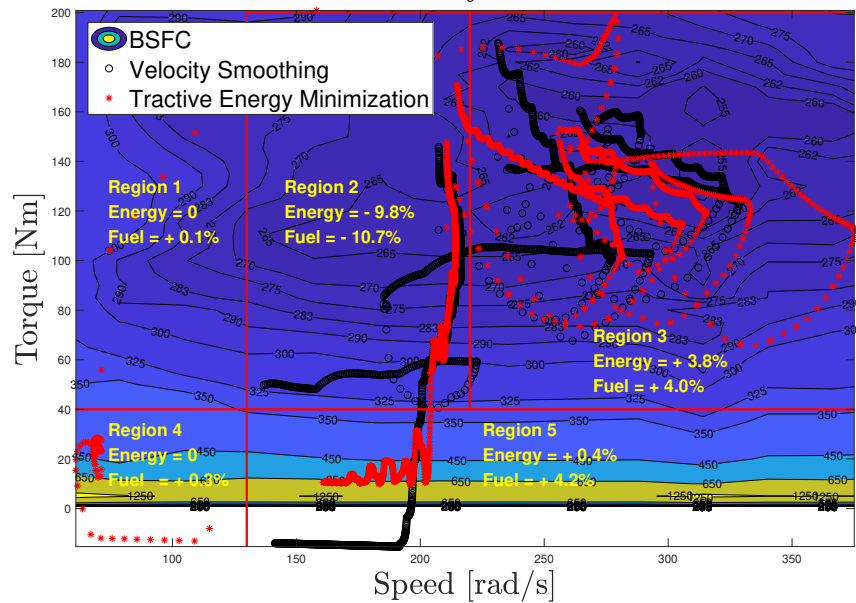


Figure 4.3: The engine operation points of the selected portion from 850 s to 950 s of the LA92 drive cycle is plotted on the BSFC map [4]. The solid red lines indicate the operating regions demarcated for residence analysis. A positive number indicates a gain in tractive energy optimization over velocity smoothing.

proportional decrease in fuel consumption.

The underlying cause for this difference can be explained by Fig. 4.3 which shows the engine operating points in the selected region. The reasons for smaller reduction in fuel consumption are not clear from operating points alone and so the map is divided into several regions, where the energy demand and fuel consumption within the confines of the region can be calculated. The regions are created as approximate zones of operation in different modes as follows:

1. Region 1: the low speed high power region which is only visited during transient fast accelerations.
2. Region 2: the approximate region of operation for the acceleration optimization case where the power demand is relatively smaller.
3. Region 3: the region with higher power potential than region 2, that is accessed by the higher power demand of the tractive energy optimization case.
4. Region 4: the region of operation for engine idling.
5. Region 5: the low torque high speed region, which is accessed while decelerating slowly, where the vehicle speed is high and the tractive power demand almost

negligible. When the vehicle decelerates at a higher rate, brakes have to be applied and there is no tractive power demand.

Within a region, a positive number indicates a higher energy demand or fuel consumption for the tractive energy minimization case while a negative number, a higher energy or fuel demand for the velocity smoothing case. In Region 2, velocity smoothing is more active and demands a 9.8% higher total energy supplied by a 10.7% higher fuel consumption. The high power demand of tractive energy minimization pushes the operating points into Region 3, where the tractive energy minimization case demands a 3.8% higher energy at a 4% higher fuel consumption. Between these two regions a net energy reduction of 6% leads to a net fuel consumption reduction of 6.7%. The higher reduction of fuel consumption is due to a greater engine efficiency as indicated by the brake-specific fuel consumption (BSFC) map in region 3 as compared to Region 2. The gains between Region 2 and 3 are as expected for tractive energy minimization due to the pulse and glide strategy.

The overall reduced fuel efficiency gain can be understood from operation in Region 5. Here a 0.4% increase in energy consumption leads to a 4.2% increase in fuel consumption for the tractive energy minimization case. In this region a small increase in energy demand causes a very large increase in fuel consumption as the operating region is extremely inefficient. The reason for operating in this region is explained by Fig. 4.4. At about 925 s, the vehicle starts decelerating in the traditional ‘glide’ portion of the pulse and glide strategy, and the tractive power demand is almost zero. However, at this high speed cruising, the tractive energy minimization case reduces speed at a lower rate of deceleration than the velocity smoothing case. The low rate of deceleration still has a very small positive tractive power demand. Due to the high speeds, this demand can only be met by operating in the highly inefficient region 5 of Fig. 4.3.

It must be noted that any energy minimization algorithm would result in almost a pulse and glide like operation. Hence the resulting velocity trace would contain some form of gliding, which in this case is the velocity segment of low power cruising, where a slight positive engine torque is required to propel the vehicle. However, this slight positive power demand leads to significant increase in fuel consumption due to the engine inefficiencies.

Broadening the analysis from the selected region to the entire LA92 drive cycle,

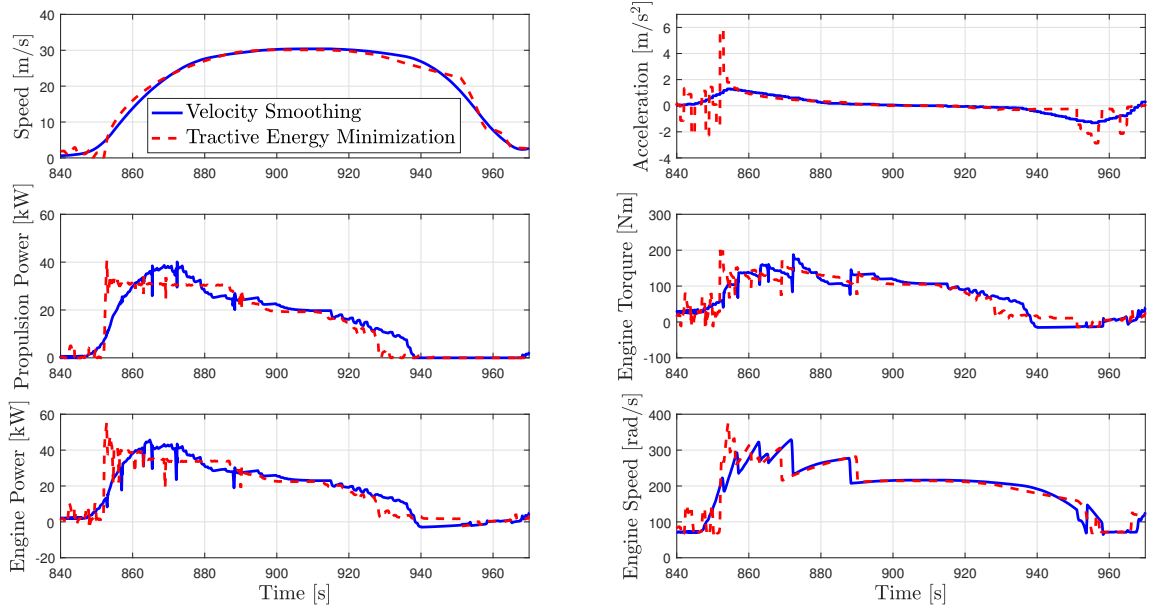


Figure 4.4: The vehicle velocity and acceleration are plotted for the selected portion of the LA92 drive cycle from 840 – 970 s. The tractive power at the wheels and the engine power are also shown. During the phase of low rate of deceleration, the engine is either idling or providing limited power. The plots for engine torque and engine speed show that at these points, the engine operates at high speed and low torque which is highly inefficient.

the pulse and glide trace for tractive energy minimization is seen for all velocity hills. This concurs with the results from literature mentioned before. To show the impact of the low power cruising, the drive cycle was divided into 5 modes based on the acceleration and power demand of the vehicle as shown in Table 4.2.

1. Acceleration: The mode of acceleration encompasses regions where vehicle acceleration as well as vehicle power demand are greater than zero.
2. Deceleration: Similarly for deceleration, it is the cases where both the acceleration as well as vehicle power are less than zero.
3. Low Rates Deceleration: These are the points where the acceleration is less than zero but the vehicle power demand is zero or higher. In these cases, even though the vehicle is decelerating, a slight torque is applied in the engine to maintain the required slowly decreasing velocity.
4. Inertial Acceleration: The inertial acceleration region is the short durations where even though the vehicle power is negative, inertia maintains a positive acceleration.
5. Vehicle Idling: Finally the engine idling region is where both acceleration and power are equal to zero.

Table 4.2: Comparison between optimized drive cycles in different modes for LA92 and US06 drive cycles. US06 results are in parentheses.

Mode	Velocity Smoothing Fuel (g)	Energy Minimization Fuel (g)	Percentage Difference	Velocity Smoothing Energy (MJ)	Energy Minimization Energy (MJ)	Percentage Difference	Velocity Smoothing Time (s)	Energy Minimization Time (s)	Percentage Difference
Acceleration acceleration \geq 0 vehicle power $>$ 0	751.12 (605.61)	680.60 (541.88)	-7.7 (-8.0)	7.44 (6.87)	6.73 (6.15)	-8.9 (-8.1)	736.1 (343.58)	648.42 (295.42)	-6.1 (-3.3)
Deceleration acceleration \leq 0 vehicle power \leq 0	73.37 (11.35)	80.33 (19.45)	0.7 (1.0)	N/A	N/A	N/A	529.98 (124.54)	411.14 (102.26)	-8.2 (-1.6)
Low Rate Deceleration acceleration $<$ 0 vehicle power \geq 0	78.00 (178.53)	123.59 (221.16)	5.0 (5.3)	0.59 (1.99)	0.75 (2.34)	2.0 (3.9)	124.98 (122.50)	239.08 (178.84)	7.9 (3.9)
Inertial Acceleration acceleration $>$ 0 vehicle power \leq 0	2.92 (0.77)	1.00 (0.13)	-0.2 (-0.1)	N/A	N/A	N/A	13.66 (3.62)	5.12 (0.68)	-0.6 (-0.2)
Vehicle Idling acceleration=0 vehicle power=0	6.78 (1.94)	28.44 (5.56)	2.4 (0.5)	N/A	N/A	N/A	35.32 (10.80)	136.28 (27.84)	7.0 (1.2)
Total	912.19 (798.20)	913.96 (788.18)	0.2 (-1.3)	8.03 (8.86)	7.48 (8.49)	-6.9 (-4.2)	1440 (605.04)	1440 (605.04)	0.0 (0.0)

From Table 4.2, it is clear that during acceleration the energy optimization case demands 8.9% less tractive energy, which translates to a 7.7% reduction in fuel consumption. On the other hand during low rates of deceleration, the energy optimization case demands only 2.0% more power but due to the inefficient engine operating regions where this power comes from, the increase in fuel consumption is 5.0%. Another major contributor to the increased fuel consumption is the engine idling mode. Here the energy minimization case spends 7% more time, resulting in 2.4% higher fuel consumption.

The above analysis explains for the entire drive cycle, that the presence of these gliding regions increases fuel consumption substantially for slightly higher energy demand and thus lower the overall fuel economy of the energy optimization case. This difference in fuel consumption is significant only in the comparison between the two optimized drive cycles. In case of the standard cycle the difference in fuel economy is 18% and hence the increased fuel consumption at inefficient regions gets obscured.

4.5.2 US06 Drive Cycle Optimization

The standard and optimized US06 drive cycles are shown in Fig. 4.5. For the US06, the optimized cycles showed a 17% improvement over the standard cycle. However, in this case, the energy minimized drive cycle had a better fuel economy than the velocity smoothed one. Over the US06 drive cycle, the tractive energy demand was reduced by 4.2% and the fuel economy by 1.4% as shown in Table 4.3. The interesting results were found in shorter sections of the drive cycles demarcated by the solid vertical lines in Fig. 4.5. In the first section from 0s to 131s the energy

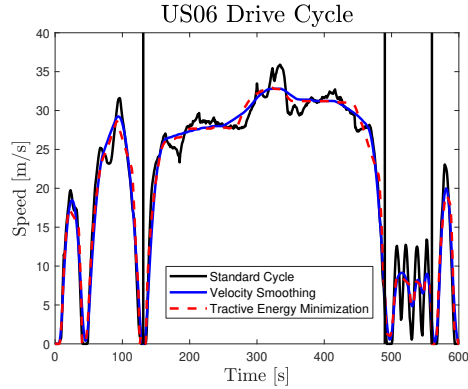


Figure 4.5: Velocity traces for the standard and optimized US06 drive cycles. As expected for the energy minimization cycle, higher rates of acceleration, long periods of low deceleration cruising and short high deceleration are observed.

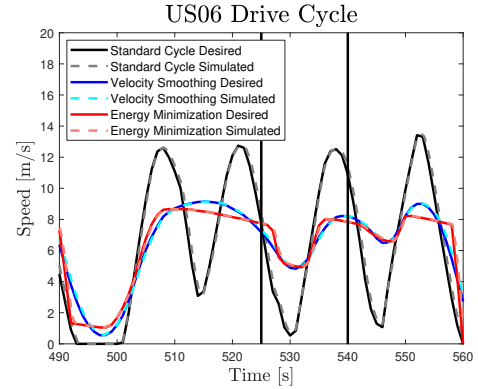


Figure 4.6: Velocity traces for the selected portions of the standard and optimized US06 drive cycles and the ALPHA simulated velocities. The three time periods of 490 – 525 s, 525 – 540 s and 540 – 560 s are demarcated in the plot.

Table 4.3: US06 Drive Cycle optimization results

	Standard Cycle	Acceleration Minimization	Tractive Energy Minimization
Fuel Economy [MPG]	24.4	28.5	28.9
Tractive Energy [MJ]	9.96	8.86	8.49

demand was reduced by 11.1% but the fuel by only 3.5%. In the second section from 131 s to 490 s the total energy demand decreased by only 1.9% and the corresponding fuel consumption by 0.6%. The most important case was the last section where even though the total power demand reduced by a significant 18.1% the fuel consumption increased by 0.2%.

To illustrate the difference between minimizing tractive energy and minimizing fuel, three consecutive parts of the US06 drive cycle are chosen as 490 – 525 s, 525 – 540 s and 540 – 560 s. The results for each of the parts are presented in Table 4.4. Interestingly, in the first case, a reduction in energy demand leads to an increase in fuel consumption; in the second case, a similar reduction in energy leads to a slight reduction in fuel consumption; finally for the third case, a significant reduction in energy demand does not lead to a proportional reduction in fuel consumption.

The difference in results is explained in Fig. 4.7, where the engine map is divided into 10 equally spaced grids. For reference, regions similar to the ones in Fig. 4.3 are also demarcated. The difference in energy demand as well as fuel consumption between velocity smoothing and tractive energy minimization are shown in each of those grids as squares and circles respectively.

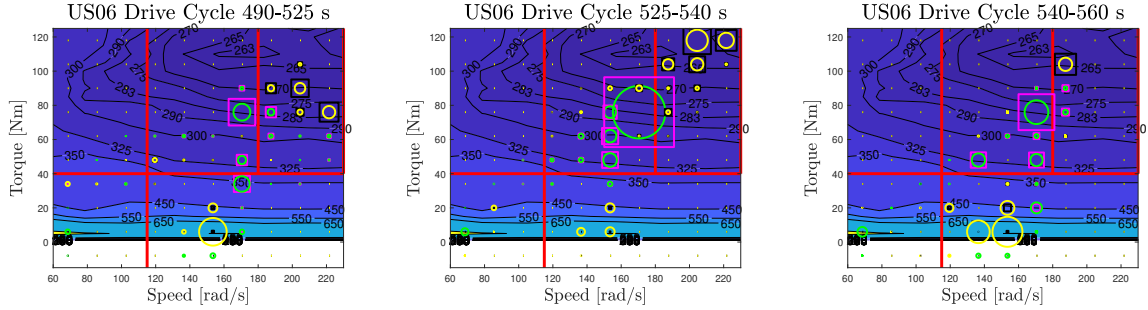


Figure 4.7:

Three consecutive parts of US06 drive cycle with the operating regions demarcated. A pink square and a green circle shows a higher energy and fuel demand respectively for the velocity smoothing case, while a black square and a yellow circle shows a higher energy and fuel demand respectively for the tractive energy minimization case. The size of the square and circle are proportional to the percentage gain over the other drive cycle.

1. The width of a square is proportional to the percent difference in energy demand in that grid. A pink square indicates a higher energy demand for the velocity smoothing case while a black square indicates a higher energy demand for the energy optimization case.
2. The radius of a circle is proportional to the percent difference in fuel consumed in that grid. A green circle indicates a higher fuel consumption for the velocity smoothing case while a yellow circle a higher fuel consumption for the energy optimization case. Different colors are necessary to show positive and negative differences.

Clearly in all cases Region 5 is where all the gains from the tractive energy minimization are lost. The tiny black dot indicates a slightly higher power demand and large concentric yellow circle shows the much higher fuel consumed. The length of operation in the high speed low torque zone dictates the increase in fuel consumption and can explain the contradictory results of the three selected parts. For all three selected cases the continued operation in the low torque high speed domain can be clearly seen in Fig. 4.7 with black dots indicating more power sought in those regions by the energy optimization case. This occurs when the vehicle velocity is decreasing at a very low rate of deceleration between 505 – 525 s, 535 – 540 s and 550 – 555 s. The elevated fuel consumption based on the length of operation in these low efficiency regions reduces all gains made from lowered energy demands. Hence the non-linearity of the engine map plays a significant role in determining the overall fuel consumption.

Table 4.4: US06 Drive Cycle optimization results for selected 3 parts

	490 - 525 s	525 - 540 s	540 - 560 s
Fuel Economy Difference [%]	-2.3	0.97	2.3
Tractive Energy Difference [%]	12.1	12.0	36.8

4.6 Case Study II: Further Downsized Engine

In the previous section the optimized cycles were simulated for the baseline engine which was already a downsized boosted engine. However, the optimized drive cycles had a much lower power demand than the standard drive cycles. The maximum engine power demanded for a standard US06 drive cycle was 93.6 kW, while those for the velocity smoothed and energy minimization ones were 60.8 kW and 47.1 kW respectively. Clearly a smaller engine with lower peak power could be used to meet the demands of these optimized drive cycles.

Since the ALPHA model was built at the EPA to account for a range of engine loads, it also has a function that provides the capability to generate fuel consumption maps by varying the engine size. Details of the function are provided in [82], where it takes into account the changes in heat transfer, friction and knock sensitivity as an engine is downsized. The 1.6L Escape engine was downsized to 75% of the original maximum power and the drive traces simulated through ALPHA. With a smaller engine, and a reduced torque range, the difference in operation between the velocity smoothing and energy optimization velocity traces were studied.

It was found that between the two drive cycles at a same reduction of power, for the entire drive cycle the smaller engine showed a 2.3% decrease in fuel consumption as compared to 1.3% in the standard engine. The cause of the reduction in the energy minimization case was however, not from the absence of operation in the inefficient regions. In fact the reason was that at some acceleration events the smaller engine operated in more efficient regions.

In Fig. 4.8 the difference in vehicle speeds between velocity smoothing and energy minimization are shown. Engine operation regions for acceleration from 75 – 90 s are also plotted on the respective engine maps in Fig. 4.8. The plots clearly show that the smaller engine has a higher engine speed as compared to the standard engine for the power optimization case. The limited torque range for the smaller engine drives the operating region to a higher speed to generate the same amount of power. This forces the engine to operate in more efficient regions. The result does make sense

US06 Drive Cycle

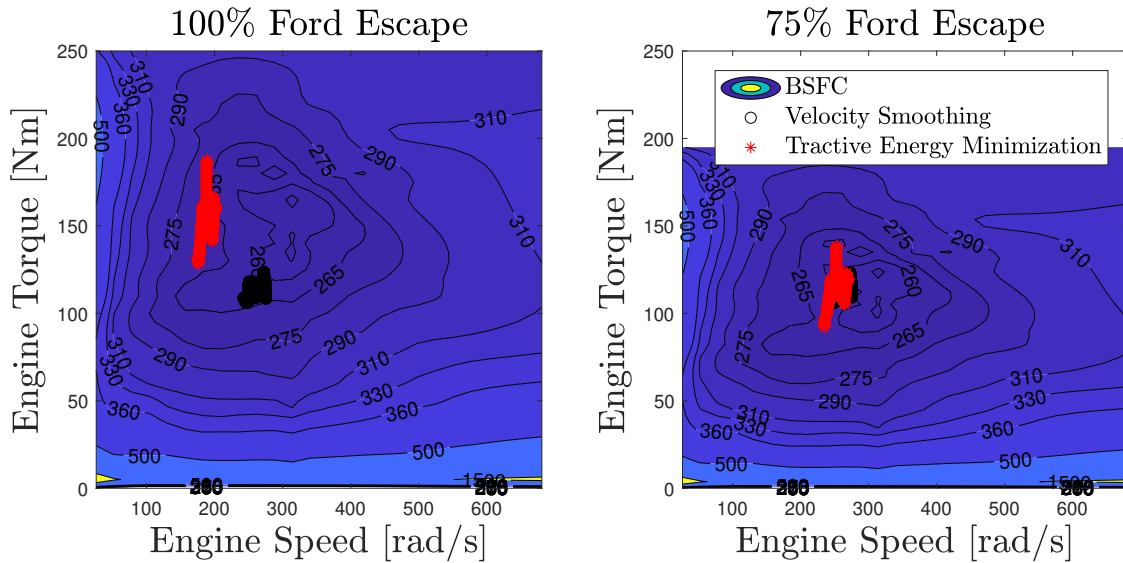
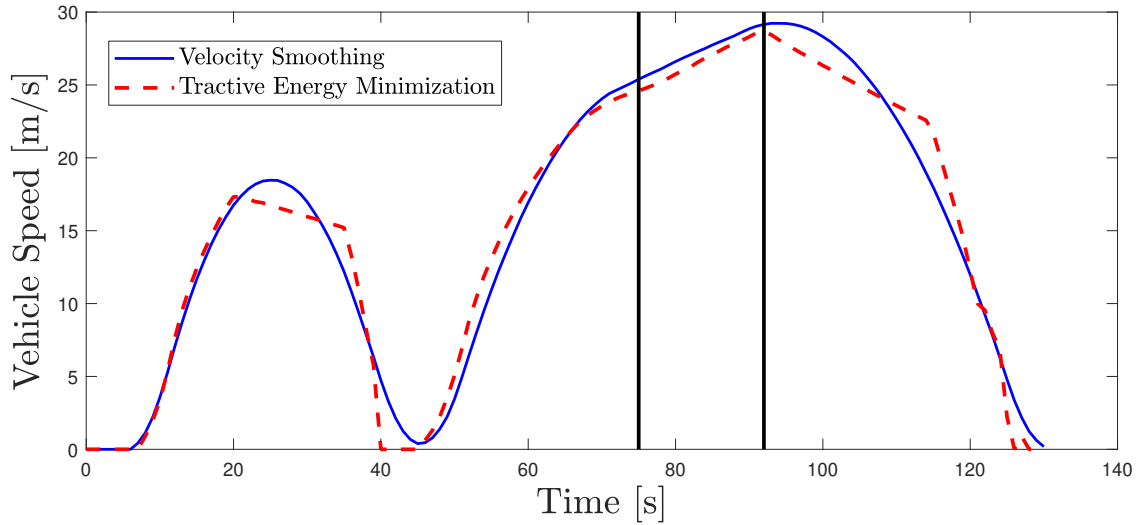


Figure 4.8: US06 drive cycle for a production 1.6L EcoBoost engine and a downsized version of the engine. For the downsized case, the available torque is reduced and to generate equivalent power, a higher engine speed is required. The full-size engine fuel maps are experimentally determined from [4].

as the smaller engine is able to meet the comparatively smaller peak power demand more efficiently. However, this approach of further downsizing the engine does not overcome operation in the inefficient regions during the low deceleration cruising that still occur and increase fuel consumption for the energy minimization case.

For the selected period of 0 – 130 s, the energy minimization case shows a 1.3% reduction in fuel consumption for the standard engine but a 2.3% reduction in fuel consumption for the smaller engine. Similar effects were observed in the period of 130–490 s a 1.8% reduction in power resulted in a 0.6% reduction in fuel consumption for a full size engine but a double or 1.2% reduction in the smaller engine. Again the reason for improvement was more efficient operation during the acceleration phase. The effect was particularly visible in the last 40 s of the drive cycle where the full engine showed a 5.9% reduction in fuel consumption but the small engine a significantly higher 9.6% reduction. However, it must be noted that the gain in fuel consumption is not proportional and the inefficient operation at low rates of deceleration remains for all cases.

After exploring the downsized engine in this section we shall now show simulation results for the full-size engine in Case Study III as it traverses the two optimized drive cycles.

4.7 Case Study III: Naturally Aspirated Full Size Engine

To understand whether the conclusions on tractive energy optimization were specific to turbo-charged engines or would hold for naturally aspirated ones as well, in this section a 4.3 L Chevrolet Silverado Ecotec engine map was used to run the optimized drive traces. This particular engine is used to power large Chevrolet pick-up trucks and does incorporate an aggressive deceleration fuel cut-off strategy.

It was interesting to observe that the aggressive cut-off actually affected the velocity smoothing case more positively than the energy minimization one. For the entire US06 drive cycle the total tractive energy demand reduced by 4.1% but the reduction in total fuel consumption was only 0.1%. As shown in Fig 4.9, the higher rates of deceleration allow for longer durations of fuel cut-off in the acceleration optimization case. On the other hand for power optimization, the low rates of deceleration that require very small amounts of engine power reduces the duration through which the fuel cut-off can be initiated, thus increasing fuel consumption. In the period shown

US06 Drive Cycle

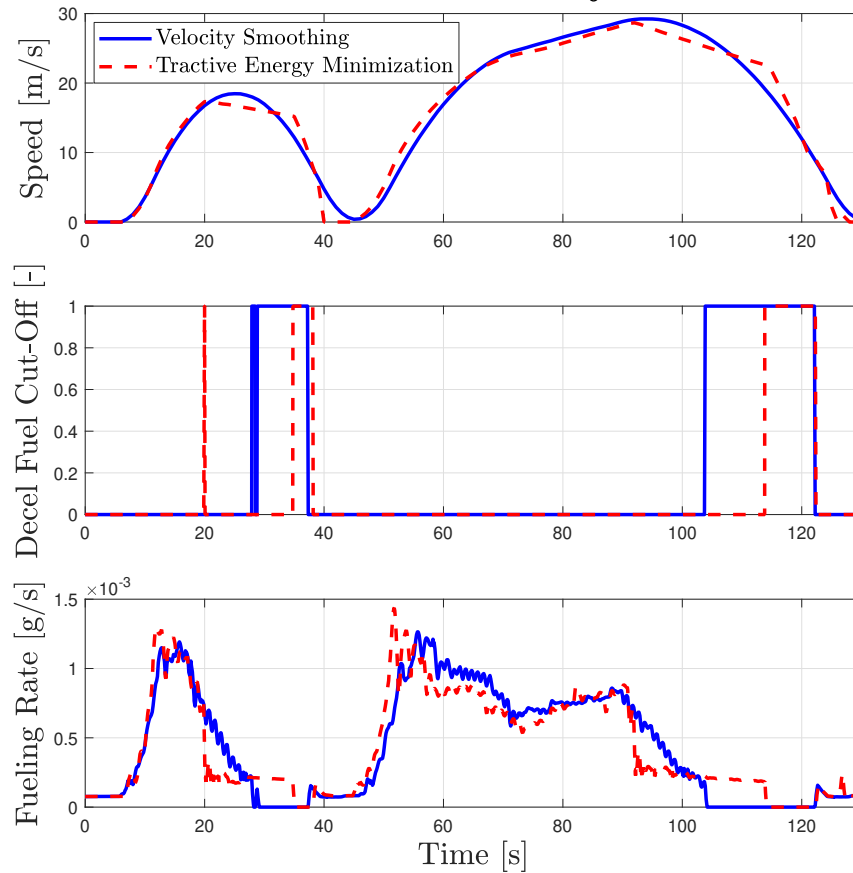


Figure 4.9: US06 drive cycle for a the 4.3L Chevrolet Ecotec engine. The low power cruising in the power optimization case reduces the cylinder deactivation time and hence increases the fuel consumption.

in Fig. 4.9, the fuel cut-off occurs for 19.3% of the time for velocity smoothing and only 7.8% of the time for energy minimization. Hence for that period, a reduction of only 0.2% is achieved in fuel consumption, even though the total energy required decreased by 10.8%.

Obviously, there was no explicit term for deceleration fuel cut-off in either of the optimization cases but the point of running these drive cycles with this technology is to highlight the several ways in which fuel consumption might not be proportional to energy demand. Any optimization to reduce fuel by minimizing energy demand has to take into account the effect of these technologies and how they change fuel consumption. Another important point is the low rate of deceleration that is the main culprit in increasing fuel consumption. While these cases require a very low amount of power to traverse, they disproportionately consume large amounts of fuel

to operate in these regions.

By disabling the fuel cut-off strategy for this large engine, the effect of only changes in the drive cycle could be studied. It was found that the decrease in fuel consumption for the entire drive cycle in the power optimization case was now 0.5% as compared to 0.1% with the cut-off enabled. The improvement can be attributed to a higher increase in fuel consumption in the acceleration optimization case with idle fuel consumption instead of a complete fuel cut-off. The corresponding increase in the energy minimization case was obviously smaller as the length of time fuel cut-off was engaged was less in this case.

The reason for much lower decrease in fuel consumption of 0.5% as compared to the 1.6L EcoBoost which showed a 1.3% decrease is during the period of 490 – 560 s. Recalling that this is the region with longest operation at the low torque - high speed range, it can be understood that the fueling rate is much higher for this large engine and it leads to significantly higher fuel consumption. An interesting technology that can be applied in this case would be cylinder deactivation which can be engaged if the desired engine torque is below 150 Nm and engine speeds are between 100 – 250 rad/s.

In the previous three sections, this paper covered the engine performance of three different engine sizes, encompassing almost all the engine displacements available commercially for light duty vehicles. The three case studies showed that energy minimization leads to a pulse and glide operation, and for conventional vehicles powered by an internal combustion engine, the glide portion operates in a highly inefficient region of engine operation consuming a disproportionately higher fuel thus lowering the overall fuel economy. While the above analysis hold true due to the fuel map of a conventional vehicle, for an all electric vehicle powered by only an electric motor should always show a reduction in energy consumption with a reduction in energy demand. This assumption was tested in the next section.

4.8 Case Study IV: Electric Vehicles

Since the issues with minimizing energy not leading to a minimization of fuel consumption were derived from the non linear fuel map and low power cruising causing the engine to operate in inefficient regions, electric vehicles were analyzed to understand their behavior. The electric motor efficiency map is much flatter and does not include enormous efficiency penalties at high speed and low torque

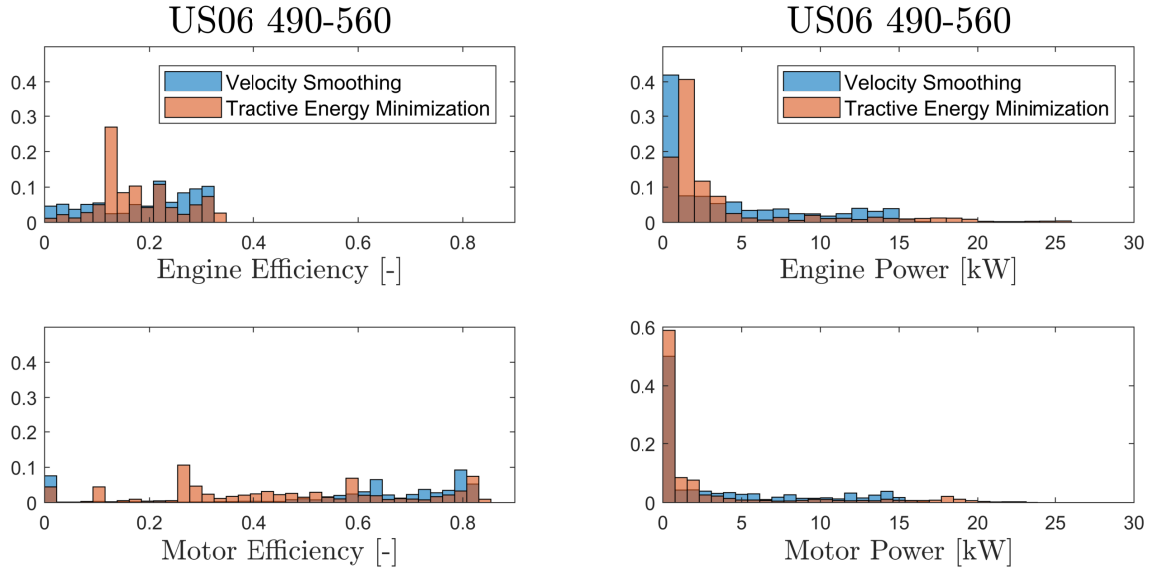


Figure 4.10: Distribution of efficiency of operating points and demanded power from both the conventional engine and the electric motor.

as compared to a conventional engine. This should mean a proportional gain for the power optimization case. On the other hand electric vehicles have regenerative braking which ensures that some of the lost energy is regained through braking. These effects are studied in this section. Simulations were carried out using the ALHPA model for a 2013 Tesla Model S.

From 0–130 s of the US06 drive cycle it was found that a 9.7% decrease in tractive energy was accompanied by a 9.0% decrease in total battery energy demand. As expected the battery discharge demand was 12% less indicating a greater gain in energy consumption than energy demand due to operation in more efficient regions. However, there was lesser battery charging in the power optimization case of -3.0% which lead to a net battery demand of 9.0%. Even though the drive cycles operated in the low torque high speed region, the slight change in efficiency did not decrease the overall gain in the energy minimization case.

The velocity smoothing case did have a much higher braking power demand, and some of this was regained by the charging of the battery. But the regained charge was much less as compared to the discharge during propulsion, leading to a net gain for the energy minimization case. In all cases studied it was found that the battery energy regained in braking was not proportional to the braking energy. The more aggressive braking in the power optimization case was able to regain more energy

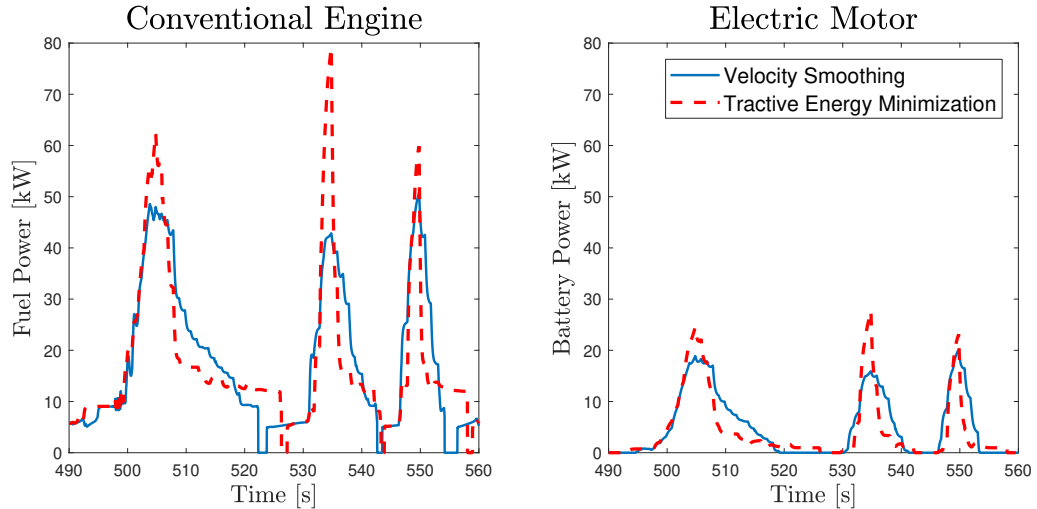


Figure 4.11: Equivalent power in fuel and battery as supplied to the engine and motor respectively for the selected portion of the US06 drive cycle. The fuel power is much higher due to the maximum 35% efficiency in a conventional engine.

through regen braking than the acceleration optimization case even though the total braking energy was much larger for the latter.

Figure 4.10 shows the distribution of operating points in engine and motor efficiency and the power demand from the engine and motor. Looking at the efficiency distribution it can be seen that both the engine and the motor operate for longer periods of time in less efficient regions for the power optimization case. However, to compare the efficiencies of a conventional engine to an electric motor, both have been normalized. As expected, the maximum engine efficiency is around 35% for the 1.6L EcoBoost, but the electric motor has a maximum efficiency of almost 90%. So while the shapes of distribution are very similar between the two, due to the much lower efficiency of the engine, the inefficient regions are far worse than the motor. This leads to a smaller increase in battery energy consumption for the motor.

In the case of the power demand, it can be seen that the conventional engine has a far higher demand for low power between 1–3 kW, than the electric motor where this demand is comparatively less. This discrepancy can be explained by the lack of gears in an electric vehicle, where the motor speed directly commands the engine speed without several transmission losses. In Fig. 4.11, the increased demand of fueling power as compared to the battery power for the 490–560 s of the US06 drive cycle is shown. The inefficiency of the engine forces the required fuel power to be much higher than the equivalent battery power. During the low speed deceleration and

idling it can be clearly seen that fuel power required is much higher. The maximum to idling fuel power ratio is 6.5. On the other hand, the electric motor is able to operate with much lower demands of battery power, proportional to the wheel power demand. The maximum to idling battery power ration is 12.9 indicating almost double the efficiency during the phases of low rate deceleration. Moreover, it is much easier for the motor to go to a zero power case than a conventional engine and a part of the braking energy can also be recovered.

For these reasons the electric vehicle showed a straightforward proportional decrease in battery energy demand for a decrease in wheel energy request on account of a energy minimized drive cycle. Some of these gains were overturned due to regen braking and energy regained in the velocity smoothing case owing to its substantially higher braking energy. Still, the more aggressive gains in the tractive energy minimization case was able to reduce the deficit, and in all cases the net battery energy consumed was always lower for energy minimization. This shows that the tractive energy minimization strategy works much better for an electric vehicle where a reduction in battery power consumption can be guaranteed unlike a conventional vehicle where this cannot be conclusively stated.

4.9 Fuel Minimization

Till now we have used a surrogate for minimizing the fuel consumption, instead of going through the vehicle powertrain and minimizing it directly. In Fig. 4.12 we analyzed the fuel economy for different cruising speeds, driving for 500 s at constant speed. The fuel economy and other results listed are only for the period that the vehicle is cruising. These simulations were again performed in the ALPHA model for a 2013 Ford Escape with a 1.6L EcoBoost Engine. Seven different speeds from 12 – 18 m/s were analyzed in simulations. The gear shift strategy, selected gear 4 for speeds between 12 – 14 m/s and gear 5 for the higher speeds from 16 – 18 m/s. The fuel economy results are expected and are listed for individual speed in the plot. And also shown are the constant power lines on the engine map.

From 12 – 14 m/s, all speeds are in gear 4 and occupy a lower torque and higher speed region. It is observed that as the speed increases the fuel economy reduces. This is explained by the fact that as the speed increases the power demand increases and the slight increase in efficiency cannot compensate for it. As the speed increased

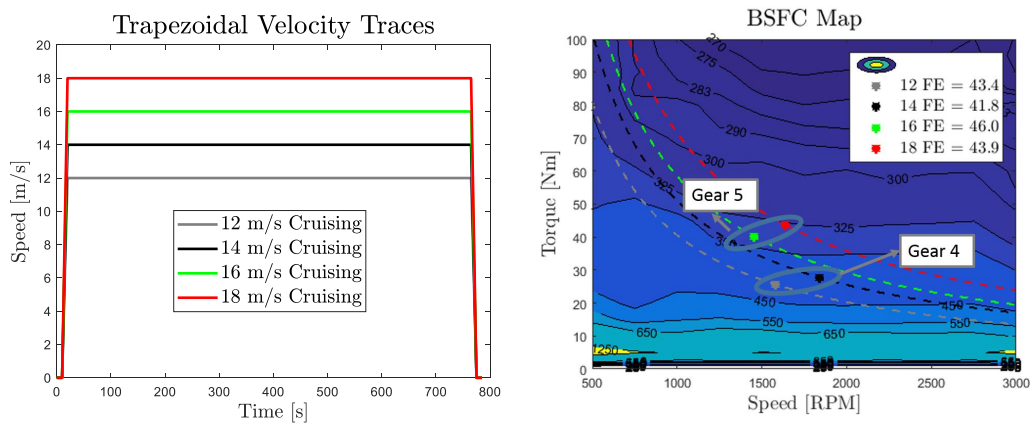


Figure 4.12: Trapezoidal velocity traces are shown with equal constant velocity cruising duration. On the right BSFC map, the engine operating point at the different constant velocity cruising and FE are shown.

further to 16 m/s the gear shift strategy increases the selected gear to gear 5 thus taking the engine operating point to a much more efficient region. This significantly improves fuel economy compared to 15 m/s results. Again with increasing speed the fuel economy reduces.

The point of this plot is to show that several factors contribute to the eventual fuel economy of the vehicle and also the region of engine operation. The goal is to go to a low speed and high torque region as the efficiency is higher here, as is clearly shown in the results above. By changing the calibration or gear shift strategy (perhaps modifying the powertrain) it could have been ensured that the simulator would select gear 4 for 15 m/s and operate the engine in the more efficient region. The number of gears also determine where the engine is operated.

To ensure that the engine is operated in the more efficient regions would be beyond the scope of simply the velocity planning algorithm. However, with the preview and use of DP in optimizing the velocity planning, the future engine power demand can modulated such that the engine operates only at its highest efficiency. From the results in Fig. 4.12, it is clear that constant cruising at 18 m/s actually produces a better fuel economy than constant cruising at 12 m/s, therefore if this information

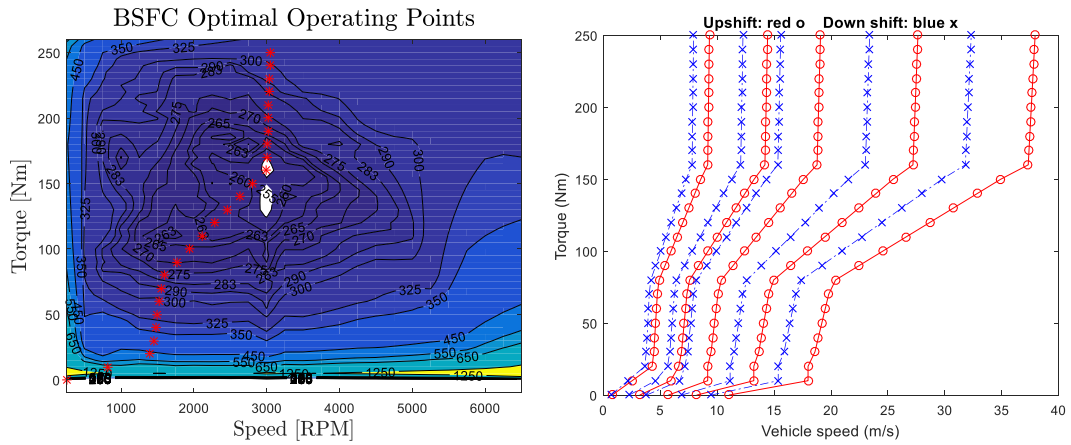


Figure 4.13: Gear shifting strategy with hysteresis based on the optimal BSFC operating points

was available to the optimizer, it would be able to meet the position constraints better and also further reduce the fuel economy.

For this process, we utilized a vehicle model using a linear correlation between the power demand at the wheels and the power demand in the engine. This simple correlation has been used in the literature before. We already know the power demand at the wheels P_k from equation 4.3. The engine power can be determined from equation 4.6, where the parameters a_1 and a_2 are determined from Linear Least Squares fitting of ALPHA results. The parameter values are listed in Table 4.9.

$$(4.6a) \quad P_{eng,k} = a_1 \times P_k + a_2$$

Since we know the vehicle speed and engine power, we can now determine the engine speed and torque by equation 4.7.

$$(4.7a) \quad \omega_{eng,k} = \frac{x_{v,k} \times GR_{fd} \times GR_{gear,k}}{r_{tire}}$$

$$(4.7b) \quad \tau_{eng,k} = \frac{P_{eng,k}}{\omega_{eng,k}}$$

where, GR_{fd} is the final drive gear ratio, listed in Table 4.9, $GR_{gear,k}$ is the selected gear ratio at time k and r_{tire} the radius of the vehicle's tire also listed in

Table 4.5: Vehicle Model Parameters

Parameter	Value
a_1	1.09×10^{-3}
$a_2 [W]$	1.724
GR_{fd}	3.21
$r_{tire} [m]$	0.337

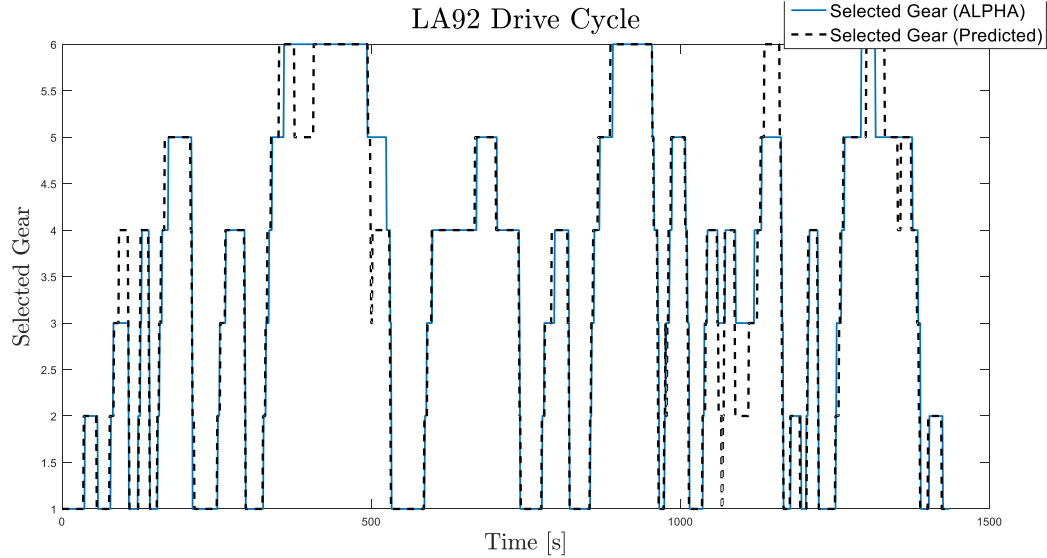


Figure 4.14: Validation of gear map with ALPHA results

Table.4.9. Now the engine speed ω_{eng} and engine torque τ_{eng} are computed. The fueling rate in the engine is determined by the fuel map that we appropriated from the ALPHA model. This formulation requires the continuous computation of the gear, which has to be selected at every time step. A simple gear map as with hysteresis, as shown in Fig. 4.13 was used to determine upshifts and downshifts. Based on the optimal operating points a shift strategy was devised, that matched fairly well with the ALPHA results. The gear map validation is shown in Fig. 4.14 where even for a highly variable drive cycle like the LA92, our gear map was able to select the correct gear for most cases.

Using the more complex vehicle model added an extra state of gear into the optimization which significantly increases the computation time in DP. This increase was so significant that optimizing for only the last 100 s of the US06 drive cycle required 6 hours. This is clearly infeasible for actual drive cycles like the UDDS which are 1372 s long. What was interesting, was that even for this short optimization, based

on the vehicle model in DP, the resulting FE was 22.5 MPG. However, when the optimized trajectory was simulated in ALPHA, the resulting FE was only 19.8 MPG. This implies that our simple vehicle model was not able to capture the powertrain dynamics and resulted in an FE that was 12% lower in full vehicle simulation.

Moreover, for the last 120 s of the US06 drive cycle, the FE from velocity smoothing and tractive energy minimization are 20.5 MPG 20.9 MPG respectively. So not only did the inaccurate vehicle model reduce FE in optimization, it reduced it below the other simpler optimizations. Inaccuracy in the model causes DP to over predict the improvements. In reality, the FE results from ALPHA simulations are worse than the FE found from previous optimizations. Hence, if full vehicle optimization is to be done, then a more accurate model should be used. However, with an increase in states, the vehicle model was already very complex and computation time for a 120 s optimization was over 6 hours.

For the complete powertrain, a schematic is shown in Fig. 4.15 to determine the fueling rate from the current and desired speed. There are two prongs to this approach, one to find the engine torque and the second to determine the engine speed. For the torque, based on the difference between the current and desired speed, a driver model determines the required driver torque. Then from the driver torque, a pedal map is used to compute the pedal torque which can be translated to the desired engine torque. For the engine speed, the current speed is converted to the synchronizer speed from the final drive gear ratio and the turbine speed based on the synchronizer slipping. Then using the equations of the torque converter clutch, based on whether they are engaged or disengaged, the impeller or the engine speed can be determined. On the other side, the commanded engine torque translated through the powertrain on to the wheels, the force on the wheels and hence the acceleration can be computed for the vehicle speed in the next time step.

This full vehicle model increased the number of states to 6 with position, velocity, selected gear, the torque converter clutch state, impeller and synchronizer speed. In offline simulation, this model matched the ALPHA results very well, showing only a 0.7% error in total fuel consumption for the US06 drive cycle and 0.6% error for the LA92 drive cycle. However, the complexity was too much for optimization and computation time made this problem intractable. Clearly, the simplest velocity smoothing algorithm can deliver as good or even better results than the more complex

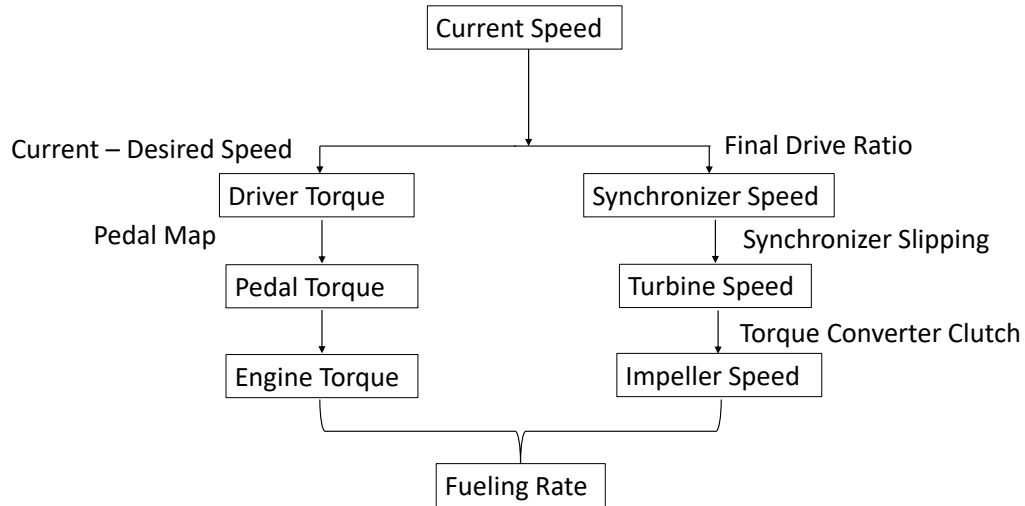


Figure 4.15: Full vehicle model schematic

optimizations with detailed vehicle models.

4.10 Discussion

From the literature review, it is clear that the fuel minimization problem is addressed, either as a simple energy minimization at the wheels or by using a linear function of wheel power that estimates fuel. In both cases, the energy at the wheel is minimized. It was analytically shown in [54] that such minimization results in a pulse and glide velocity trajectory. Therefore, it is not surprising that whatever the assumed model might be, most attempts at velocity manipulation for minimum fuel consumption lead to a pulse and glide velocity trajectory. Similarly, in this chapter, minimizing the power demand at the wheels, resulted in a pulse and glide velocity trajectory. This result is consistent with those presented in the literature.

The main contribution of this chapter is twofold. First, the fuel economy improvement achieved by the two optimization approaches is compared and analyzed rigorously. Second, the effectiveness of the approaches for different powertrain options, i.e., downsized turbo-charged engine, further downsized engine, naturally aspirated engine, and all-electric vehicles is investigated. The comparison in this paper reveals that velocity smoothing works as well, or better in some cases than tractive energy minimization for conventional gasoline vehicles. A well-validated ALPHA model is

used to evaluate the fuel economy of both drive cycles. The detailed comparative analysis of the resulting velocities as shown in Fig. 4.3 clearly reveals the differences. As an optimization problem, the tractive energy minimization case with the cost function as the tractive energy demanded at the wheels, reduces it over the velocity smoothing case. However, a similar reduction of fuel consumption reduction was not found. Utilizing ALPHA's detailed simulation, it was shown that during the gliding phase, to maintain the optimal velocity, a slightly higher energy demand led to a significantly higher fuel consumption. This was due to the engine efficiency at the high speed low torque operating points which wipes out all the gains from the lower energy demand.

The significance of this result, is that a simple optimal control problem with a linear model and quadratic costs could deliver comparable results to a more complex nonlinear optimization requiring more computational time and power. For instance, the cloud based DP algorithm in [76] can be replaced by a quadratic programming solver that can be implemented online; or the nonlinear function in the formulation used in [77] can be replaced by a linear function to reduce the computational burden. This method would significantly simplify the optimal control problem in [78].

Further, the resulting pulse and glide profile can be unsatisfactory from a passenger comfort point of view. Hence, in the literature, implementation of pulse and glide has to manipulate the optimal velocity to account for passenger comfort [54]. The switching in [38] can be implicitly removed in the velocity smoothing formulation delivering superior smoothness. Therefore, it is much easier to persuade customers to implement the velocity smoothing algorithm that does both, improve passenger comfort without compromising on fuel economy. It should be noted that these results are only valid in a conventional gasoline vehicle and as shown are not valid for an electric vehicle.

4.11 Conclusion

From the initial attempt at minimizing fuel consumption by minimization of energy demand at the wheels, this work has shown that in some cases the assumption might not hold. The energy minimization algorithm, decreased the total energy by initially applying a high power at the start of any velocity hill and then moving to a low power cruising mode. This ensured a lesser energy demand than the velocity

smoothing case under all circumstances. However, the presence of the low power cruising part forced the engine to operate in an inefficient low torque - high speed region, significantly increasing fuel consumption for a slight demand of power. This behavior was observed in a larger as well as smaller engine. Additional technologies such as deceleration fuel cut-off reduced the gains from energy minimization further. Finally in a comparison with electric vehicles, owing to the more efficient electric motor and a lack of gears, it was shown that reducing energy demand at the wheels guaranteed a decrease in battery energy consumption.

From this work it is clear that the easily solvable velocity smoothing algorithm, which does not require any vehicle information and is more conducive for passenger comfort can deliver almost the same improvements as a more complex energy minimization algorithm. Hence, in a conventional vehicle the engine operating region has to be taken into account while reducing propulsion power to result in a proportional decrease in fuel consumption.

CHAPTER V

Electric Vehicle Analysis

Eco-driving via velocity trajectory optimization and regenerative braking can both reduce the energy demand of an electric vehicle (EV). However, eco-driving can save more energy than can be recovered via regenerative braking due to the total roundtrip efficiency of the motor/generator. The optimal velocity trajectory would always avoid braking if the constraints allow. This chapter initially analyzes the battery energy consumption results for the velocity smoothed cycles to show a battery range extension of over 15%. Further, this chapter investigates energy optimal velocity profiles for various electric ground vehicles over varying road grades, where the autonomous vehicles can adjust their velocity trajectory. The optimal velocity trajectories, numerically obtained from Dynamic Programming, significantly reduce the total energy demand by the motor compared to a constant cruising operation for the same travel distance and time. The optimized velocity trajectories, thus increase vehicle range without a change in battery size or trip time.

5.1 Introduction

The analysis carried out for all the previous chapters was for a conventional vehicle with an advanced downsized boosted engine. All fuel economy improvements shown were for the particular vehicle and engine. However, velocity smoothing in essence reduces the energy demand from a power source. This works well for a conventional vehicle where the energy demand from the engine and hence the fuel consumption gets significantly lowered. The same principle can also be applied for electric vehicles too by reducing the energy demand from the battery. In reducing the battery energy demand, the same distance can be covered with by consuming less battery charge and thus increase the range of the vehicle. The issue with velocity smoothing with

regards to electric vehicle is the ability to recharge the battery by use of regenerative braking. Velocity smoothing would reduce the scope for the optimized cycle to recharge the battery in braking. The net effect of velocity smoothing where the battery discharging is lowered due to lower energy demand and battery charging is lowered due to smaller braking are analyzed in this section.

The electric vehicle analyzed in this section is the Tesla Model S, modeled in ALPHA [3] by the U.S. EPA. Just like the conventional vehicle, the ALPHA model in this case takes the input of the drive cycle and simulates a vehicle run over that drive cycle. The entire vehicle is modeled in the program giving simulation results from the motor operating points down the powertrain into the transmission, final drive and vehicle resistance. The ALPHA model provides comprehensive vehicle data at every point in the powertrain which will aid in the analysis of the battery energy consumption and where the gains are being made due to the smoother drive cycles.

5.2 LA 92 Drive Cycle Analysis

Starting with the LA92 drive cycle, which is a high speed modern urban cycle that represents traffic conditions in today's world most accurately, it was found that the MPGe of the optimized drive cycle was 12.4% higher than the MPGe of the standard LA92 drive cycle. MPGe or miles per gallon equivalent is established by the EPA to convert electric energy to gasoline energy in terms of normalizing cost. That is, from the MPGe numbers a customer would be able to understand their fuel costs. The conversion is 33.7 kWh of electricity is equal to 1 gallon of gasoline. So for our case, the MPGe of the standard cycle is 91.1 while for the optimized cycle is 102.4. The percentage increase of 12.4% is smaller than for the conventional vehicle where it was 15.3% over the optimized drive cycle. A part of the gains in energy saving during acceleration is lost during deceleration where the standard cycle recharges its batteries more than the optimized drive cycle.

A 13.2% decrease in propulsion energy over the total braking and propulsion energy translates to a 19.6% decrease in battery discharging. Or in other words the motor consumes 19.6% less battery energy due to the savings in energy on the standard drive cycle. However, a 12.4% decrease in braking energy over the total braking and propulsion energy leads to a 8.4% less battery charging. Hence in net

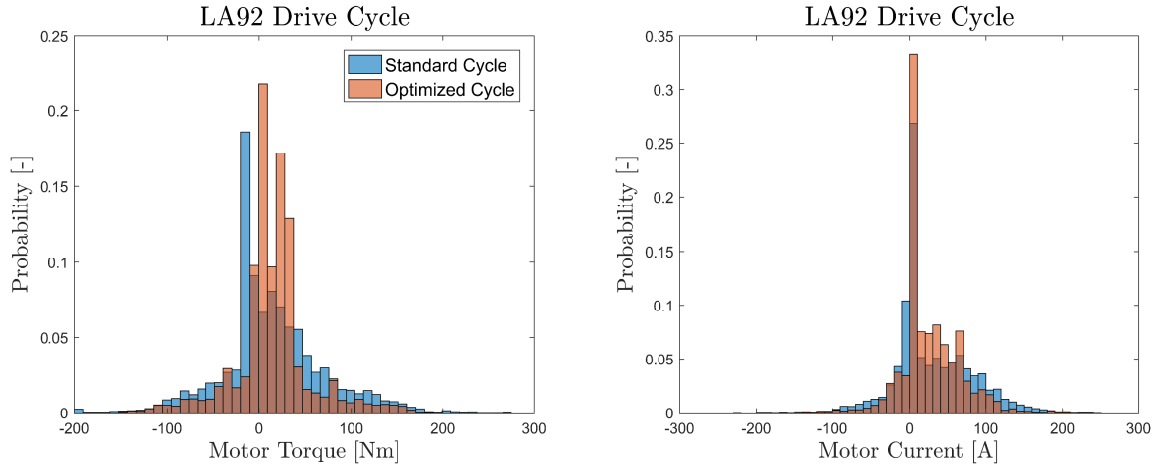


Figure 5.1: Motor Torque and Motor Current distribution for LA92 drive cycle while traversing the standard and optimized velocity traces. The optimized trace clearly has a lower torque demand that is further reflected in lower motor current. This trend was observed for both positive (propulsion) and negative (braking) sides

effect the optimized LA92 drive cycle consumes 11.2% less battery energy. This when translated to MPGe leads to an improvement of 12.4%.

The improvements in MPGe can be directly attributed to the lowered power demand for the optimized drive cycle. As shown in Fig. 5.1, the motor torque distribution for the optimized drive cycle is much narrower than the standard cycle. For the positive motor torque, the acceleration and consequently the propulsion power demand being less reduces the motor torque for the optimized cycle. Reduced motor torque translates to smaller motor current, as can be seen in Fig. 5.1, thus reducing the battery discharging. On the other hand, for the braking side, the standard cycle undergoes more and harsher negative motor torque than the optimized one. This increases the negative motor current and therefore charges the battery more. Hence the reduced battery discharging in the optimized drive cycle is somewhat offset by reduced battery discharging. However, it was found that the net effect for the LA92 drive cycle was favorable to the optimized cycle as indicated by the numbers above.

An interesting result of the optimization of the drive cycles is the reduction of frequent accelerations and decelerations by applying a constant, slower acceleration velocity trajectory. These are able to meet the position constraints and at the same time minimize the total accelerations and decelerations. In Fig. 5.2, two such events are shown where the standard cycle undergoes acceleration, deceleration and another acceleration while the optimized cycle is able to traverse the distance at a smaller rate

of acceleration. In both these cases, during the deceleration event, the standard cycle is able to recharge its battery to some extent. At 29 s, the start of the acceleration profile the difference in battery energy between the standard and optimized drive cycle is 7.3 kJ. At 43 s, the end of the deceleration for the standard cycle, the difference is -1.3 kJ, indicating that the optimized cycle had used more battery energy. But at the end of final deceleration at 65 s, the battery energy difference was 25.9 kJ thus showing that overall from 29 – 65 s the optimized cycle used a net 18.6 kJ of energy less than the standard cycle.

Extending this further, at 85 s, another point at the end of a deceleration in the standard cycle, the difference in battery energy is 29.6 kJ, while at the end of the profile at 115 s, it is 113 kJ. A net gain of 87.1 kJ of energy in the velocity profile from 65 – 115 s. Hence, we can conclude that while for an electric vehicle, the presence of extra deceleration does increase the battery recharging, a net reduction in energy demand at the wheels leads to a net smaller demand from the batteries. In fact on exploring this phenomenon further, this conclusion can be further validated. At the times 73.7 s and 91.8 s the standard and optimized drive cycles both have almost the same velocities. However, in between, the standard cycle undergoes a period of rapid acceleration followed by sharp deceleration and again a rapid acceleration. On the other hand, the optimized drive cycle slowly increases its speed in the same time period. In this period, the propulsion energy demand was 84.4 kJ higher for the standard cycle leading to a 95.8 kJ higher energy discharge from the batteries. While the braking energy was 80.7 kJ higher for the standard cycle leading to only a 40.3 kJ higher battery charging. The net effect being that almost similar increases in propulsion and braking energy resulted in less than half the increase in battery charging as compared to discharging.

This can be attributed to the efficiency in both converting braking energy at the wheels to negative motor torque as well as the efficiency in converting negative motor torque to battery charge. While for battery discharging the average motor efficiency for both cycles was 92.7%, and powertrain efficiency was 95.1%. In braking the powertrain efficiency or the efficiency in converting braking power to negative motor power was only 65.4%. The sharp drop in efficiency in utilizing the braking power is primarily responsible for the lower battery recharging in braking. The effect gets further compounded by the low efficiency in battery charging which was

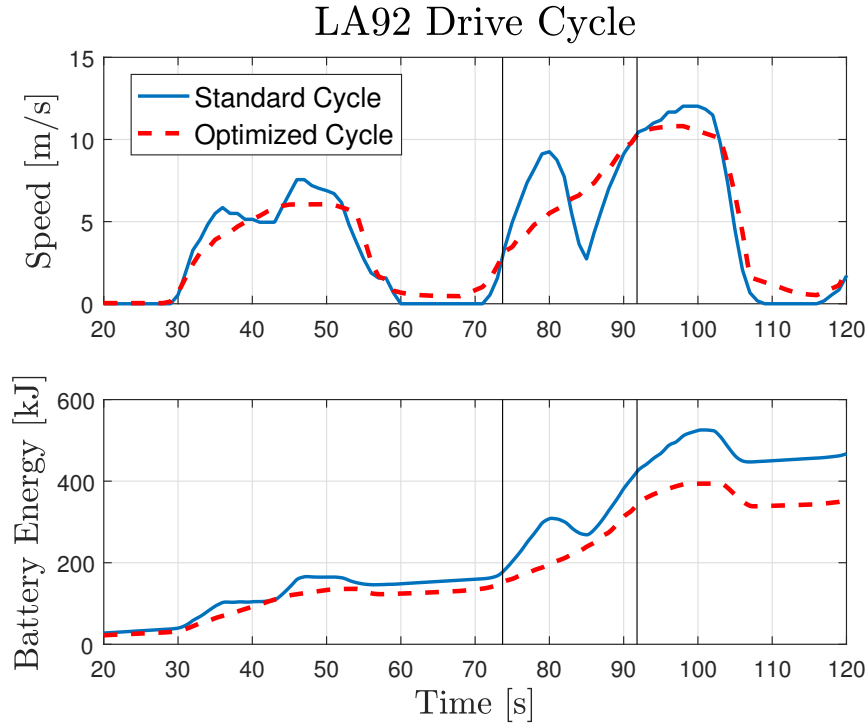


Figure 5.2: Velocity traces for the standard and optimized drive cycles in the first 120 s of LA92 drive cycle, with the Battery Energy consumed in that time period. Between the solid black lines the standard cycle accelerates, decelerates and accelerates again at a high rate while the optimized cycle accelerates slowly to reach the same velocity. In this period the optimized cycle consumes 55.5 kJ less battery energy.

found to be only 76.4% in the given time period. These efficiency results further validate the conclusion that the optimized drive cycle, reducing total accelerations and decelerations is better even for an electric vehicle with regen braking capability and can reduce the battery energy consumed over a drive cycle. These results are however different for a conventional vehicle without the ability to recover braking energy.

A common criticism of the MPGe number released by the EPA is that it does not convey the range of an electric vehicle. This is valid, as for an electric vehicle with a limited battery pack, the range that it covers becomes a very important factor. As indicated earlier, due to the reduced demands of energy in the optimized cycle the battery energy consumption undergoes reduction for the same distance covered. This would increase the range of the vehicle under the same conditions with the same battery pack size but only through optimal driving. The vehicle covers about 2.7 miles/kWh for the standard cycle while increasing its range to cover 3.1 miles/kWh. An average of 0.4 miles/kWh extra can be covered with an optimized

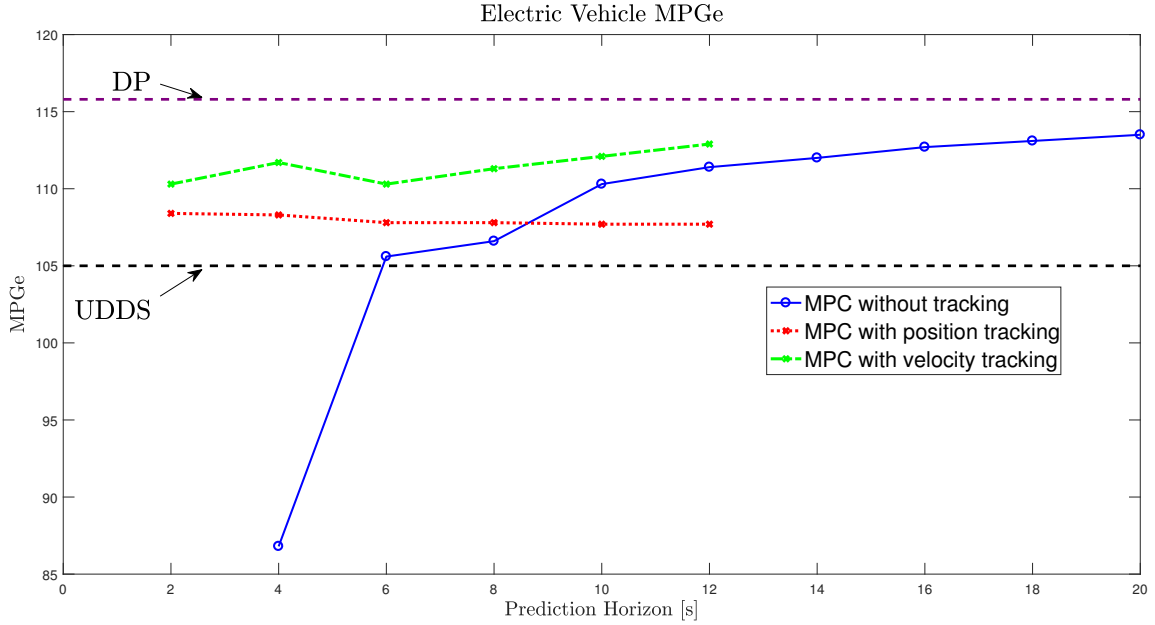


Figure 5.3: MPGe for different velocity traces found using a range of prediction horizons with different MPC formulations for the UDSS drive cycle. The constant black and purple lines indicate the MPGe for the standard and DP optimized drive traces. For shorter prediction horizons, MPC without tracking does not work at all and tracking has to be introduced to improve results exactly like the conventional vehicle. Velocity tracking performs better than position tracking, but with longer prediction, the no tracking case improves MPGe significantly

cycle or a 14.8% increase in range with the same battery capacity. For electric vehicles, a significant range increase through optimized drive cycles represents an exciting opportunity outside of the battery technology. Range anxiety has been one of the major negative attributes of electric vehicles and a simple algorithm to increase range without any changes to existing vehicle technology can improve acceptability of these vehicles.

5.3 UDSS Drive Cycle Analysis

Similar to the analysis for the conventional vehicle, the DP results are only offline optimal solutions when the velocity trajectory of the entire lead vehicle is known. This is not acceptable for a real world implementation where only a few seconds of preview can be got for the lead. The MPC formulations and resulting velocity trajectories have been explained previously, this section deals with the electric vehicle energy consumption in traversing those trajectories.

For the DP optimized UDSS drive cycle, the improvement in MPGe is 10.4% for the optimized drive cycle over the standard cycle. A 10.8% reduction in propulsion

power demand leads to a 17.2% reduction in battery discharge. While a 10.6% lower braking power translates to a 7.7% lower battery charging. The net reduction in battery energy consumed is 9.5% which amounts to an 8.8% improvement in range.

For the online implementation using MPC optimization, the results for the UDDS drive cycle were very similar to those found with the conventional vehicle. For the MPC optimization without any tracking, at short prediction horizons of less than 6 s, the MPGe was lower than that of the standard drive cycle. With increasing prediction horizon, the MPGe increased steadily.

For shorter prediction horizon with position tracking, it was found that the MPGe, improved dramatically from 1.5 s prediction horizon to 2 s prediction horizon and then was slightly decreasing with increased prediction horizon. For 1.5 s, the propulsion power was only 2.3% lower and braking 2.2% lower, resulting in a net 2.7% lower battery energy consumption. On the other hand for 2 s prediction horizon, the propulsion power is much lower by 3.2% while the braking power is 3.1% lower. As discussed earlier, the efficiency in converting battery power to wheel power in propulsion is much higher than the reverse of converting braking power at the wheels to battery charge. Hence in this case the net battery energy consumption is 3.2% lower. At 4 s prediction horizon, the drive cycle becomes even smoother, but the drop in battery recharging is less than the decrease in battery charging and this results in a slightly lower reduction of battery energy consumption. With the increasing prediction horizons, it can be seen that the propulsion and braking power are almost the same. The difference in these drive cycles was explained previously in that the tracking of the position constraint becomes better and after a certain increase in prediction horizon, no further improvements can be made. In any case, for all the results of MPGe for MPC with position tracking, the difference is less than 1 MPGe, which is insignificant. Hence we can conclude that for electric vehicles, MPC with position tracking can reduce battery energy consumption even at very low prediction horizons of 1.5 s.

Finally for MPC implementation with velocity tracking, the results are again similar to those found with the conventional vehicle. The MPGe increases with increasing prediction horizon, except at 4 s horizon, where the increase is higher than the trend. This behavior was observed in the conventional vehicle too and was explained by the weight tuning between tracking and acceleration optimization.

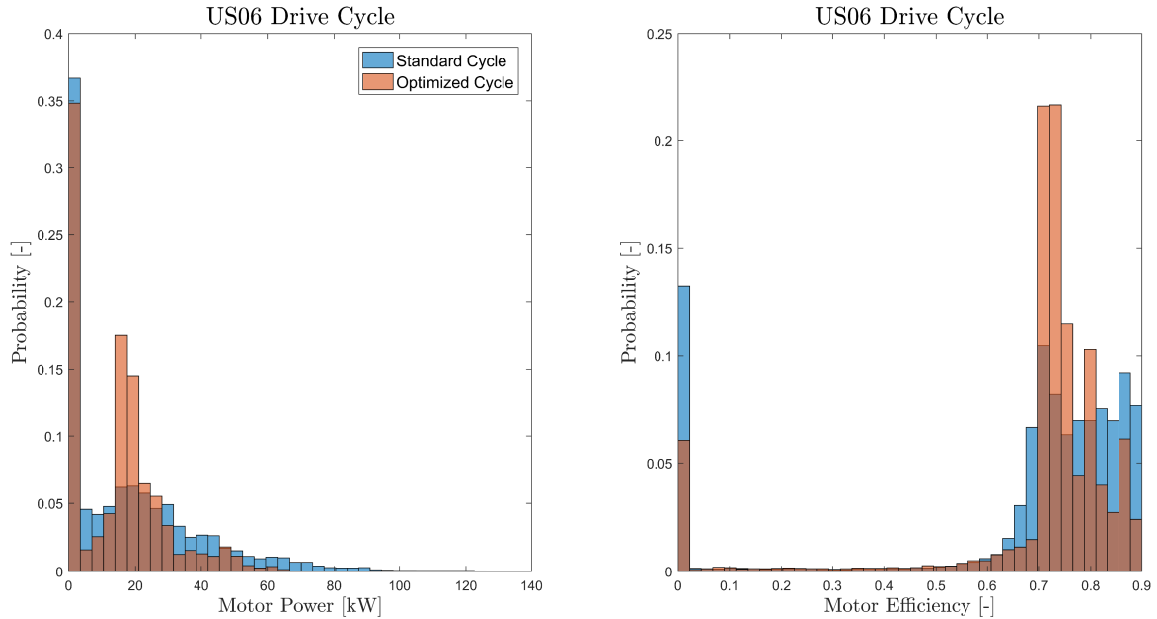


Figure 5.4: Probability distribution of the motor power and motor efficiency in propulsion for the standard and optimized US06 drive cycles. While from previous results it was assumed that the optimized US06 trace would operate for longer at lower motor power, the interesting result is in the motor efficiency. Operating at lower power reduces the motor efficiency.

For all other cases, there is a steady decline in propulsion power demand which reduces the discharge demand. On the other hand, the braking power also reduces but the increase in battery charging is not proportional thus decreasing the net battery energy consumption. These result in an increasing MPGe with increasing prediction horizon. Again, the velocity tracking MPC was found to be better than the position tracking one to decrease battery energy consumption and delivers a 5.1% improvement in MPGe, even at the lowest 1.5 s prediction horizon.

5.4 US06 Drive Cycle Analysis

The US06 drive cycle has the highest rates of acceleration and highest speeds out of all the standard EPA drive cycles. This is a fast highway cycle that undergoes very high speeds of almost 80 MPH, with frequent accelerations and decelerations demanding very high power from the motor but also replenishing the batteries with the frequent braking. With the US06 drive cycles having the highest power demand of all EPA test cycles, all vehicles are geared to meet these high requirements. Fig. 5.4 shows the probability distribution of the motor power and motor efficiency for both the standard as well as the optimized drive cycles. Clearly the maximum as well as

average motor power demanded from the optimized cycles is much less as compared to the standard cycle. This indicates a scope to reduce the size of the electric machine and hence the weight of the vehicle further reducing the power demand for propulsion. Moreover, as the distribution of motor efficiency indicates, the optimized cycle operates for longer periods at low efficiency points. This occurs as the motor has been scaled to meet much higher power requirements. By reducing the size of the motor, the power demand of the drive cycle can be delivered with a higher motor efficiency, thus further reducing the battery discharge. The present simulation tools do not allow for reducing the size of the motor and studying its impacts but the results clearly show a the potential.

During the analysis of the LA92 drive cycle it was stated that the energy recovery in braking was far less efficient than energy use in propulsion thus even at the same reduction of propulsion and braking energy, the net battery energy consumption was always less for the optimized drive cycle. However, two interesting points came up for the US06 drive cycle where the battery charge for the standard cycle was more than that of the optimized cycle.

The first time this happened was at 85 s, here the battery SOC was 0.863 for the standard cycle as compared to 0.862 for the optimized drive cycle. While the difference is negligible, the fact that they were so close after 85 s of driving was explored further. For the cost function minimized by DP, in the given period from 0 – 85 s, the cost reduced from 2.56 to 1.43. Specifically the total acceleration in that time reduced from 3.5×10^3 m/s to 3.2×10^3 m/s, an 8.6% reduction. However, this reduction in acceleration did not translate into reduction in total propulsion energy. In fact the total propulsion energy was 1.57 MJ for the standard cycle, lower than the optimized cycle where it was 1.70 MJ. The difference being a 4.4% higher propulsion energy demand in the optimized cycle. This higher energy demand increased the battery discharge by 6.1% that resulted in the higher battery energy consumption while in the optimized cycle. However, the particular point must be closely observed, in Fig. 5.5, the velocity traces of both drive cycles are shown. Clearly the standard cycle undergoes a braking event at that point while the optimized cycle is still increasing its speed at a low rate of acceleration. This behavior while reducing the total acceleration does increase the total propulsion power. as is also shown in Fig. 5.5.

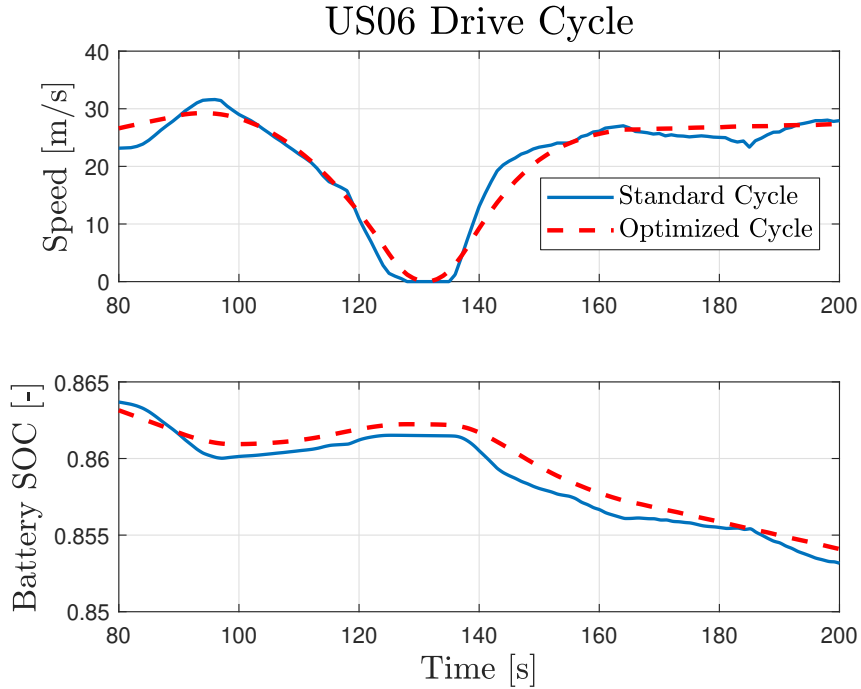


Figure 5.5: Selected portion of US06 drive cycle where the SOC for the optimized cycle is higher in some cases than the standard cycle.

Again the peculiar case where the battery SOC is higher for the standard cycle happens at 185.1 s. A higher battery consumption for the optimized drive cycle 185 s into the trace was again explored. Unlike the previous case, here the total propulsion energy was less for the optimized cycle. In this instance the closeness in battery energy came from the energy gained through braking. Just before 185.1 s, the standard cycle undergoes a significant braking event while the optimized cycle accelerates slowly. This additional braking increases the difference in total braking energy between the two cycles to 341 kJ. At that instant the difference in total propulsion energy is 170 kJ, around half of the braking energy and hence the battery SOC despite the inefficient energy recovery in braking is almost the same for both cases. At 185.1 s, the difference in battery discharging is 128.0 kJ while the difference in battery charging is -128.2 kJ between the standard and optimized cycles.

Having stated the above two examples where despite the reduction in acceleration and deceleration, the battery SOC's are able to converge, it is important to state a caveat. Both instances occurred at the end of a deceleration event where the two phenomenon increased the SOC for the standard cycle. First the obvious battery recharging happened with the braking events and this was compounded by

the optimized cycle still undergoing an acceleration which increased its propulsion power as compared to the standard cycle. The combination of these forces produced similar SOC results almost 185 s into the drive cycle. However, since the optimized cycle was still accelerating, it is reasonable to assume that the standard cycle would have to undergo a succeeding acceleration as well. Indeed, at 185.1 s the difference in battery energy consumed is only -0.01% but by 214 s this difference increases to 7.6%. Thus with this example we can restate the conclusion that the net effect of the optimized cycle will always reduce the total battery energy consumption.

However, the finding that a reduction in acceleration does not lead to a decrease in propulsion power demand is also important. That results indicates that a further reduction in energy consumption is possible if the objective function reduced the total energy demand at the wheels. Another finding is the influence of braking, while the efficiency in converting braking energy to battery charge is much lower than the reverse, it does have an effect and lowers the improvements in energy consumption. The phenomenon is further studied in future work by changing the optimization procedure and introducing a different cost function.

5.5 Road Grade Variation

Prior optimal energy management solutions for electric vehicles have been found for flat roads in both online and offline implementations [83, 84]. However, changing road grades adds an additional gradient force acting for and against the vehicle. In [56], the authors used Pontryagin's Minimum Principle to solve the optimal velocity trajectory of a vehicle traversing a hill. They concluded that the optimal velocity was to "increase speed while approaching the base of the hill, and then allow the speed to drop off while climbing the hill ... and the reverse while descending." Similar results have been proposed for the traversing of road grades by trucks [85] and conventional vehicles [86].

The optimal power management strategy over changing road grades have also been considered for Plug-in-Hybrid Electric Vehicles (PHEV) in [87, 88]. It was found that the proposed optimal solution required additional engine torque when climbing a hill, while during hill descent regenerative braking was used to recharge the battery. The analysis in [89] shows that inclusion of road grade information improves fuel economy for an HEV but does not mention the velocity characteristics

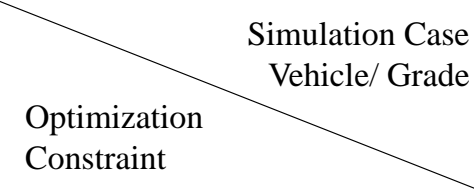



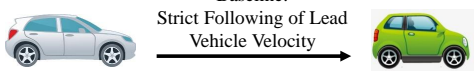
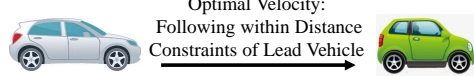
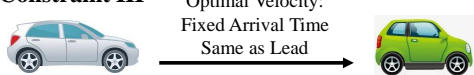
 Optimization Constraint	Simulation Case Vehicle/ Grade Case I Tesla/ GEM grade 	Case II Twice Mass Tesla/ GEM grade 	Case III Military Robot/ Military grade 
Constraint I Baseline: Strict Following of Lead Vehicle Velocity 	Regen Braking during - Hill Descent to maintain given velocity - Baseline	Regen Braking during - Hill Descent to maintain given velocity - Baseline	Regen Braking during - Hill Descent to maintain given velocity - Baseline
Constraint II Optimal Velocity: Following within Distance Constraints of Lead Vehicle 	No Regen Braking during - Hill Descent as all constraints satisfied without braking (+3.2%)	Regen Braking during - Hill Descent to satisfy given position constraints (+5.3%)	Not Considered
Constraint III Optimal Velocity: Fixed Arrival Time Same as Lead 	No Regen Braking during - Hill Descent as all constraints satisfied without braking (+8.0%)	No Regen Braking during - Hill Descent as all constraints satisfied without braking (+14.6%)	Regen Braking during - Hill Descent to satisfy maximum velocity constraints (+24.2%)

Figure 5.6: Three different vehicle cases are considered in this paper with varying power to weight ratios. The first two cases are run for EPA's GEM drive cycle while Case III is run over steeper military grades. For each case, three different constraints are applied all of which force the optimal velocity to traverse the given distance in the same time as constant speed lead. Regenerative braking was observed as part of the optimal solution only in cases where constraints were imposed. The motor energy demand reduction over the baseline for the optimized cycles are also shown in bold.

or changes in hill climbing strategy leading to those improvements. When finding the optimal power split for a constant speed drive through a changing road grade, the authors in [90] proposed that battery energy is used while climbing up the hill and recharged while descending similar to findings in the previous studies.

The conclusion from the literature review is that the period of hill descent is an opportunity to generate electricity for storage using the regenerative braking system. However, the regenerative braking system is not 100% efficient and there are losses during energy conversion. In all these cases, it is assumed that a certain proportion of the vehicle kinetic energy will be lost in braking, and hence some of that energy can be recovered by regenerative braking. On the other hand, if we consider optimal velocity trajectory implementation for autonomous vehicles, then the highest possible efficiency is sought. Hence, braking will be avoided as far the constraints allow, even in hill descent. This paper finds the optimal velocity trajectory while traversing road grades for electric vehicles, through offline globally optimal solutions using dynamic programming. A summary of the case studies and constraints are presented in Fig. 5.6

5.6 Electric Powertrain Model

For this chapter, the electric powertrain model was built utilizing a backward looking scheme, suitable for use in numerical optimization algorithms. The model assumes the vehicle to be a point mass and only includes longitudinal dynamics. The vehicle parameters include the road load and aerodynamic drag coefficients as well as the tire radius and the final drive gear ratio. For the powertrain, an average final drive efficiency is assumed and an experimentally derived motor map calculates the power conversion efficiency. The parameters are listed in Table 5.1. Forces acting on the vehicle are as follows,

$$(5.1a) \quad F_a = M_u a$$

$$(5.1b) \quad F_g = M_s g \sin(\tan^{-1}(\frac{\beta}{100}))$$

$$(5.1c) \quad F_d = A + Bv + Cv^2$$

where a is the vehicle acceleration, β the gradient percentage and v the vehicle velocity. Equation 5.1a) computes the acceleration force, 5.1b) the gradient force and 5.1c) the resistance drag forces. The powertrain model to determine the motor power is as follows

$$(5.2a) \quad \omega_m = \frac{v GR_{fd}}{r_{tire}}$$

$$(5.2b) \quad \tau = \frac{(F_a + F_g + F_d) r_{tire}}{GR_{fd} \eta_{fd}}$$

$$(5.2c) \quad \tau_m = \begin{cases} \min(\phi_1(\omega_m), \tau) & \text{if } \tau \geq 0 \\ \max(\phi_2(\omega_m), \tau) & \text{if } \tau < 0 \end{cases}$$

$$(5.2d) \quad P_m = f(\tau_m, \omega_m)$$

where ω_m is the motor speed, τ_m the motor torque and P_m the electric power of the motor. The functions ϕ_1 and ϕ_2 determine the maximum and minimum torques allowed by the motor. At low speeds, the maximum torque is limited by the peak torque and at higher speeds it is limited by the peak power of the motor. The function f computes the electric power demand of the motor from an experimentally derived motor map. The electric powertrain model used is reasonable, as it showed

Table 5.1: Vehicle Parameters

Name	Parameter	Case I	Case II	Case III
Static Mass (kg)	M_s	2041	4082	453.6
Dynamic Mass (kg)	M_u	2294	4588	453.6
Static Road load (N)	A	194	388	13.6
Dynamic Road Load (N/(m/s))	B	1.97	1.97	0.07
Aerodynamic Load (N/(m/s) ²)	C	0.36	0.36	0.17
Final Drive Gear Ratio	GR_{fd}	9.73	9.73	7.54
Tire Radius (m)	r_{tire}	0.35	0.35	0.28
Final Drive Efficiency	η_{fd}	0.96	0.96	0.96
Velocity Range (m/s)	(v_{min}, v_{max})	(0,40)	(0,40)	(0,22)
Acceleration Range (m/s ²)	(a_{min}, a_{max})	(-6,6)	(-6,6)	(-6,6)

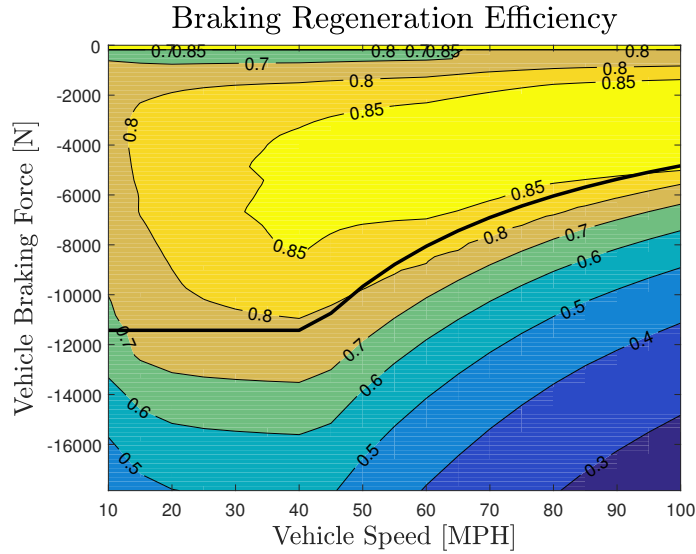


Figure 5.7: The efficiency of the regenerative braking system is determined by the powertrain and generator efficiency. Also, braking power beyond the generator torque and power limits, shown by the thick black solid line is dissipated as heat, which reduces efficiency further at high loads and speeds.

only a 0.18% normalized RMS error in motor electric power demand, from simulation results of an experimentally validated high fidelity model [3].

Utilizing the model, a 2-D map of the regenerative braking efficiency can be generated as shown in Fig. 5.7. The efficiency is of converting mechanical power at the wheels to electric power in the generator. The generator capacity is limited and is shown by the thick black solid line in the figure, beyond which additional power is dissipated as heat.

5.7 Optimal Control Problem

While the autonomous self-driving cars and unmanned robots give an additional flexibility to control and optimize the vehicle velocity, constraints should still be

considered based on the traffic requirements. Three different constraints are applied in this chapter as shown in Fig. 5.6.

The first constraint case is simply a constant speed cruising where the autonomous vehicle maintains a constant speed while traversing the given road grade. This is our baseline case and is referred to as the standard cycle or constraint I.

The second constraint case, constraint II is the same traffic constraints imposed before in Section 3.2.2.

The final constraint case, constraint III enforces a fixed time duration for the autonomous vehicle to cover the given distance. Here, the autonomous vehicle has to cover the distance in the same time as the constant speed baseline without the previous time varying position constraints. This is the most lenient constraint and is most relevant for the military application where the distance and time are set based on the mission. It must be noted that all three cases have the same travel time and velocity optimizations are made within those strict time durations.

Utilizing this concept, the simplified electric vehicle model was used to optimize the velocity trajectory by minimizing motor power demand within reasonable traffic constraints and vehicle limits. The problem is defined in Eq. 5.3

$$\begin{aligned}
 (5.3a) \quad & \min_{P_m} \sum_{k=0}^{N_f-1} P_{m,k} \\
 (5.3b) \quad & \text{s.t. } a_k \in (a_{min}, a_{max}) \\
 & v_k \in (v_{min}, v_{max}) \\
 & s_k \in (s_k^{\min}, s_k^{\max}) \\
 & k = 0, \dots, N_f - 1,
 \end{aligned}$$

where N_f is the final time-step, and a_k , v_k and s_k are the instantaneous vehicle acceleration, speed and position respectively.

The above cost function minimizes the motor electric energy demand for an electric powertrain. When considering a hybrid powertrain, fuel consumption minimization is more important and significant efficiency gains can be made by changing engine operating points affecting the overall efficiency of the system. Hence, we stress that the results are only valid for vehicles with an electric motor as the only propulsion source.

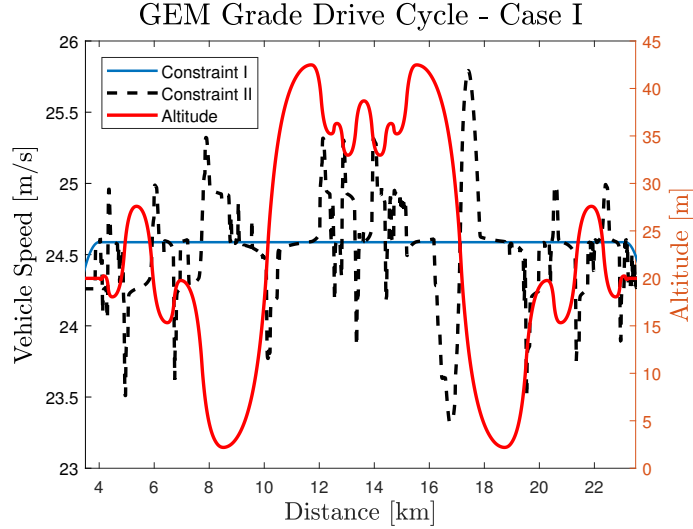


Figure 5.8: The vehicle velocity for the constant velocity 55 MPH standard cycle of constraint I and the distance constrained optimized cycle of constraint II are plotted on the left y-axis. The altitude is shown on the right y-axis. The distance constrained optimal velocity was able to reduce the motor energy demand by 3.2% over the constant velocity case.

5.8 Results and Discussion

The drive cycle was optimized through the Dynamic Programming (DP) algorithm. DP is a numerical method which computes a set of inputs that minimize a given cost function [51]. In our case, we use the DP implementation in the DPM function [52] to minimize the motor electric power demand, which includes regenerative braking. The DP formulation has one input of vehicle power and two states of position and velocity. Input power is limited between ± 20 kW and is discretized with 201 points. The constraints for state of position are time varying for constraint II given by Eq. 3, while for constraint III it is time invariant with a hard constraint for the final time step, to ensure that the autonomous vehicle covers the given distance. The state of speed is constrained between 0 and the maximum speed of the given vehicle. Both states are discretized with 201 points. As mentioned before, the cost function is the electric power demand of the motor where negative power demand from regenerative braking reduces the cost.

The optimization was carried out for three case studies with different vehicle masses varying the power to weight ratio from 44 – 110 W/kg. A schematic diagram of the different case studies and optimization constraints is shown in Fig. 5.6.

5.8.1 Case Study I : Tesla Model S as an EV

The vehicle parameters for the Tesla Model S were found from dynamometer experiments at the US EPA's National Vehicle and Fuel Emissions Laboratory (NVFEL) listed in Table 1. Under the US EPA's Greenhouse Gas Emission Model (GEM) a varying road grade profile has been developed. The standard cycle completes the given GEM grade at a constant speed of 55 MPH. Utilizing the given road grades, the optimal velocity while traversing these road grades were sought through DP. When optimizing for motor energy, the DP optimization was constrained by maintaining a reasonable following distance to the constant velocity lead. Reductions are seen in the electric motor power demand of the optimal drive cycle. The resulting velocity profile and the road grade are shown in Fig. 5.8.

The optimized cycle for constraint II showed a 3.2% reduction in energy consumption over the standard cycle operating at constant speed. These improvements came by allowing for changes in speed, similar to the previous studies on optimal velocity profiles over road grades. Vehicle velocity increased at the base of a hill and reduces as the vehicle climbs and on descent the vehicle velocity increases. Optimized motor power followed the standard one for the most part, except for some deviations at steeper road grades. The main difference was seen during hill descent, where the motor shuts off instead of braking and generating electricity through the regenerative braking system.

To study this phenomenon more closely, the hill descent from 7 – 8.1 km was analyzed in the left plots of Fig. 5.9. During a long hill descent, the optimized cycle followed the motor power of the standard cycle except for two instances. Between 7.2 – 7.3 km, the motor shuts off thus reducing speed slightly below the constant speed. Later as the standard cycle brakes to maintain speed after 7.6 km, the optimized cycle shuts off the motor again and allows for an increase in speed. At 7.77 and 7.85 km the motor applies short bursts of power to increase the speed further before shutting off again to reduce speed. At 8.02 km the motor goes back to the standard operation to maintain speed. Through the deviations the motor was able to save about 3.6% in total electric energy for the observed distance.

Similar behavior was observed during the longer 2 km descent from 16 – 18 km shown in the right plots of Fig. 5.9. The motor shuts off at times which slightly reduced speed, but at the steeper descent, it either shut off or provided short bursts of

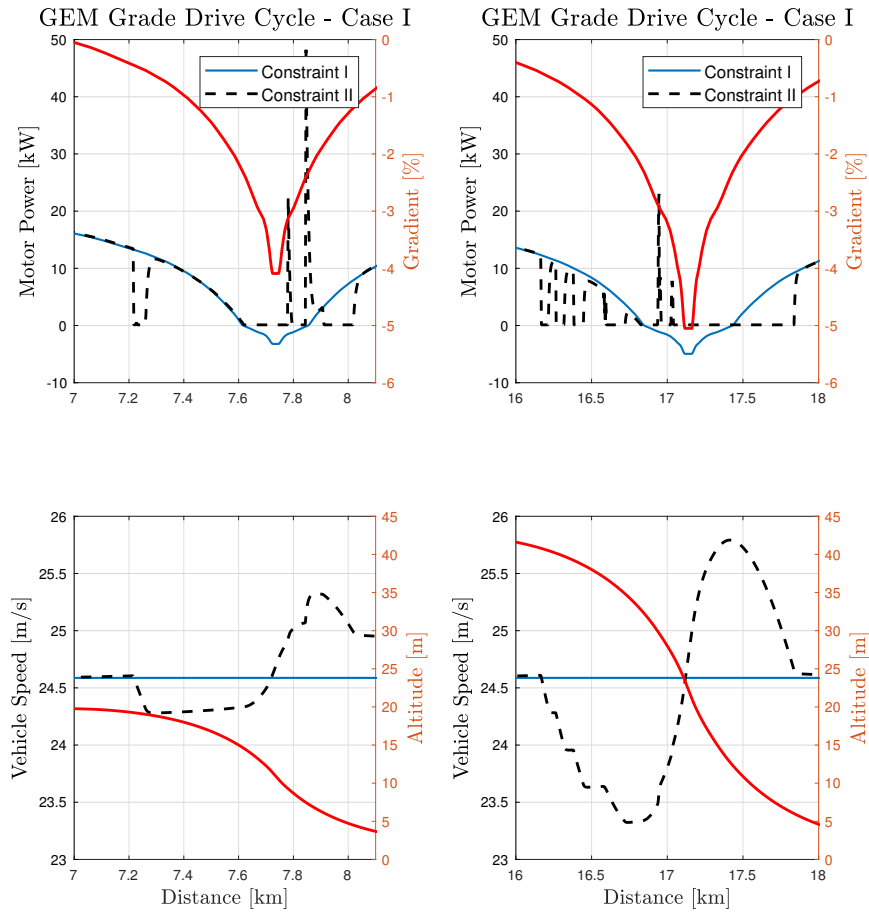


Figure 5.9: Magnified plots of the vehicle velocity and motor power while the vehicle descends downhill. In both constraint cases, while the constant speed standard cycle brakes to maintain speed on the negative gradient, the optimal policy is to avoid braking and coast. When the negative slope is low, the vehicle velocity reduces but when the negative slope increases, the vehicle velocity increases as well.

power instead of braking which led to an increase in speed. As the descent became less steep, the motor remained off allowing the vehicle speed to reduce the constant speed before returning to standard operation. Again by these deviations, the motor was able to save 35.2% energy as compared to the baseline. The increased improvements for this segment are due to the steeper descent, which provided more opportunity for coasting during the optimized cycle as well as the longer distance which required more tractive energy for the baseline.

Interestingly, the optimized trajectory during descent did not utilize regenerative braking at all, and instead utilizes gravitational force to increase the kinetic energy of the vehicle. The vehicle is sometimes propelled forward by the motor to increase velocity beyond the acceleration from the negative gradient. These results occur

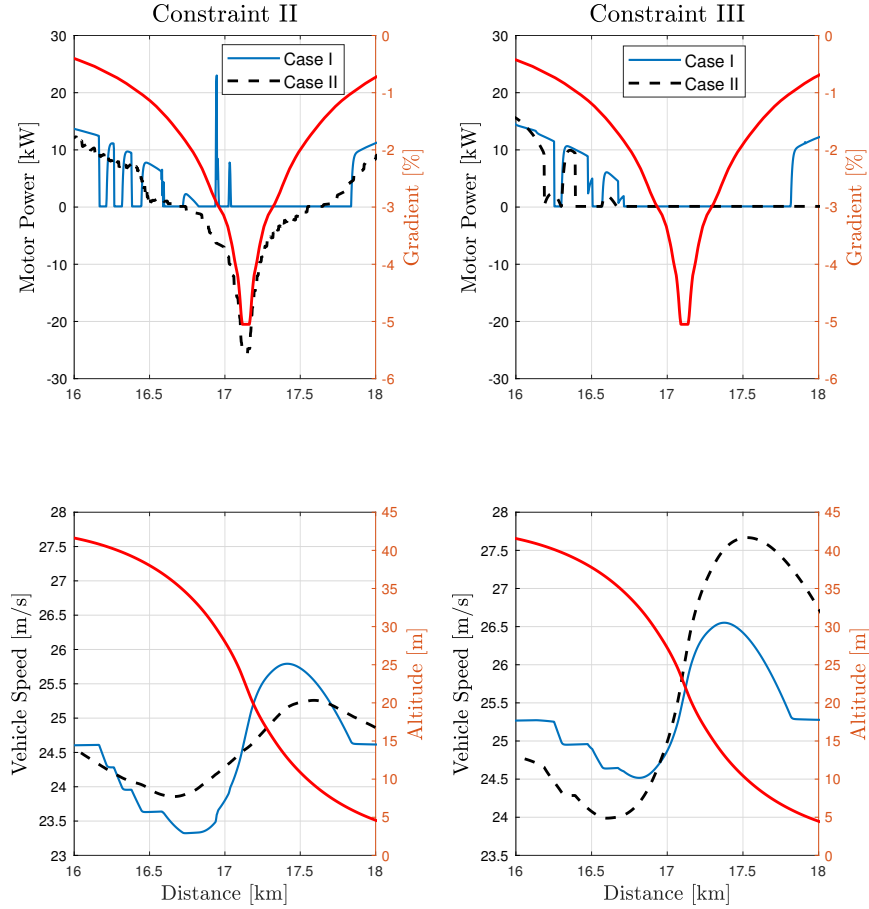


Figure 5.10: The plot on the left shows the motor power and vehicle velocity with time varying tight constraints of constraint II, while the plot on the right shows the case with only the initial and final constraints of III are applied. Due to the tight constraints on the left, the double mass case brakes to meet them while on the right the velocity is allowed to increase more.

despite regenerative braking power being a negative cost in DP. The optimal solution found by DP indicates that coasting with the motor shut off is preferred over regenerative braking. This can be explained by the efficiency losses in converting mechanical power to electricity and back to mechanical power, thus even with very high conversion efficiency, the round-trip efficiency is lower.

5.8.2 Case Study II: Heavier Mass EV

While the regenerative braking efficiency is determined by the generator characteristics, the absolute braking force is governed also by the mass of the vehicle. To understand the effects of a higher mass requiring a greater braking force, the mass of the vehicle was doubled in simulations as listed in Table 1, without changing the motor size. In comparison between the standard and double mass, the velocity pro-

files are similar as shown in the left plots of Fig. 5.10 the only difference being the magnitude of the motor power. But again, the optimal policy prefers shutting off the motor rather than braking to recover energy through regen except for one instance around 17 km. The particular velocity profile during the long hill descent shows that for the double mass case II, the motor power becomes negative. This implies that the regenerative braking system is being used.

We speculate regenerative braking is only being used to avoid violating the distance following constraint. To confirm our speculation, we loosened the strict constraints imposed on the previous optimization. The above simulations were carried out utilizing the leader-follower scheme, but in these cases, we can remove the time varying constraints and only apply the initial and final distance constraints while also constraining the arrival time to that of the constant speed case. This is constraint case III.

Again, even without time varying constraints, the optimal policy is to coast rather than brake to regenerate power. It is shown in the right plots of Fig. 5.10 that even with the doubled mass, removing the tighter position constraints allowed the double mass to avoid braking and increase its speed to beyond that of the standard mass. Hence as speculated, braking was initiated only to meet the given constraints on position and not to recover energy.

5.8.3 Case Study III: Proposed Light Weight Military Robot

Since the previous results with the Tesla S simulations show that the optimal policy while traversing grades is to coast rather than brake, yielding a significant reduction in electric energy demand, it poses an interesting question for lighter vehicles traversing steeper hills. It was shown that the only time the optimal DP policy used regenerative braking was with the double mass vehicle where the velocity increase during descent had to be curbed by braking. In this case, we consider a lighter vehicle, a small 1000 lb autonomous military robot. The robot is powered by a series hybrid system incorporating a fuel cell and a battery, such that the propulsion is provided only by the electric motor. Hence it can be assumed to have the same electric powertrain as our previous cases. An efficiency map based on the downsized motor of the Nissan Leaf was used as the power source for the robot. The vehicle parameters are listed in Table 1.

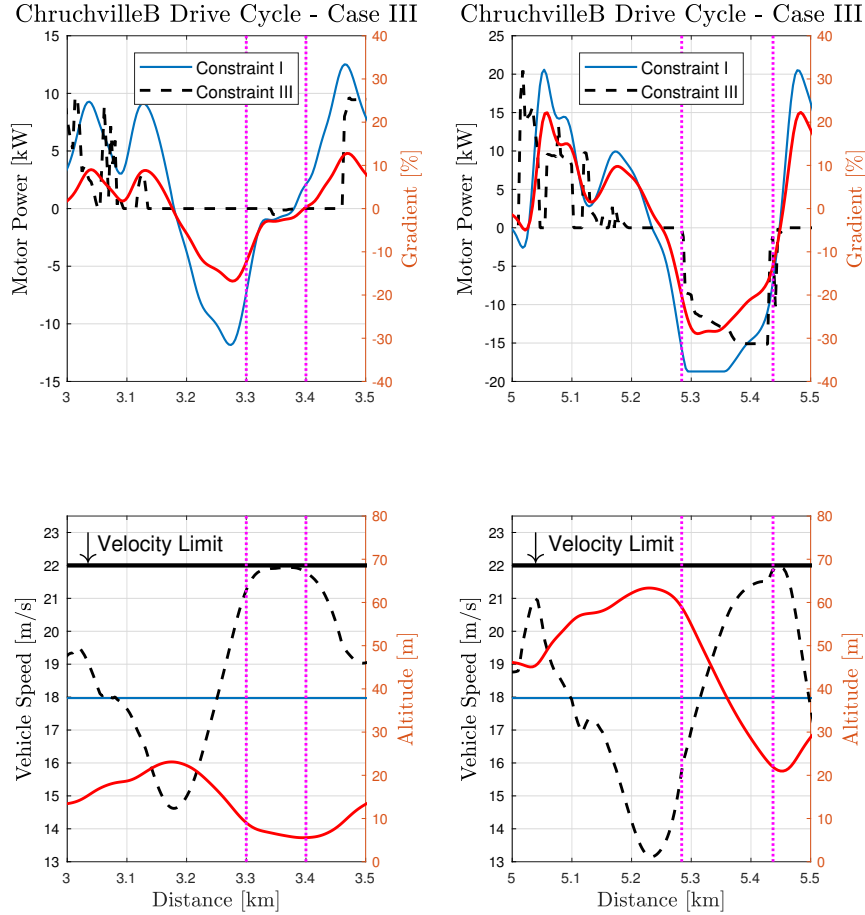


Figure 5.11: When the DP optimization is carried out for the small 1000 lb robot in case III, optimized velocity trajectory obtained through constraint III shows a reduction of 24.2% over the constant speed standard cycle of constraint I.

These robots are meant to be used on in rugged environments which are much steeper than the GEM grades used previously in this paper. The ChurchvilleB military drive cycle was used for demonstration of the optimal algorithm with peak grades of 30% [91]. Further, these steeper grades with a much higher negative gradient force would also test our hypothesis of regenerative braking being avoided. Since the vehicle is operated autonomously off road, only the constraint III case on total trip tip time was considered for optimization.

Selected distance segments of the results are shown in Fig. 5.11, where the optimal velocity deviates significantly from the constant velocity case by following the optimal principles of hill climbing. These deviations reduced electric energy demand for the motor by 24.2%. The motor results are interesting and different from those of the Tesla as the maximum velocity of the robot is limited to 22 m/s. In the left plots

of Fig. 5.11 from 3 – 3.5 km, the optimized cycle does not use the motor but the robot velocity does not violate the limit. On the other hand in the right plots, with a much steeper drop, the robot has to apply regenerative braking to maintain the velocity within the constraints. Applying brakes leads to negative motor power and regenerative braking. But the reason behind applying brakes was to stay within the velocity constraints and not use regenerative braking, otherwise even in the left plots brakes would have been applied.

These results have interesting implications for the battery sizing of these robots as these are powered by a hybrid fuel cell system. The results prove that for the unmanned case, where the velocity can be controlled, the optimal policy in traversing the road grades is to avoid regenerative braking due to the low round-trip efficiency. This implies that a large battery to store the regenerated electricity is not required and an appropriate battery size that meets other requirements of the robot would suffice.

Having stated this, it is important to note that the above conclusions are drawn only for unmanned robots where the velocity can be controlled to drive an optimal path. Moreover, as was shown in the ChurchvilleB cycle, there are some cases where the robot velocity can increase to beyond operational limits and brakes have to be engaged. In these instances, having the capability to store regenerated braking power would reduce fuel demand.

5.9 Case IV: 100% Efficiency in Regeneration

Till now our conclusion is that the optimal policy is to avoid regenerative braking during hill descent, and the reason for doing so is assumed to be due to the low round-trip efficiency of the system. To verify this assumption, we simulate a case with 100% round-trip regeneration efficiency. In this case, we assume that all braking power will be converted to electricity and back to propulsive power. This is done by removing the powertrain and motor efficiencies. Simulation results for motor power in Fig. 5.12 clearly show that with full recovery, regenerative braking is preferred during the hill descent. The plots record several periods of braking to reduce vehicle velocity and recover energy. This result validates our assumption and shows that only with no round-trip efficiency losses regenerative braking is a part of the optimal path.

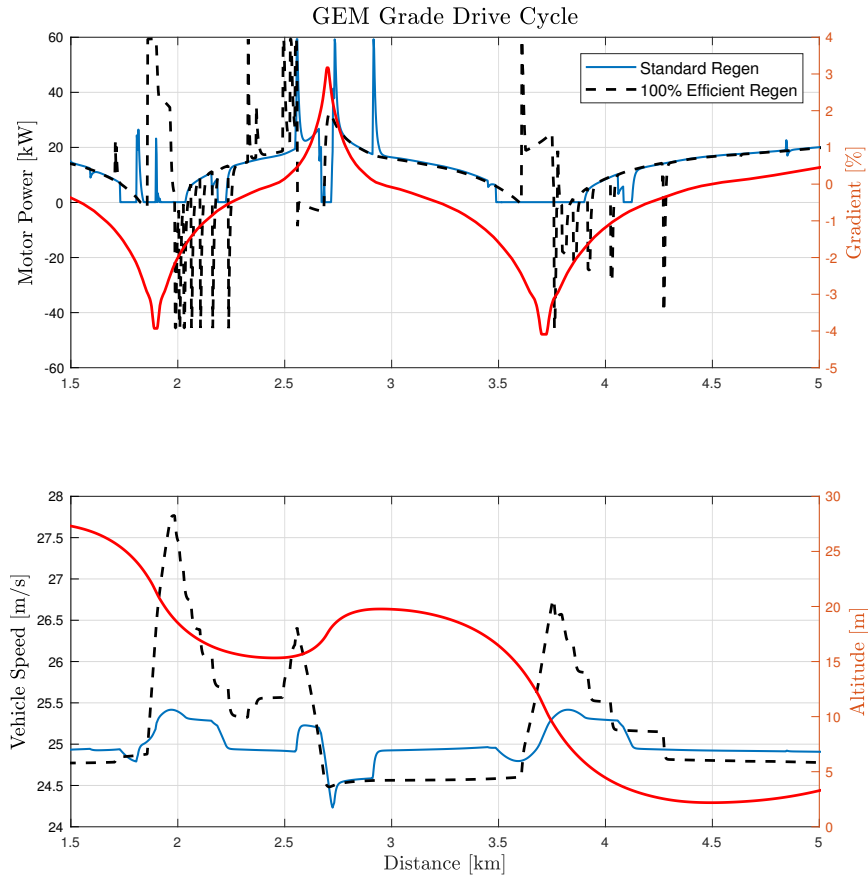


Figure 5.12: If the round-trip regeneration efficiency is assumed to be 100%, the optimal policy does include several braking events while descending downhill.

However, the generator efficiency is an important consideration in the analysis. For example, if the powertrain and generator efficiency were included for the results from the 100% round-trip efficient case, the motor electricity demand would increase by 4% over the previously determined optimal path. The reason for this loss is simply that even with a high efficiency of 90% in the motor/generator, the overall efficiency in regeneration is 81%. Hence while regenerative braking is useful in utilizing force that would otherwise be dissipated as heat, the low efficiency of the system means that in the optimal path, braking should be avoided altogether.

5.10 Conclusions

The optimal velocity trajectory to reduce the motor electric energy demand was investigated in this paper. While traversing varying road grades, the optimal solutions were shown to avoid braking as far as the constraints allowed and not use

the regenerative braking system. These results were replicated for lighter robots on much steeper road grades. It was shown that only with unrealistic 100% efficient power recovery, regenerative braking was a part of the optimal solution.

While regenerative braking and eco-driving are both methods for range extension of EVs, the former should only be utilized to meet vehicle limitations or traffic constraints. Utilizing the motor energy minimization strategy, significant energy reductions up to 24% were shown for changing road grade which translates into a corresponding increase in range. In other words, a significant increase in driving range can be achieved without increasing battery size.

CHAPTER VI

Fuel Cell Vehicles

The optimization in this chapter is the power split in a Fuel Cell hybrid vehicle for military applications. Military vehicles are typically armored, hence the open surface area for heat rejection is limited. Hence, the cooling parasitic load for a given heat rejection can be considerably higher and important to consider upfront in the system design. Since PEMFCs operate at low temp, the required cooling flow is larger to account for the smaller delta temperature to the air. We will apply scalable physics-based models of the fuel cell stack and a balance of plant that includes a realistic parasitic load from cooling integrated with existing models of the lithium ion battery. This model allows the combined optimization that captures the dominant trends relevant to component sizing and system performance. The baseline optimal performance is assessed using dynamic programming for a reduced order model, by assuming a static cooling load required to maintain the stack at the operating temperature with peak efficiency. Pseudo-spectral optimization methods, which enable fast computation even for larger number of states in the model is then used to consider the additional control of the cooling system. For scaling of the battery in the hybrid system we can use a modular approach, adding cells in parallel and series. If the fuel cell operates always with net power above the peak efficiency point, a simple rule based strategy can nearly recover the optimal fuel consumption achieved with dynamic programming.

6.1 Introduction

In the previous chapter on electric vehicle optimization, we found the optimal velocity trajectories that reduces the power demand from the motor. In this last chapter, we will investigate the optimal power split in a Fuel Cell (FC) hybridized

with a lithium ion battery that powers a vehicle similar to the one modeled previously. In this chapter, we don't manipulate the drive cycle, instead we focus on optimizing the power split between the Fuel Cell and the battery for a given motor power demand.

The army has been investigating the use of hydrogen as a battlefield fuel to enable silent mobility. In addition, hydrogen fuel can be produced in theater by electrolysis of water or reforming hydrocarbon fuels. Proton Exchange Membrane Fuel Cells (PEMFCs) are a promising alternative to internal combustion engines for this task due to their silent operation, low heat signature ($70^{\circ}C$ operating temperature), and higher efficiency (peak near 50%). Fuel cell systems are typically hybridized with a lithium ion battery pack to help filter the load demand and support the power draw of the auxiliary balance of plant components such as pumps and blowers during startup and shutdown.

Air-cooled stacks are attractive for systems with lower power density and those below about 5kW. The reduction in system mass and complexity is beneficial for portable applications, as opposed to transportation systems where power density is critical to reduce the system volume. For higher power density systems, liquid cooling provides the necessary heat rejection from the stack. In the air-cooled systems considered here, the cathode airflow is also used to cool the cell and regulate temperature. The flow rates for cooling are typically greater than 20x of the stoichiometry needed for the hydrogen oxidation reaction. In this case, the air blower is the main parasitic load in the balance of plant, and should be considered in the control design to obtain the energy optimal power split.

In the following sections, the system model is presented including the stack polarization curve, for which the slow dynamic of fuel cell temperature is considered as a dynamic state. The battery is represented by a single dynamic state, its state of charge (SOC). Next the optimal power split for several military drive cycles are investigated using dynamic programming and a static fuel cell efficiency by assuming the fuel cell is able to operate at the ideal temperature. Finally, the dynamic stack cooling requirements are considered to maintain fuel cell temperature and again the optimal power split is calculated using pseudo-spectral co-location methods to enable the computation with a larger number of states and inputs in the model. Comparisons with the optimum power split based on the static efficiency map and rule based

power split strategies are presented.

6.2 System Models

As stated previously, the vehicles under consideration are a small packbot robot [92]. The nature of the surveillance missions are such that the path and terrain are well defined, so in this work we can consider a known vehicle trajectory and optimize the power split over a given profile power [93].

6.2.1 Fuel Cell Model

The fuel cell voltage, and hence power can be parameterized by the operating temperature, T_{fc} , current I_{fc} , and oxygen partial pressure in the cathode $P_{O_2,ca}$. In the case of an air breathing PEMFC, we can assume the oxygen partial pressure is the same as ambient conditions, or 0.21 atm. Fuel cell polarization curves are typically functions of the current density $i = \frac{I_{fc}}{A_{fc}}$, where A_{fc} is the stack active area in cm^2 . An empirical relationship for the cell voltage is then given by

$$(6.1) \quad V_{cell} = E_{0,rev}(T_{fc}) + \frac{RT_{fc}}{nF} \log \left(\frac{p_{H_2} \sqrt{p_{O_2}}}{p_{H_2O}} \right) - \frac{2RT_{fc}}{F} \sinh^{-1} \left(\frac{I_{loss} + I}{2I_{oc}} \right) - IR_{ion} + B_c \log \left(\frac{1 - I}{I_{max}} \right)$$

The theoretical open circuit potential $E(T_{fc}, P)$ is given by the Nernst equation [40],

$$(6.2) \quad E(T_{fc}, P) = \frac{\Delta G(T_{fc})}{nF} = 1.256 - 2.26 \times 10^{-4} \times T$$

Where $\Delta G(T)$ is the temperature dependent Gibbs free energy.

The value of the parameters in the polarization curve can be found in Table 6.2.1. The fuel cell polarization curve and net power are plotted in Fig. 6.1. The fuel cell voltage varies slightly, decreasing with temperature as shown. The optimal stack operating temperature for the Ballard 1020ACS Stack was found experimentally in [94], however the authors did not consider the parasitic loss of the fan. The effect of increased membrane resistance due to drying at high temperatures, and flooding at low temperature are not included in the present model [95, 96], should be considered in subsequent work.

The fuel cell heat generation is given by

Table 6.1: Fuel Cell Parameters

Parameter	Value
AFC [cm^2]	150
mC_p	100
i_{loss} [A]	0.001
i_{OC} [A]	0.7
B_c	0.12
α	0.5
R_{mb} [ohm]	0.05
R [$J/molK$]	8.314
F [C/mol]	96,485
R_B [ohm]	0.18
N_p	3
N_s	8
Q_b [Ah]	1.875

$$(6.3) \quad Q_{gen} = (E^{th} - V_{cell})I_{fc}N_{cells}$$

Where N_{cells} is the number of series cell in the stack and $E^{th} = 1.256$ V. The fuel cell stack temperature dynamics can be modeled by the following differential equation,

$$(6.4) \quad mC_p \frac{dT_{fc}}{dT} = \frac{Q_{gen}}{N_{cells}} - Q_{cool}$$

Where mC_p is the heat capacity of a single cell and the cell heat removal rate, Q_{cool} , is given as a function of the per cell flow rate,

$$(6.5) \quad Q_{cool} = \frac{1}{h} (T_{fc} - T_{amb}) \left(\frac{W_{air}}{N_{cells}} \right)^{\frac{1}{1.35}}$$

where W_{air} is the total stack air cooling rate in SLPM, and T_{amb} is the ambient temperature of the cooling air. The heat transfer coefficient $h = 26$ is approximated from the data in operation manual for the Ballard Mark 1020 fcs stack assumed for this simulation.

Finally, electrical power required for the cooling fan can be calculated from the following empirical fan curve,

$$(6.6) \quad P_{cool} = \left(k_1 + k_2 \Delta P_{ca} \frac{W_{air}}{N_{cells}} \right) N_{cells}$$

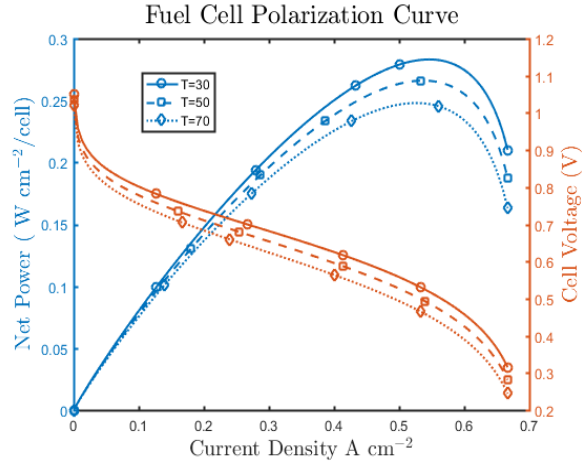


Figure 6.1: Fuel cell polarization curve and power output per cell normalized by cell active area. The fuel cell output power increases with current, and peaks when the voltage drops below a critical value.

Where the constants $k_1 = 1$ and $k_2 = 10^{-3}$ describe the base electrical power of the fan and the work required to overcome the pressure drop across the stack, ΔP_{ca} (Pa), for a given flow rate W_{air} (SLPM). The pressure drop across the stack, ΔP_{ca} is given by

$$(6.7) \quad \Delta P_{ca} = f \frac{4L}{D_h} \left(\frac{1}{2} \rho_{air} U^2 \right) \simeq 4.65U$$

Where f is the friction factor, and $fRe = 14.2$ for a square cross section [97], $L = 60$ mm is the channel length $D_h = 0.66$ mm is the hydraulic diameter, ρ_{air} is the air density. The velocity of air in the cathode channels U can be related to the flow rate W_{air} by, $U = \frac{W_{air}}{N_{cells} A_{CS} 60 \times 10^3}$ where $A_{CS} = 125$ mm² is the total cross sectional area of the channels. At 100 SLPM of air flow per cell the channel velocity is around 13.3 m/s. Under these assumptions, a pressure drop of 50 Pa is predicted by equation 6.7 and a power consumption of 6 W is required for the fan, or 14% of the peak cell power (43 W). The Reynolds number $Re = \frac{UD_h}{\nu_{air}} \simeq 430U$, indicates that laminar flow is a reasonable assumption for the cathode air channels below about 35 SLPM/cell.

Since the fuel cell generates significant heat, requiring a large cooling flow rate,

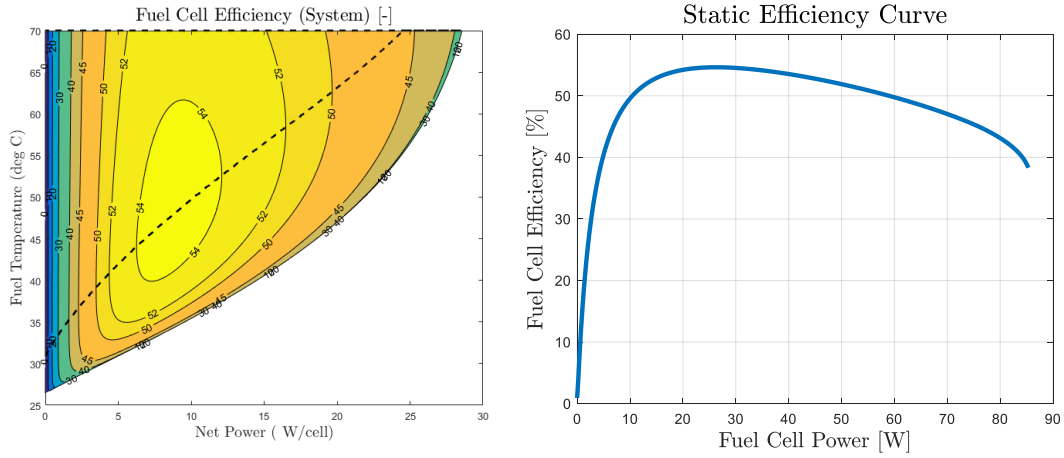


Figure 6.2: Fuel cell system efficiency including power to drive the fan and regulate the stack at a given temperature assuming an ambient temperature of 25°C . The black dashed line indicates the optimum efficiency line for the system as a function of net power and the corresponding stack temperature. The white region in the lower right hand corner of the figure is the set of net power and temperature for which steady state operation is infeasible. That is the cooling power is greater than the stack output at these low temperatures and high operating current.

the model should account for the auxiliary loads for the cooling systems. The system efficiency defined as

$$(6.8) \quad \eta = \frac{P_{fc} - P_{cool}}{I_{fc} E^{th} N_{cells}}$$

Where the stack power is the power per cell multiplied by the number of series connected cells in the stack,

$$(6.9) \quad P_{fc} = I_{fc} V_{cell} N_{cells}$$

The auxiliary loads, P_{cool} , are non-zero, even at zero fuel cell gross output power, therefore the system efficiency is low for small net fuel cell power as shown in Fig. 6.2. Hence, the low power operation, below 10% of the peak power should be avoided, similar to idle condition in internal combustion engines. The system is representative of the NREL targets for FC efficiency given in [98], where the maximum efficiency is at 25% of the maximum load. Also shown in Fig. 6.2 is the optimum efficiency

as a function of fuel cell net power, representing the corresponding steady state temperature which yields that efficiency. We can approximate the fuel cell efficiency from this steady state line and that curve is used as the baseline efficiency of the fuel cell for the initial optimization study. The fuel cell manufacture also specifies a maximum temperature of 70 °C, which is used as a constraint in our optimization routines.

6.2.2 Battery Model

A simple one-state OCV-R type battery model is assumed, where the open circuit voltage is assumed to be a linear function of SOC for simplicity. The cell voltage is given by

$$(6.10) \quad V_b = N_s (V_{OC}(SOC) - I_b R_b)$$

current and SOC is the battery state of charge given by the following differential equation.

$$(6.11) \quad \frac{d}{dt} SOC = \frac{I_b}{3600 Q_b}$$

where Q_b is the battery capacity in Ah and V_{oc} is the battery open circuit voltage, assumed to be a linear function of SOC without loss of generality for simplicity

$$(6.12) \quad V_{OC}(SOC) = (V_{max} - V_{min})SOC + V_{min}$$

Where $V_{min} = 3\text{ V}$ and $V_{max} = 4.2\text{ V}$ are the cell minimum and maximum voltage. The battery current I_b , can be determined from the power by

$$(6.13) \quad I_b = \frac{V_{OC}(SOC) - \sqrt{V_{OC}(SOC)^2 - \frac{4R_b P_b}{N_p N_s}}}{2R_b}$$

where

$$(6.14) \quad P_b = P_{load} + P_{cool} + P_{fc}$$

6.2.3 Component Sizing

The main system design parameters are the number of battery cells and series connected fuel cells, which we call the sizing problem. The base system design can be determined from the simple rule based strategy in equation 6.14, where the total trip energy is divided between the battery and fuel cell. The number of series connected FCs for the base system design is $N_{cells} = 3$, chosen to put the average fuel cell output power near the peak system efficiency, and the number of batteries in series $N_s = 8$ and parallel $N_p = 3$ were chosen to meet the remaining load requirements. The battery temperature should also be considered as a design requirement, with a not to exceed temperature, which would limit the choice of cells based on their internal resistance or number of cells in parallel. The topic of battery temperature will be addressed later in this chapter. In general, increasing the number of battery cells would lower the pack resistance and I^2R losses which cause heating of the battery. However, the increased cell count comes with a weight penalty that increases the mobility power compromising fuel efficiency [99].

6.3 Optimal Control Strategy

6.3.1 Dynamic Programming

To find the optimal split between the battery and fuel cell that minimizes fuel consumption in the fuel cell, dynamic programming (DP) is used in this paper. The Bellman Principle for minimizing a given cost function is the basis for DP [51]. For implementation of the DP algorithm, the open source software DPM is utilized which can handle the non-linear fuel cell model [52]. The algorithm produces an optimal input sequence which that will minimize our given cost function of fuel consumption, which is proportional to the stack current.

$$(6.15) \quad J = \int W_{H_2} = \int \frac{I_{fc} N_{fc} M_{H_2}}{2F}$$

The DP was set up with one input of fuel cell power and one state of battery SOC. In this way, the optimal FC power could be determined while adhering to the battery SOC constraints as well as minimizing hydrogen consumption. Within the model, once the FC power is determined, the corresponding current and voltage were found

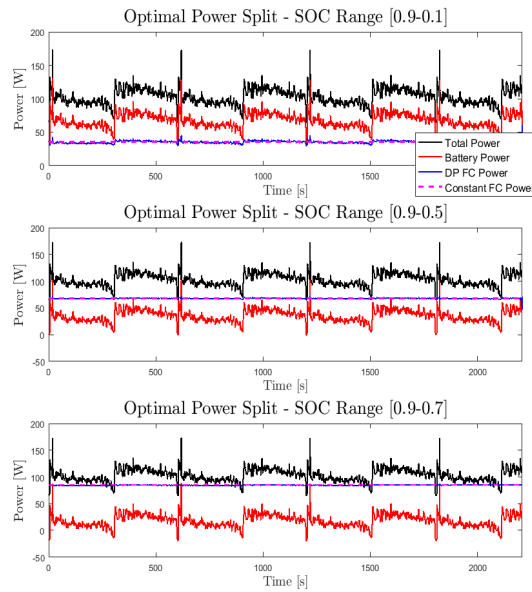


Figure 6.3: Optimal power split between the fuel cell and battery for a given power demand as shown above. Three different SOC ranges are shown that limit the battery energy to approximately full, half and quarter.

by interpolating on the polarization curve. Only the initial part of the polarization curve up to maximum fuel cell power is considered in the interpolation.

The remaining power demand of the drive cycle is to be met by the battery. The maximum battery power is limited by the resistance and the open circuit voltage which depends on the battery SOC. These are regulated in DP using the infeasibility conditions. Hence, from the battery power, the battery current can be determined which updates the battery SOC for the next time step.

Since DP is a numerical method the optimal results depend on the discretization. For this problem, the boundary line method was used that ensures all feasible inputs are considered by predetermining the boundary line between feasible and infeasible spaces [100]. For discretization, the input and state grids were increased till an optimal solution was found and using finer grids did not improve the optimal solution. For a one state, one input problem, DP is computationally quite efficient and can determine the solution fairly quickly, within a few minutes. On the other hand, increasing states or inputs can exponentially increase computation time.

6.3.2 Dynamic Programming Results

The DP results for the optimal power split is shown in Fig. 6.3. The simulations for a given power demand were carried out for three different ranges of battery SOC which limited battery energy to approximately full, half and a quarter of the total battery capacity to isolate the impact of changing pack resistance. As can be seen clearly, as the battery energy reduces, the power demand from the fuel cell increases, as expected. But surprisingly, the optimal fuel cell power is shown to be almost constant for a given battery energy. The variation in load demand was handled completely by the battery, while the fuel cell supplied almost constant power. This behavior was replicated across 6 different drive cycles with significantly varying power demand as well. In all cases, the final SOC was constrained between the limits given below but the optimal SOC trajectory always ended up discharging the battery energy as much as possible.

The almost straight line behavior could, therefore, be approximated with a simple rule-based solution which we define as follows

$$(6.16) \quad FC_{energy} = Total_{energy} - Battery_{energy}$$

$$(6.17) \quad FC_{power} = \frac{FC_{energy}}{TripTime}$$

For the cases shown in Fig. 6.3, the difference between the fuel consumption from DP is given in the table below

Clearly, the simple rule-based solution is able to match the optimal DP solution quite well for all cases and therefore, the simple rule given in equation 6.16,6.17 can quickly determine the optimal power split between the two power sources.

The reason for the fuel cell power being almost constant across the power demand is due to the relatively linear fuel cell efficiency with respect to fuel cell power as shown in Fig 6.4.

From Fig. 6.4, it is clear that switching between different fuel cell powers, changes the fuel cell efficiency linearly and therefore, a constant FC power would be the approximate mean power and by extension a mean efficient point. Hence, overall the fuel consumption is almost the same.

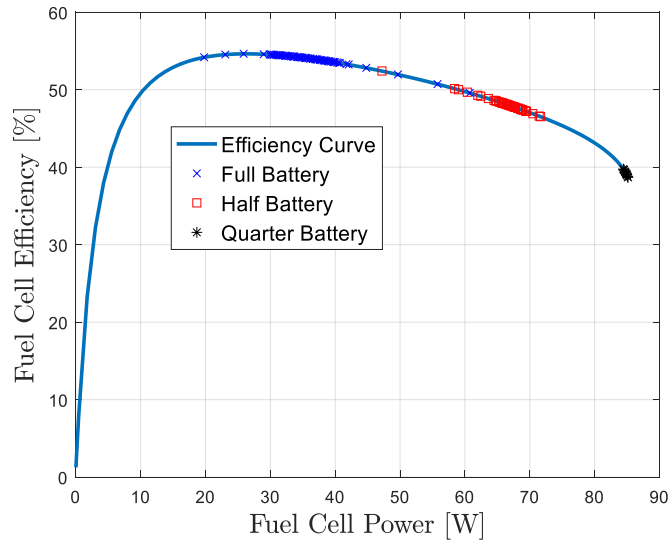


Figure 6.4: Operating points of the fuel cell on the efficiency curve for different battery energy with a 3 cell stack.

6.3.3 Efficiency Results

While the optimal control strategy can be easily approximated with a simple rule-based solution, the optimal sizing of different components also plays a major role in determining energy losses due to inefficient energy conversion in the fuel cell. Fig. 6.5 shows the distribution of various components. The useful electric energy produced in the FC and the efficiency losses are shown separately. Clearly, with the quarter battery even when the sum of battery and fuel cell power is the same, there is a slight increase in the cooling power. This increase in cooling power occurs due to a higher current in the fuel cell required to meet the higher power demand. However, the significant increase in total energy is caused by the increased efficiency losses in hydrogen conversion. These efficiency differences come from stack efficiency and not the power lost to cooling load. As is clear in Fig. 6.4, the quarter battery operates at the lower end of the efficiency curve.

6.3.4 Charge Sustaining

Till now we have only explored the charge depleting case, where the battery SOC end is constrained at a lower level than the start so that the battery can be depleted. Now we will optimize the power split using DP for the charge sustaining case, where

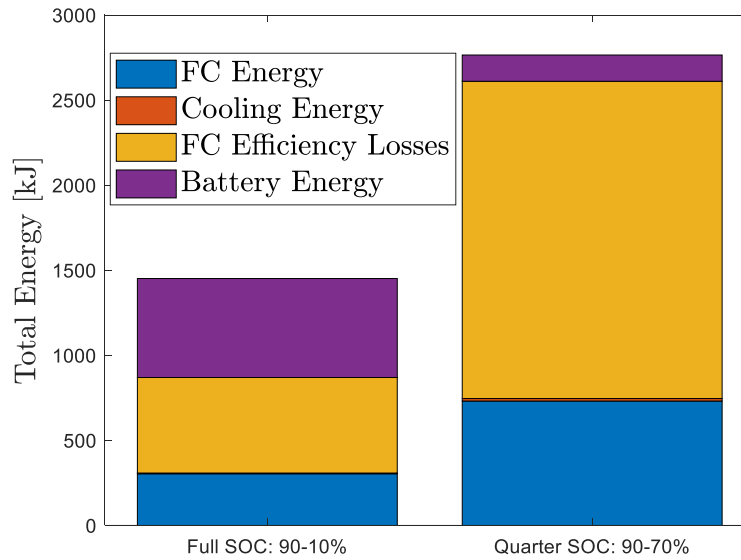


Figure 6.5: Energy demand from different components for full and quarter battery

the start and end of battery SOC are fixed at the same level. Using this formulation, the net battery energy will remain constant or become negative as there are energy conversion losses. However, we have already shown that significant gains in the fuel cell efficiency can be obtained by operating at an efficient point, hence the battery can be utilized for changing the operating point of the fuel cell.

When the optimization was run for the charge sustaining case, again we saw a constant power operation for the fuel cell while the variability in the power demand was handled by the battery. The FC operating point is somewhere at the average power point hence when the demanded total power is less than the FC power, the battery is charged. In this way the battery goes through the same charge-discharge cycles and end up at the same SOC at the end.

The World Harmonized Light Vehicle Test Procedure (WLTP) drive cycle is an interesting velocity profile as the power demand varies significantly over time, unlike the previous case mentioned in this thesis [101]. Hence, now we find the optimal power split with a significantly varying power demand. Even with the significant variations, the FC ends up operating at almost its maximum efficiency point or being shut off. Again, this occurs because significant efficiency gains are possible at the maximum operating point of the FC. We have shown the results for the charge sustaining case in Fig. 6.6, where the during extended periods of zero power

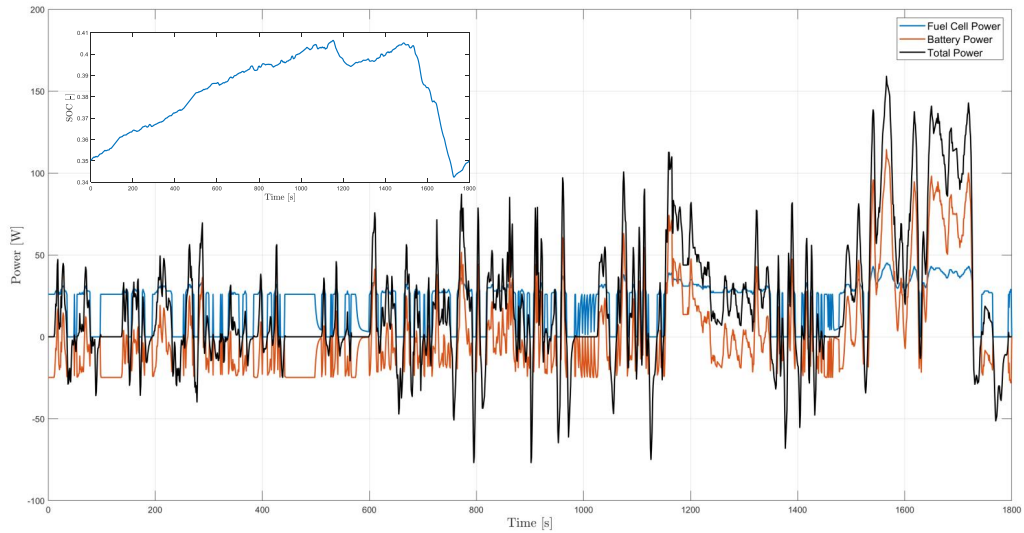


Figure 6.6: Charge Sustaining case for the highly variable WLTP drive cycle

demand, the FC operates at its highest efficiency point and uses this power to charge the battery. Since this is the optimal result obtained through DP, it clearly means that charging the battery and then using this energy later in the drive cycle with all the associated conversion losses, is most efficient.

Therefore, we have shown that even for a drive cycle with a highly variable power demand and the charge sustaining case, the optimal power split, still tries to operate the FC at a constant power, if possible maximum efficiency point. Another optimization was carried out where the power demand from the WLTP cycle was halved. In this case, it can be clearly seen in Fig. 6.7, that the extended periods of battery charging are now avoided. The peak SOC is only at 0.365, as this is enough to navigate the last portions of the drive cycle. Obviously, the Fuel Cell behavior is unrealistic as there are penalties involved in start up and shut down which would reduce these frequent switches. Such a penalty should be included in future work.

6.3.5 Lower Power Demand

The constant power FC operation results were shown for only the cases, where the fuel cell operates in a region where the power is greater than the peak efficiency point. In the cases where the fuel cell power demand was around the 20 W (7 W/cell), the power demand would change due to the non-linear efficiency curve.

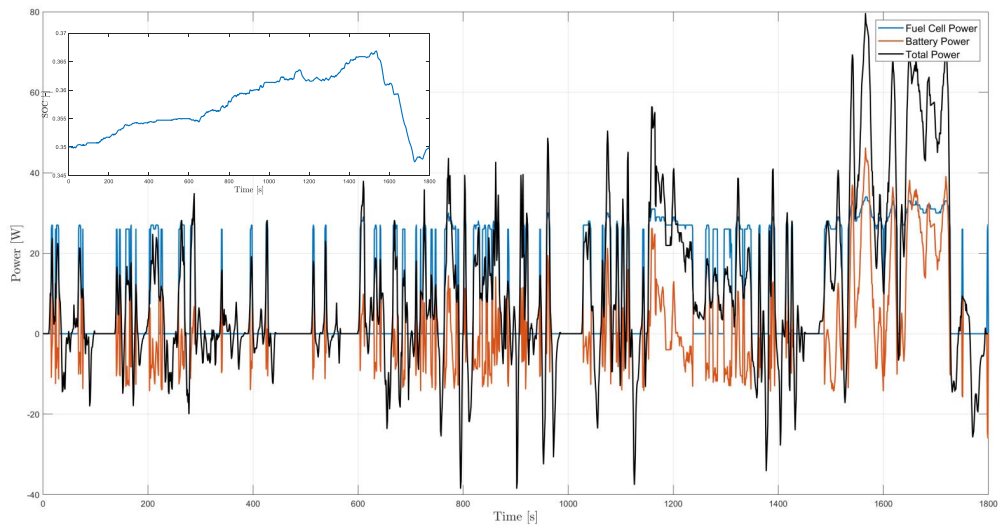


Figure 6.7: Charge Sustaining case for WLTP with half power demand.

The optimal power split in navigating such a trajectory is shown below in Fig. 6.8. In this example, the optimal strategy for the fuel cell is to switch between zero fuel cell power and a constant power that corresponds to the maximum efficiency point. All negative power in the power trajectory is absorbed in the battery to recharge it, while during positive power demand, the fuel cell power is almost constant except for some points. The reason for operation at a higher power is due to limited battery energy despite long charging, where the battery power has to be supplemented by less efficient higher fuel cell power.

Now since the change in efficiency is significantly different and non-linear, the simple rule-based solution from equation 6.17. is not able to match the DP results at all and shows a 20.9% higher hydrogen consumption. The increased consumption of hydrogen is due to operation in the less efficient operating points of the fuel cell where the losses due to auxiliary loads significantly reduce efficiency. The results are shown in Fig. 6.8.

Fig. 6.8 shows the operating points of the DP optimization and the rule-based constant fuel cell power case. While the figure does not show the time of operation, we can confirm from the figure that the maximum time of operation is spent at the maximum efficiency point of 25 – 30 W. As explained before some operating points move into the higher fuel cell power at slightly lower efficiency. At all other times, the

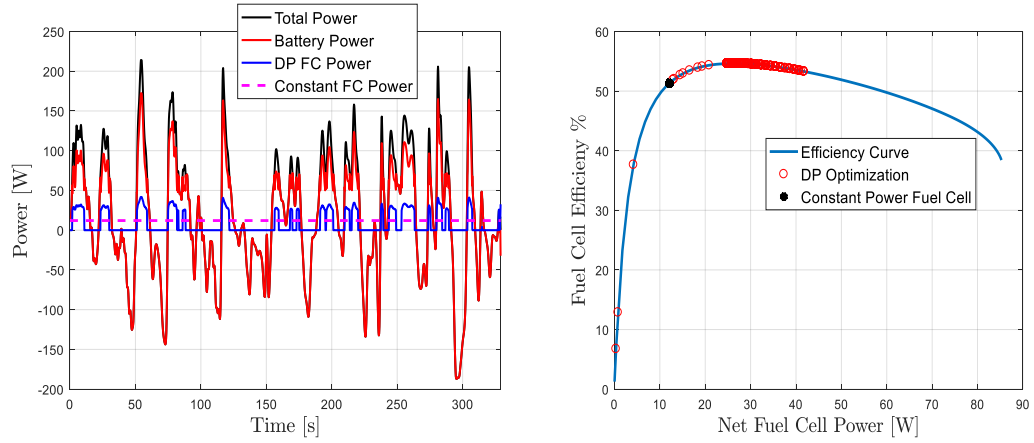


Figure 6.8: Optimal power split between the battery and fuel cell for traversing the Churchill B cycle with the given power demand and the optimal operating points of the Fuel Cell found from DP with the constant operating point of the rule-based solution.

Table 6.2: Battery to trip energy ratio. Average dynamic efficiency and H_2 consumption.

Battery Capacity	Battery to Trip Energy Ratio	Average Eff	FC average Power [W]	H_2 Consumed (g)
Full (1.9 Ah) 90-10%	0.6751	54.6722	33.5243	1.1220
Half 90-50%	0.3631	49.0459	65.6476	2.4536
Half 10x Rb	0.3375	48.2568	68.4135	2.5934
Quarter 90-70%	0.1876	42.1410	83.4637	3.6386
Quarter Nfc=7	0.1877	54.4481	83.6864	2.8158

fuel cell is switched off. The constant power case operates at almost half the power and a much lower efficiency. In doing so, it is also switched on during the regions of negative power demand thus it burns hydrogen in a less efficient manner to only charge the battery. The final battery SOC is same between the DP and rule-based solution, but hydrogen demand for the rule-based is significantly higher.

6.4 Optimal Control Strategy - Thermal Effects

In the previous results, we see that using a simple rule-based strategy produces a solution that nearly replicates the optimal solution found using DP if the fuel cell

power demand is more than 30 W (10W/cell). However, our results were based on a fixed approximation of auxiliary loads, without considering the actual temperature of the fuel cell (only the power required to maintain the optimal temperature for a given load). In the next section, we address the fuel cell thermal dynamics and control of the cooling fan to account for the actual losses from the cooling system as the fuel cell heats up producing useable electric power.

Including a thermal model for our problem provides more realistic answers for the optimal power split. The thermal model has two effects

1. Fuel cell temperature affects the polarization curve thus altering the fuel cell efficiency
2. Maintaining a temperature involves a cooling load which can be accounted for by the heat rejection model

The system efficiency to maintain a given temperature at a given current is shown in Fig. 6.2. The efficiency curve is similar to the NREL curve as the fuel cell efficiency increases up to 10 W/cell and then starts to decrease with increasing net power draw. Also, with increasing temperature, the fuel cell stack efficiency increases till the optimal temperature and then falls significantly due to the increased airflow required to cool the cell and the additional resistive losses due to drying of the membrane. From the efficiency contour shown in Fig. 6.2, we can see that the fuel cell system is most efficient at low loads between 5 – 15 W/cell and medium temperatures between 45 – 65 °C. The portion shown in white is the region of negative steady-state efficiency. This means that at these points, the cooling load to maintain the temperature in steady state is higher than the power produced by the fuel cell. Transient operation during warmup occurs here, but without using the fan to maintain temperature a high efficiency can be achieved at these operation points.

6.4.1 Trajectory Optimization using GPOPS

The issue with including a thermal model is that it increases the model inputs to two by adding the input of cooling air flow and the number of states to two by adding the state of fuel cell temperature. DP is very sensitive to these dimensions, and problems which could previously be solved in a few minutes now require a computation time of a few hours. Hence, a more efficient optimization algorithm was sought.

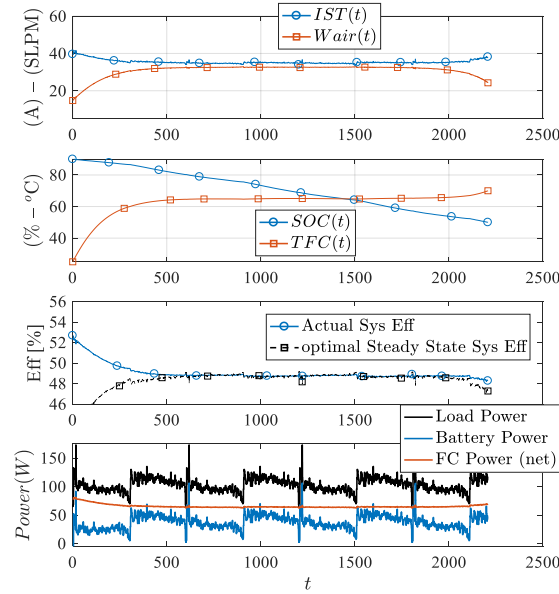


Figure 6.9: Optimal system trajectory for a medium sized battery. The fuel cell and battery delivery roughly equal power to the load.

Pseudo spectral methods that use a direct collocation method to approximate a state using a global polynomial are used for these optimizations [102]. In particular, the commercially available GPOPS software, that utilizes the Legendre-Gauss-Radau (LGR) points for the approximation was used in this paper [103]. The model layout for GPOPS is very similar to DP and has been shown to approximate the DP solutions quite well [104]. The main advantage of using GPOPS is that it is able to reduce computation time significantly from hours to a few 100 s.

The results for the optimal power split and control of the fan are shown in Fig. 6.9 and 6.10 for three distinct simulation cases highlighted in Table 6.4 corresponding to the Half (50 – 90%*SOC*) and Quarter (70 – 90%*SOC*) battery simulations, where the final *SOC* was increased to reduce the available battery energy. The ratio of the battery to trip energy is a useful figure of merit for battery sizing. Fig. 6.9 shows the results for a medium sized battery, the battery trip to energy ratio for the half-sized battery about 0.347, requiring 66% of the energy to come from the fuel cell, however, due to *IR* losses in the battery, the actual energy is a little bit higher for highly dynamic cycles.

Since the battery resistance is relatively low compared to the fuel cell, the transients of the load power are mostly handled by the battery. The fuel cell operates

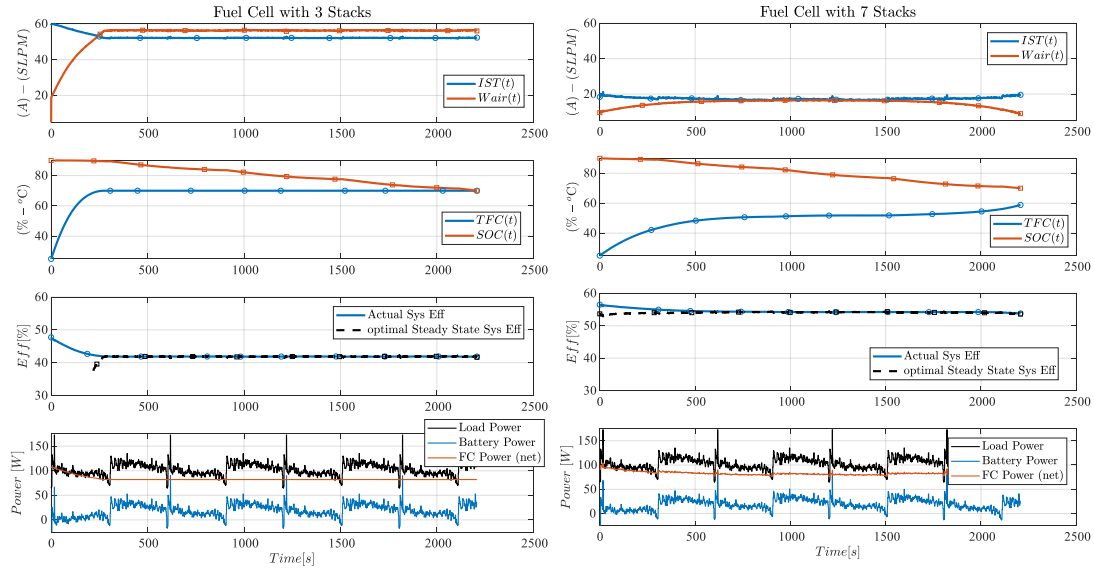


Figure 6.10: Optimal system trajectory for a small battery (quarter sized). Even for this relatively small battery, the optimal solution tends to avoid charging the battery with a monotonically decreasing SOC profile. Since the stack operating temperature is near the limit, the cooling flow cannot be decreased at the end of the cycle. When the fuel cell stack is resize as shown in the right plot from 3 to 7, the cooling requirements reduce and allow the cell to operate at the peak efficiency point.

near constant power, with slightly higher power in the initial phase when the temperature is low, and the efficiency is relatively high (compared to the steady state efficiency) since the fan does not need to operate to cool the cell. At the end of the cycle, again the cooling rate is decreased to save energy, permitting the cell to warm slightly nearing the peak allowable temperature. In future work, the shutdown requirements, including purging will be included in the optimization to capture their impact on energy utilization and final SOC.

The quarter battery simulation shown in Fig. 6.10 shows very poor system efficiency as the FC is required to handle a higher fraction of the load and hence operates at higher temperatures. Increasing the number of cells in the FC stack from 3 to 7 reduces the power per cell and brings the stack operating power back near the peak efficiency point as shown in Fig. 6.10. This highlights the importance of combined battery and FC stack sizing for plug-in hybrid vehicle applications even where the battery energy is less than half of the total trip energy.

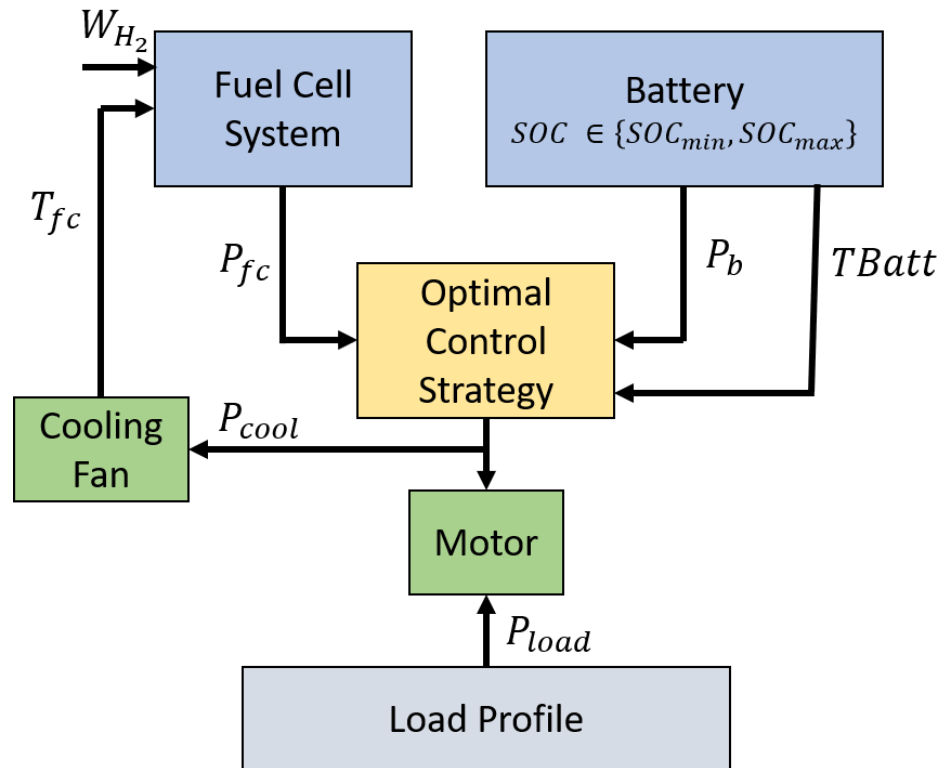


Figure 6.11: Schematic of Fuel Cell with battery thermal states included

6.5 Battery Thermal Results

Till now this work has only considered the thermal effects of the fuel cell. However, the battery discharging current also releases heat and causes an increase in battery temperature. This phenomenon is observed in this section. We use a single state battery thermal model to track temperature of the battery and impose limits in the optimization, on the maximum battery temperature. Now the optimal control problem includes the additional state of battery temperature and must account for that in the optimization as shown in the schematic in Fig. 6.11.

Here we employed some made-up power demand profiles, to understand the effect of including battery thermal dynamics in the optimization. The results are shown in Fig. 6.12, where in the middle plot an additional battery temperature state T_{Batt} is also tracked. In the first instance, the battery could not be discharged completely. This was because the battery temperature rose to its maximum value. The opti-

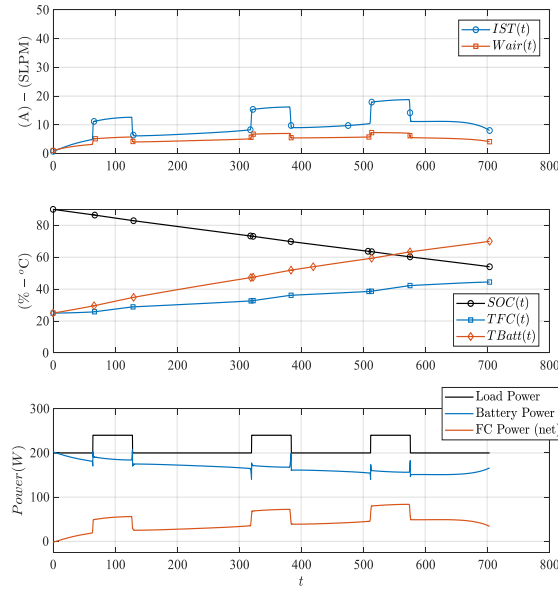


Figure 6.12: After the addition of the battery thermal state, an additional constraint is imposed on the maximum battery temperature. Within the optimization, rising battery temperature prevents a complete battery discharge.

Table 6.3: Increasing trip time, with increasing trip energy demand

Trip Time [s]	H2 Consumed	Trip Energy [Wh]	Battery Energy [Wh]	Batt/Trip energy Ratio	Mean Efficiency Fuel Cell
700	0.37	41.26	32.72	0.79	49.57
1400	1.69	82.52	43.05	0.52	49.97
2100	3.37	123.78	47.22	0.38	48.90

mization ensured that the rate of battery temperature increase was steady, and the maximum temperature is reached only at the end of the drive cycle. Meanwhile, the battery power was gradually reducing and the fuel cell power gradually increasing at a steady slope. Clearly, in this case even if the battery had enough stored energy, it could not be expended for the completion of these profiles.

To explore further we repeated the same profile twice and thrice, thus doubling and tripling the trip duration respectively. With a longer duration to cover, a larger part of the stored battery energy could be used towards powering the motor. This was because the FC, operating power right from the start was higher than in the short profile, thus allowing a lower current in the battery and a lower temperature rise. In the trade-off between extracting higher power from the battery in exchange for higher heating, the optimization pulls lower power for a longer time for maximum discharge.

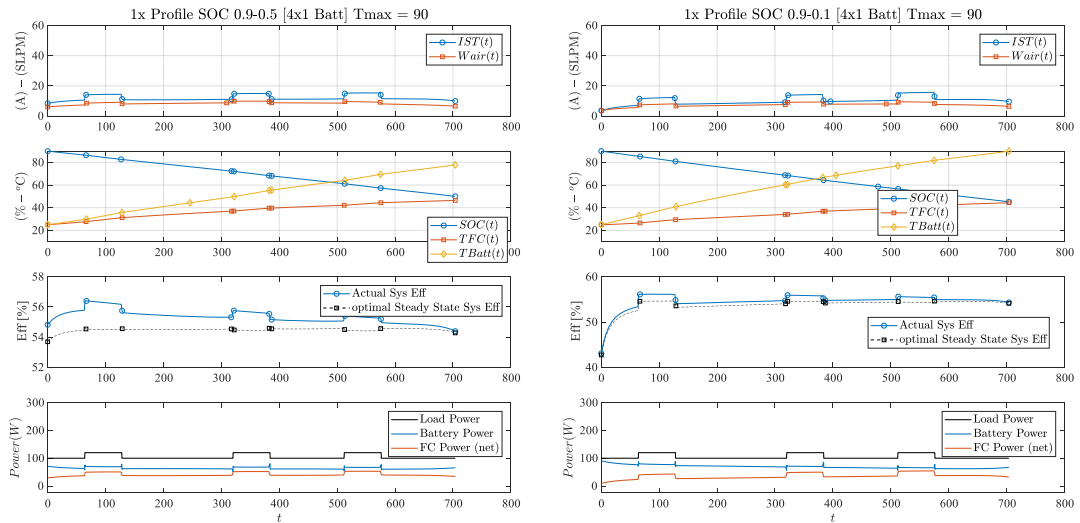


Figure 6.13: Final battery temperature constraints are raised to 90°C . In the left plot with final SOC at 0.5, the battery is discharged to its maximum level without hitting the temperature constraints. On the right plot with the final SOC at 0.1, the battery cannot be discharged as it hits the maximum temperature constraint.

Having said this, in all three cases, the battery is not completely discharged. Moreover, as the trip duration increases, the hydrogen consumption increases significantly, and the battery to trip energy ratio decreases as shown in Table 6.5. It is clear that only a slight increase in battery energy is possible and the higher trip energy demand is met by increased FC power. Also from the last column showing the mean efficiency, we can see that efficiency losses in the FC were not responsible for increased hydrogen consumption.

Further simulations were carried out with an increase in the battery temperature constraint to 90°C as shown in Fig. 6.13. In the left plot, the minimum SOC level is kept at 0.5, thus the battery is able to discharge completely without hitting the maximum temperature constraint. Additionally, the constant power operation of the FC is also maintained. However, in the right plot, when the minimum SOC constraint is lowered to 0.1, the battery is not able to discharge completely and hits its temperature constraints. Now we see a power split, where the battery power reduces slowly, while the FC power correspondingly increases.

6.6 Conclusions

This work highlights the importance of combined sizing and power split for PEMFC hybrid systems. In the case simulated here, the low battery resistance resulted in a nearly constant FC power output when using a simple 1-state battery model with static FC efficiency and dynamic programming. The significant loss in efficiency in FC ensures that the optimal solution is to switch between the maximum efficiency point and FC off. All load leveling was done by the battery. Including the dynamics of FC temperature resulted in an improvement in system efficiency, due to the reduced cooling requirement during stack warmup as compared to the rule-based strategy and dynamic programming results with a static FC model. The rule-based strategy, however, can be effective when the fuel cell operates with powers above the peak system efficiency, where the efficiency decreases gently with increasing power and is almost linear. The effects of battery temperature and battery thermal limits were also considered.

CHAPTER VII

Conclusions and Future Work

While the scepticism is justified as far as around the practicability of fully autonomous vehicles in the near future, the hype surrounding it's imminent introduction has died down. For now, sophisticated technologies that have been developed for lower levels of vehicle autonomy that serve as a sort of Adaptive Cruise Control (ACC) system. These systems are increasingly being sold as standard equipment in mid-size sedans in the United States. With their focus on preventing road accidents, we can expect further liability, economic and regulatory efforts to popularize these systems. The velocity optimization improvements explored in this thesis are all applicable for an ACC type implementation.

This work develops a framework for measuring the Fuel Economy (FE) of self-driving algorithms as a close approximation of present testing. This framework will assist regulators in developing testing procedures to for evaluating current and upcoming algorithms. It has been already shown that FE improvements are not an inevitable consequence of autonomous driving. But applying the framework developed in this thesis present compelling arguments for implementation of those algorithms, especially ones that reduce CO_2 emissions.

Within this framework, velocity smoothing has demonstrated significant benefits in terms of the FE improvement and emissions reduction possible, with offline optimization using full preview. These results have been validated with chassis dynamometer testing at the closely regulated laboratory of the US EPA. It was shown in simulation that with a limited accurate preview of just 1.5s, most of the FE benefits can be retained. And further with an inaccurate preview for 10s using a velocity prediction algorithm, it could still deliver up to 10% increase in FE. These improvements have come about by using a simple, easily implementable double integrator

model, that does not require detailed vehicle characteristics. Additionally, it's been shown that minimization of velocity deviations is also desirable from a passenger comfort perspective. These findings show that, ACC with such MPC optimization can and should be implemented.

Further, this work has evaluated the tractive energy minimization problem, which has been analytically shown to result in a pulse and glide velocity trajectory. It was shown in simulation that while this trajectory has a lower power demand at the wheels, due to the high speed low torque demand of the glide portion of this drive cycle, a disproportionately high fueling rate is demanded. This wipes out all the gains of a lower energy demand over the drive cycle and results in almost the same FE as velocity smoothing. Moreover, since these trajectories are undesirable from a passenger comfort perspective they should not be implemented.

This work also finds that the impact of velocity smoothing on electric vehicles has also been improved as the modified velocity trajectory technique has increased the battery range by 15%. More interestingly, this work showed that there is a trade-off between eco-driving and regenerative braking as methods for range extension in a battery electric vehicle, and using these techniques in combination doesn't add up.

Finally, these optimization techniques have been applied to optimize the power split in a Fuel Cell (FC) hybridized with a Lithium Ion battery. Optimization showed that due to the relatively low resistance of the battery in comparison to the FC, load leveling was done by the battery while FC operated at constant power, if the power demand was greater than the peak efficiency point. These results hold even for the charge sustaining case and even with the introduction of FC thermal states. FC sizing was an important factor in reducing the cooling power demand and balance of plant component sizing was also investigated. The only constraint imposed was a battery temperature limit due to battery discharging and this forces increased FC operation without full battery discharge.

Overall, this work has explored a large range of optimization possibilities for minimization of fuel consumption for algorithm driven vehicles. It has conceived of a framework to evaluate fuel consumption, and within that framework has implemented optimization for a range of gasoline engine sizes, electric vehicles and a fuel cell hybrid.

7.1 Future Work

The work in this thesis has raised some questions that require further investigation. These are listed below:

7.1.1 Co-optimization

It was shown that for fuel consumption minimization an accurate model of the vehicle's powertrain is required for effective optimization. However, an accurate powertrain model significantly increases the number of states and computational complexity involved in processing it. An analysis is required on a powertrain to understand these significant losses and effectively reduce the order for optimization effectively. On the other hand, a better optimization technique might be applied such as pseudospectral methods which could reduce computational time by adopting approximations. This work can also be extended to include other technologies such as cylinder deactivation or discrete engine operating modes like HCCI which have a better efficiency albeit for a limited power range.

7.1.2 Platoon Formation

This thesis did not address the problem of drag coefficient reduction as this would require CFD modeling of various platoon formation. However, there is also additional opportunities for optimization of an ideal platoon formation that locates different size vehicles in the formation such that the overall fuel consumption of the entire group is reduced. For example, an electric vehicle might drive more aggressively to cover for vehicles powered by large gasoline engines, in order to reduce their drag coefficients.

7.1.3 Liquid Cooled Fuel Cells

The work on Fuel Cell hybrids only explored an air cooled fuel cell stack with limited thermal states for the FC and battery. However, this work can be extended to study a liquid cooled stack by adding a physics-based model of membrane hydration and flooding to guide the optimal power split. Such an optimization should consider a full model coupling including dynamic membrane water content, stack temperature and channel humidity.

BIBLIOGRAPHY

BIBLIOGRAPHY

- [1] “Regulatory Impact Analysis : Final Rulemaking for 2017-2025 Light-Duty Vehicle Greenhouse Gas Emission Standards and Corporate Averaged Fuel Economy Standards, EPA-420-R-12-016 August 2012, Table 7.4-2, page 7-32”.
- [2] Gartner, N., Messer, C., and Rathi, A., 2005. “Revised monograph on traffic flow theory,(Chapter 4) Car following models”. *Transportation Research Record*.
- [3] Byungho, L., Lee, S., Cherry, J., Neam, A., Sanchez, J., and Nam, E. “Development of advanced light-duty powertrain and hybrid analysis tool”. *SAE Technical Paper*(2013-01-0808).
- [4] Stuhldreher, M., Schenk, C., Brakora, J., Hawkins, D., Moskalik, A., and DeKraker, P., 2015. “Downsized boosted engine benchmarking and results”. *SAE Technical Paper*(2015-01-1266).
- [5] Goddard, R. H., 1920. A method of reaching extreme altitudes.
- [6] Rutowski, E. S., 1954. “Energy approach to the general aircraft performance problem”. *Journal of the Aeronautical Sciences*, **21**(3), pp. 187–195.
- [7] Vanderbilt, T., 2012. “Autonomous cars through the ages”. *Wired*, Feb.
- [8] Council, N. R., et al., 1998. *National Automated Highway System Research Program: A Review*.
- [9] Robinson, T., Chan, E., and Coelingh, E., 2010. “Operating platoons on public motorways: An introduction to the sartre platooning programme”. In 17th world congress on intelligent transport systems, Vol. 1, p. 12.
- [10] On the road waymo.
- [11] Underwood, S., 2014. “Automated Vehicle Forecast: Vehicle Symposium Opinion Survey”. In Automated Vehicle Symposium.
- [12] Autopilot.
- [13] Autonomous.
- [14] Hawkins, A. J., 2018. “GM will make an autonomous car without steering wheel or pedals by 2019”. *Verge*, Jan.
- [15] Arbib, J., and Seba, T., 2017. “Rethinking transportation 2020–2030: The disruption of transportation and the collapse of the internal-combustion vehicle and oil industries”. In *RethinkX Sector Disruption Reports*. RethinkX California, US.
- [16] Visnic, B., 2018. “Tapping the brakes on autonomy”. *Visnic, B. (2018). Tapping the brakes on autonomy. SAE automotive engineering, [online] (4). Available at: <http://www.nxtbook.com/nxtbooks/sae/18AUTP02/index.php/0> [Accessed 6 Apr. 2018].*, Feb, p. 4.
- [17] Violence, W. H. O., Prevention, I., and Organization, W. H., 2013. *Global status report on road safety 2013: supporting a decade of action*. World Health Organization.
- [18] Singh, S., 2015. Critical reasons for crashes investigated in the national motor vehicle crash causation survey. Tech. rep.

- [19] Schrank, D., Eisele, B., and Lomax, T., 2012. “Ttis 2012 urban mobility report”. *Texas A&M Transportation Institute. The Texas A&M University System*, p. 4.
- [20] Velodyne, 2017. User’s manual hdl - 64e.
- [21] Baji, T., 2017. NVIDIA AI driving platform and AI supercomputer XAVIER.
- [22] Klunder, G. A., Malone, K., Mak, J., Wilmlink, I. R., Schirokoff, A., Sihvola, N., and C., H., 2009. “Impact of information and communication technologies on energy efficiency in road transport-final report”.
- [23] “National Research Council (NRC), Climate Stabilization Targets, p.3”.
- [24] “Inventory of US Greenhouse Gas Emissions and Sinks: 1990-2014, EPA Publication number EPA 430-R-16-002, April 15,2016”.
- [25] “Proposed Determination on the Appropriateness of the Model Year 2022-2025 Light-Duty Vehicle Greenhouse Gas Emission Standards under the Midterm Evaluation, EPA Publication number EPA-420-R-16-020 November 2016”.
- [26] Wadud, Z., MacKenzie, D., and Leiby, P., 2012. “Help or hindrance? the travel, energy and carbon impacts of highly automated driving”. *Transportation Research Part A*, **17**, pp. 201–207.
- [27] Sciarretta, A., De Nunzio, G., and Ojeda, L. L., 2015. “Optimal ecodriving control: Energy-efficient driving of road vehicles as an optimal control problem”. *IEEE Control Systems*, **35**(5), pp. 71–90.
- [28] Evans, L., 1978. “Driver behavior effects on fuel consumption in urban driving”. In *Proceedings of the Human Factors Society Annual Meeting*, Vol. 22, Sage Publications Sage CA: Los Angeles, CA, pp. 437–442.
- [29] Boriboonsomsin, K., Vu, A., and Barth, M., 2010. “Eco-driving: pilot evaluation of driving behavior changes among us drivers”. *University of California Transportation Center*.
- [30] Zarkadoula, M., Zoidis, G., and Tritopoulou, E., 2007. “Training urban bus drivers to promote smart driving: A note on a greek eco-driving pilot program”. *Transportation Research Part D: Transport and Environment*, **12**(6), pp. 449–451.
- [31] Barkenbus, J. N., 2010. “Eco-driving: An overlooked climate change initiative”. *Transportation Research Part C: Emerging Technologies*, **38**(2), pp. 762–769.
- [32] Gonder, J., Earleywine, M., and Sparks, W., 2012. “Analyzing vehicle fuel saving opportunities through intelligent driver feedback”. *SAE International Journal of Passenger Cars-Electronic and Electrical Systems*, **5**(2012-01-0494), pp. 450–461.
- [33] He, Y., Rios, J., Chowdhury, L., Pisu, P., and Bhavsar, P., 2012. “Forward power-train energy management modeling for assessing benefits of integrating predictive traffic data into plug-in-hybrid electric vehicles”. *Transportation Research Part D*, **17**, pp. 201–207.
- [34] Manzie, C., Watson, H., and Halgamuge, S., 2007. “Fuel economy improvements for urban driving: Hybrid vs. intelligent vehicles”. *Transportation Research Part C: Emerging Technologies*, **15**(1), pp. 1–16.
- [35] Mensing, F., Bideaux, E., Trigui, R., and Tattegrain, H., 2013. “Trajectory optimization for eco-driving taking into account traffic constraints”. *Transportation Research Part D*, **18**, pp. 55–61.
- [36] Shengbo, K., Wang, J., Zhang, L., Lian, X., Ukawa, H., and Bai, D., 2008. “MPC based vehicular following control considering both fuel economy and tracking capability”. *Vehicle Power and Propulsion Conference, IEEE*, pp. 1–6.
- [37] Lee, J., and Nelson, D. J. “Vehicle inertial impact on fuel consumption of conventional and hybrid electric vehicles using acceleration and coast driving strategy”. *SAE Technical Paper*(2009-01-1322).
- [38] Li, S. E., Peng, H., Li, K., and Wang, J., 2012. “Minimum fuel control strategy in autonomous car-following scenarios”. *IEEE Transactions on Vehicular Technology*, **61**(3), pp. 998–1007.

- [39] Li, S. E., and Peng, H., 2012. “Strategies to minimize the fuel consumption of passenger cars during car-following scenarios”. *Proceedings of the Institution of Mechanical Engineers, Part D: Journal of Automobile Engineering*, **226**(3), pp. 419–429.
- [40] Mench, M. M., 2008. *Fuel cell engines*. John Wiley & Sons.
- [41] Pukrushpan, J. T., Stefanopoulou, A. G., and Peng, H., 2004. *Control of fuel cell power systems: principles, modeling, analysis and feedback design*. Springer Science & Business Media.
- [42] Bonsall, P., Liu, R., and Young, W., 2005. “Modelling safety-related driving behaviour impact of parameter values”. *Transportation Research Part A: Policy and Practice*, **39**(5), pp. 425–444.
- [43] Treiber, M., Hennecke, A., and Helbing, D., 2000. “Congested traffic states in empirical observations and microscopic simulations”. *Physical review E*, **62**(2), p. 1805.
- [44] Lefèvre, S., Sun, C., Bajcsy, R., and Laugier, C., 2014. “Comparison of parametric and non-parametric approaches for vehicle speed prediction”. In American Control Conference (ACC), 2014, IEEE, pp. 3494–3499.
- [45] Reed, P., 2005. “We test the tips: What really saves gas? and how much”.
- [46] LeBlanc, D. J., Sivak, M., and Bogard, S., 2010. “Using naturalistic driving data to assess variations in fuel efficiency among individual drivers”.
- [47] Kruse, R. E., and Huls, T. A., 1973. Development of the federal urban driving schedule. Tech. rep., SAE Technical Paper.
- [48] Austin, T. C., Hellman, K. H., and Paulsell, C. D., 1974. Passenger car fuel economy during non-urban driving. Tech. rep., SAE Technical Paper.
- [49] Prakash, N., Stefanopoulou, A. G., Moskalik, A. J., and Brusstar, M. J., 2016. “Use of the hypothetical lead (hl) vehicle trace: A new method for evaluating fuel consumption in automated driving”. In American Control Conference (ACC), 2016, IEEE, pp. 3486–3491.
- [50] Zhang, H. M., and Kim, T., 2005. “A car-following theory for multiphase vehicular traffic flow”. *Transportation Research Part B: Methodological*, **39**(5), pp. 385–399.
- [51] Bertsekas, D., 2005. *Dynamic programming and optimal control*. Belmont, Massachusetts: Athena Scientific.
- [52] Sundstrom, O., and Guzzella, L., 2009. “A generic dynamic programming matlab function”. In Control Applications, (CCA) & Intelligent Control, (ISIC), pp. 1625–1630.
- [53] Prakash, N., Cimini, G., Stefanopoulou, A. G., and Brusstar, M. J., 2016. “Assessing fuel economy from automated driving: Influence of preview and velocity constraints”. In ASME 2016 Dynamic Systems and Control Conference, American Society of Mechanical Engineers, pp. V002T19A001–V002T19A001.
- [54] Wan, N., Vahidi, A., and Luckow, A., 2016. “Optimal speed advisory for connected vehicles in arterial roads and the impact on mixed traffic”. *Transportation Research Part C*, **69**, pp. 548–563.
- [55] Chang, D. J., and Morlok, E. K., 2005. “Vehicle speed profiles to minimize work and fuel consumption”. *Journal of Transportation Engineering*, **131**, pp. 173–182.
- [56] Schwarzkopf, A., and Leipnik, R., 1977. “Control of highway vehicles for minimum fuel consumption over varying terrain”. *Transportation Research*, **11**(4), pp. 279–286.
- [57] Prakash, N., Kim, Y., Rizzo, D. M., Brusstar, M. J., and Siegel, J., 2018. “Role of regenerative braking in velocity trajectory optimization of electrified powertrains over varying road grades”. In 2018 IEEE Conference on Control Technology and Applications (CCTA), IEEE, pp. 1014–1019.
- [58] Siegel, J. B., Stefanopoulou, A. G., Rizzo, D., and Prakash, N., 2018. Cooling parasitic considerations for optimal sizing and power split strategy for military robot powered by hydrogen fuel cells. Tech. rep., SAE Technical Paper.

- [59] Snapp, L., 2015. “Epa policy considerations for connected and automated vehicles”. *Presented at Automated Vehicle Symposium, Ypsilanti*.
- [60] Mersky, A. C., and Samaras, C., 2015. “How will autonomous vehicle technology affect fuel economy ratings?”. *Poster presented at Automated Vehicle Symposium, Ypsilanti*.
- [61] Austin, T. C., Hellman, K. H., and Paulsell, C. D., 1974. “Passenger car fuel economy during non-urban driving”. *SAE Transactions*, pp. 2353–2357.
- [62] Stuhldreher, M., Schenk, C., Brakora, J., Hawkins, D., Moskalik, A., and DeKraaker, P., 2015. Downsized boosted engine benchmarking and results. Tech. rep., SAE Technical Paper.
- [63] Kesting, A., Treiber, M., Schonhof, M., and Helbing, D., 2008. “Adaptive cruise control design for active congestion avoidance”. *Transportation Research Part C*, **16**(1), pp. 668–683.
- [64] Mayne, D. Q., 2014. “Model predictive control: Recent developments and future promise”. *Automatica*, **50**(12), pp. 2967 – 2986.
- [65] NHTSA, 2010. *Summary of State Speed Laws*, 11 ed.
- [66] Office, U. S. G. P., 2016. *Code of Federal Regulations, Title 40, Protection of Environment, Part 86 Sections 86.158, Supplemental Federal Test Procedures; overview*. Government Printing Office.
- [67] Del Re, L., Allgöwer, F., Glielmo, L., Guardiola, C., and Kolmanovsky, I., 2010. *Automotive Model Predictive Control: Models, Methods and Applications*. Lecture Notes in Control and Information Sciences. Springer London.
- [68] Hartley, E. N., and Maciejowski, J. M., 2015. “Field programmable gate array based predictive control system for spacecraft rendezvous in elliptical orbits”. *Optimal Control Applications and Methods*, **35**(7), pp. 585–607.
- [69] Kouro, S., Perez, M., Rodriguez, J., Llor, A., and Young, H., 2015. “Model predictive control: MPC’s role in the evolution of power electronics”. *Industrial Electronics Magazine, IEEE*, **9**(4), Dec, pp. 8–21.
- [70] Necoara, I., 2015. “Computational complexity certification for dual gradient method: Application to embedded MPC”. *Systems & Control Letters*, **81**, pp. 49 – 56.
- [71] Cimini, G., Bernardini, D., Bemporad, A., and Levijoki, S., 2015. “Online model predictive torque control for permanent magnet synchronous motors”. In *Industrial Technology (ICIT), 2015 IEEE International Conference on*, pp. 2308–2313.
- [72] Bemporad, A., 2015. “A quadratic programming algorithm based on nonnegative least squares with applications to embedded model predictive control”. *IEEE Transactions on Automatic Control*, **PP**(99), pp. 1–1.
- [73] Ferreau, H. J., Bock, H. G., and Diehl, M., 2008. “An online active set strategy to overcome the limitations of explicit MPC”. *International Journal of Robust and Nonlinear Control*, **18**(8), pp. 816–830.
- [74] Nüesch, S., Sterniak, J., Jiang, L., and Stefanopoulou, A. G., 2015. “On beneficial mode switch decisions based on shortterm engine load prediction”. *IFAC E-COSM*.
- [75] Eunjeong Hyeon, Youngki Kim, N. P., and Stefanopoulou, A. G., 2019. “Short-term speed forecasting using vehicle wireless communications”. In *American Controls Conference* (submitted).
- [76] Ozatay, E., Onori, S., Wollaeger, J., Ozguner, U., Rizzoni, G., Filev, D., Michelini, J., and Di Cairano, S., 2014. “Cloud-based velocity profile optimization for everyday driving: A dynamic programming based solution”. *IEEE Transactions on Intelligent Transportation Systems*, **15**(6), pp. 2491–2505.
- [77] Turri, V., Kim, Y., Guanetti, J., Johansson, K. H., and Borrelli, F., 2017. “A model predictive controller for non-cooperative eco-platooning”. In *American Control Conference (ACC), 2017, IEEE*, pp. 2309–2314.

- [78] Li, N. I., He, C. R., and Orosz, G., 2016. “Sequential parametric optimization for connected cruise control with application to fuel economy optimization”. *Proceedings of the Conference on Decision and Control*, pp. 227–232.
- [79] Kadijk, G., and Ligterink, N., 2012. “Road load determination of passenger cars”. *TNO report*, **10237**, p. 2012.
- [80] Newman, K., Kargul, J., and Barba, D., 2015. Benchmarking and modeling of a conventional mid-size car using alpha. Tech. rep., SAE Technical Paper.
- [81] Dekraker, P., Stuhldreher, M., and Kim, Y., 2017. “Characterizing factors influencing si engine transient fuel consumption for vehicle simulation in alpha”. *SAE International Journal of Engines*, **10**(2017-01-0533), pp. 529–540.
- [82] Dekraker, P., Kargul, J., Moskalik, A., Newman, K., Doorlag, M., and Barba, D., 2017. “Fleet-level modeling of real world factors influencing greenhouse gas emission simulation in alpha”. *SAE International Journal of Fuels and Lubricants*, **10**(2017-01-0899), pp. 217–235.
- [83] Dib, W., Serrao, L., and Sciarretta, A., 2011. “Optimal control to minimize trip time and energy consumption in electric vehicles”. In Vehicle Power and Propulsion Conference (VPPC), 2011 IEEE, IEEE, pp. 1–8.
- [84] Dib, W., Chasse, A., Moulin, P., Sciarretta, A., and Corde, G., 2014. “Optimal energy management for an electric vehicle in eco-driving applications”. *Control Engineering Practice*, **29**, pp. 299–307.
- [85] Hellström, E., Ivarsson, M., Åslund, J., and Nielsen, L., 2009. “Look-ahead control for heavy trucks to minimize trip time and fuel consumption”. *Control Engineering Practice*, **17**(2), pp. 245–254.
- [86] Ozatay, E., Ozguner, U., Micheli, J., and Filev, D., 2014. “Analytical solution to the minimum energy consumption based velocity profile optimization problem with variable road grade”. *IFAC Proceedings Volumes*, **47**(3), pp. 7541–7546.
- [87] Gong, Q., Li, Y., and Peng, Z.-R., 2008. “Trip-based optimal power management of plug-in hybrid electric vehicles”. *IEEE Transactions on vehicular technology*, **57**(6), pp. 3393–3401.
- [88] Bin, Y., Li, Y., Gong, Q., and Peng, Z.-R., 2009. “Multi-information integrated trip specific optimal power management for plug-in hybrid electric vehicles”. In American Control Conference, 2009. ACC’09., IEEE, pp. 4607–4612.
- [89] Katsargyri, G.-E., Kolmanovsky, I. V., Micheli, J., Kuang, M. L., Phillips, A. M., Rinehart, M., and Dahleh, M. A., 2009. “Optimally controlling hybrid electric vehicles using path forecasting”. In American Control Conference, 2009. ACC’09., IEEE, pp. 4613–4617.
- [90] Zhang, C., and Vahidi, A., 2012. “Route preview in energy management of plug-in hybrid vehicles”. *IEEE Transactions on Control Systems Technology*, **20**(2), pp. 546–553.
- [91] Directorate, A. “Test operations procedure (top) 01-1-011a vehicle test facilities at aberdeen test center and yuma test center”. *US Army Aberdeen Test Center, Aberdeen Proving Ground, MD, Final TOP*, pp. 01–1.
- [92] Siegel, J. B., Wang, Y., Stefanopoulou, A. G., and McCain, B. A., 2015. “Comparison of sofc and pem fuel cell hybrid power management strategies for mobile robots”. In 2015 IEEE Vehicle Power and Propulsion Conference (VPPC), IEEE, pp. 1–6.
- [93] Boice, K., Leo, A., Lee, J., Paulson Jr, J., Skalny, M., and Valascho, T., 2010. Baseline field testing of bb-2590 lithium-ion batteries using an irobot fastac 510 robot. Tech. rep., ARMY TANK AUTOMOTIVE RESEARCH DEVELOPMENT AND ENGINEERING CENTER WARREN MI.
- [94] Zhiyu, Y., Tao, X., Zhixiang, L., Yun, P., and Weirong, C., 2014. “Study on air-cooled self-humidifying pemfc control method based on segmented predict negative feedback control”. *Electrochimica Acta*, **132**, pp. 389–396.
- [95] Nandjou, F., Poirot-Crouvezier, J.-P., Chandesris, M., Blachot, J.-F., Bonnaud, C., and Bultel, Y., 2016. “Impact of heat and water management on proton exchange membrane fuel cells degradation in automotive application”. *Journal of Power Sources*, **326**, pp. 182–192.

- [96] Yesilyurt, S., Siegel, J. B., and Stefanopoulou, A. G., 2012. “Modeling and experiments of voltage transients of polymer electrolyte membrane fuel cells with the dead-ended anode”. *Journal of Fuel Cell Science and Technology*, **9**(2), p. 021012.
- [97] Bejan, A., 2013. *Convection heat transfer*. John wiley & sons.
- [98] Zolot, M., Markel, A. J., and Pesaran, A. A., 2007. *Analysis of fuel cell hybridization and implications for energy storage devices*. National Renewable Energy Laboratory.
- [99] Sundström, O., and Stefanopoulou, A., 2007. “Optimum battery size for fuel cell hybrid electric vehiclepart i”. *Journal of fuel cell science and technology*, **4**(2), pp. 167–175.
- [100] Sundström, O., Ambühl, D., and Guzzella, L., 2010. “On implementation of dynamic programming for optimal control problems with final state constraints”. *Oil & Gas Science and Technology—Revue de l’Institut Français du Pétrole*, **65**(1), pp. 91–102.
- [101] Ciuffo, B., Marotta, A., Tutuianu, M., Anagnostopoulos, K., Fontaras, G., Pavlovic, J., Serra, S., Tsiakmakis, S., and Zacharof, N., 2015. “The development of the world-wide harmonized test procedure for light duty vehicles (wltp) and the pathway for its implementation into the eu legislation”. In TRB 2015 Annual Meeting.
- [102] Patterson, M. A., and Rao, A., 2012. “Exploiting sparsity in direct collocation pseudospectral methods for solving optimal control problems”. *Journal of Spacecraft and Rockets*, **49**(2), pp. 354–377.
- [103] Patterson, M. A., and Rao, A. V., 2014. “Gpops-ii: A matlab software for solving multiple-phase optimal control problems using hp-adaptive gaussian quadrature collocation methods and sparse nonlinear programming”. *ACM Transactions on Mathematical Software (TOMS)*, **41**(1), p. 1.
- [104] Zhou, W., Zhang, C., Li, J., and Fathy, H. K., 2016. “A pseudospectral strategy for optimal power management in series hybrid electric powertrains”. *IEEE Transactions on Vehicular Technology*, **65**(6), pp. 4813–4825.